

A Portable, Ultra-Low Cost NMR Device

by

Ashley Brown Raynal

S.B., Massachusetts Institute of Technology (2012)

S.M., Massachusetts Institute of Technology (2014)

Submitted to the Department of Mechanical Engineering
in partial fulfillment of the requirements for the degree of

Doctor of Philosophy in Mechanical Engineering

at the

MASSACHUSETTS INSTITUTE OF TECHNOLOGY

September 2019

© Massachusetts Institute of Technology 2019. All rights reserved.

Signature redacted

Author
.....

Department of Mechanical Engineering
August 8, 2019

Signature redacted

Certified by
.....

Ian W. Hunter

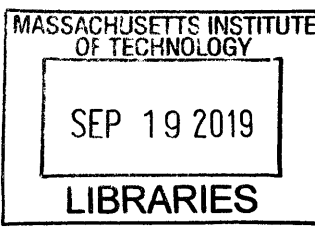
Hatsopoulos Professor of Mechanical Engineering

Signature redacted Thesis Supervisor

Accepted by
.....

Nicolas Hadjiconstantinou

Chairman, Department Committee on Graduate Theses



A Portable, Ultra-Low Cost NMR Device

by

Ashley Brown Raynal

Submitted to the Department of Mechanical Engineering
on August 8, 2019, in partial fulfillment of the
requirements for the degree of
Doctor of Philosophy in Mechanical Engineering

Abstract

Nuclear magnetic resonance (NMR) provides powerful measurements that remain inaccessible in many applications due to the instruments' size and expense. Recent research efforts have focused on creating handheld devices with lower resolution but greatly reduced cost. Persistent challenges include implementing a miniature magnet with sufficiently homogeneous magnetic field, and isolating the weak NMR signal from the powerful excitation pulses. In this thesis, we demonstrate a magnet design and experimental technique to address these needs.

A significant cost for a small NMR magnet is associated with the extensive labor for assembly and correction of field variations. To alleviate this difficulty, we optimized and constructed a self-assembling NMR magnet. The palm-sized assembly, called a shim-a-ring, had a mass of 418 g. The magnetic field strength was 0.48 T, large enough to perform spectroscopy. To ease the process of correcting the field, we propose an active shim system, which would eliminate much of the labor required with other strategies. Electromagnetic shims were optimized to correct 14 lower-order spherical harmonics with minimal power consumption. When comparing the efficiency of the shims to the correction needed in the shim-a-ring magnet, the required current was found to be too large for steady-state operation. In short experiments, however, the strategy was shown to be feasible, with heat dissipation causing only a negligible temperature change.

Stochastic excitation provides a low-power alternative to standard NMR techniques. With the pulse amplitudes reduced by orders of magnitude, isolating the signal from the excitation is much less challenging. Experiments performed in the shim-a-ring magnet demonstrated this benefit. Although the magnetic field variations were too large for spectroscopy, the initial amplitude of the impulse response was proportional to the number of resonant nuclei in the sample, called the spin density. The ratio of water and heavy water contained in a sample was characterized using this technique.

Thesis Supervisor: Ian W. Hunter

Title: Hatsopoulos Professor of Mechanical Engineering

Acknowledgments

When I entered MIT as a freshman in 2008, I had no idea that I would remain a student on campus for over a decade. Now as I look back, I am so grateful for the unexpected directions that my life took, and for the people who helped me along the way.

First, I'd like to thank Prof. Hunter for the tremendous opportunities, encouragement, and support he's given me over the past 8 years in the BioInstrumentation Lab. His confidence in my abilities, and the freedom he gave me in pursuing challenging projects have formed me into the engineer I am today. I'm particularly grateful for his amazing support this past year as I've been adjusting to life as a new mother while finishing this thesis.

I've been so lucky to have intelligent, amiable, and generous colleagues in the BioInstrumentation Lab: Bryan, Alison, Ashin, Mike, Brian, Craig, Geethoon, Nick, Seyed, Span, Lina and many others. I'd like to give a special thank you to Kate Melvin and Shibani Joshi, who keep the lab running smoothly and have helped me on countless occasions. I'd also like to thank my dear friend and trusted mentor Dr. Cathy Hogan, whose bedrock presence in the lab we cherish.

The folks over at the Martinos Center were so helpful with getting me started in NMR hardware and finding resonance. Dr. Larry Wald was so generous in opening his lab, and Dr. Jason Stockmann spent many hours working through NMR hardware and experimental fundamentals with me. I am truly grateful.

Lastly, I'm so thankful for my friends and family. Becoming a mother myself has made me more deeply appreciate the tremendous job my own parents did, and so grateful for their unfailing love and support. In my husband Jean-Raymond I am blessed beyond measure. He's strong-minded yet very sweet; he's self-sacrificing and an affable companion. His loving support in finishing this chapter of my life has been essential, and I'm so excited to continue our journey together.

Contents

Contents	7
List of Figures	11
List of Tables	15
1 Introduction	17
1.1 Motivation	17
1.2 Principles	19
1.2.1 Spin	19
1.2.2 Magnetic Moment	19
1.2.3 Radiofrequency Pulses	22
1.2.4 Free Induction Decay	23
1.2.5 Inhomogeneous Magnetic Field	24
1.2.6 NMR Spectra	26
1.2.7 A Simple NMR Experiment	27
1.2.8 Rotating Frame	28
1.2.9 Bloch Equations	28
1.2.10 Quadrature Detection	29
2 NMR Spectrometer Construction	31
2.1 NMR Probe	32
2.2 Transmitter Pathway	36
2.3 Receiver Pathway	37

2.4	MyRIO Controller	40
2.5	Example Measurements	42
3	Portable NMR Magnet	47
3.1	Comparison of Magnet Designs	48
3.1.1	Iron Yoke	48
3.1.2	Halbach Array	49
3.1.3	Aubert Configuration	52
3.1.4	Shim-a-Ring	52
3.1.5	Design Comparison	54
3.2	Shim-a-Ring Optimization	56
3.2.1	Commercially Available Magnet	58
3.2.2	Custom Magnet	60
3.3	Active Shim System	66
3.3.1	Measurement of Spherical Harmonics	68
3.3.2	Shim Design	73
3.3.3	Active Shim Feasibility	88
4	Stochastic Spin Density	95
4.1	Correlation Techniques	96
4.1.1	Derivation	96
4.1.2	Experimental Details	99
4.1.3	Measurement in an Inhomogeneous Field	100
4.2	Bloch Simulations	102
4.3	Experimental Measurements	108
5	Conclusion	119
A	Code	121
A.1	LabVIEW Code	121
A.2	MATLAB Code	123

List of Figures

1-1	Larmor Precession	20
1-2	T ₁ Relaxation	22
1-3	Measurement Coil	24
1-4	Free Induction Decay	25
1-5	Summed Sinusoids	25
1-6	NMR Spectrum	26
1-7	Inhomogeneous Broadening	27
2-1	NMR Spectrometer Block Diagram	32
2-2	NMR Probe	33
2-3	Tank Circuit Diagram	34
2-4	Tank Circuit Bode Plot	35
2-5	Tank Circuit PCB	36
2-6	Measured Tank Impedance	37
2-7	Transmitter Pathway	38
2-8	Excitation Amplifier	38
2-9	Receiver Pathway	39
2-10	Preamplifier and Band-pass Filter	39
2-11	Power Splitter, Mixers and Low Freq. Amp	41
2-12	MyRIO with External ADC	43
2-13	NMR Electromagnet	44
2-14	FID in Electromagnet	44
2-15	Pulse Echo in Electromagnet	45

2-16 Pulse Echo Using Mixer	46
3-1 Iron Yoke Magnet	49
3-2 Ideal Halbach Array	50
3-3 Halbach Realizations	51
3-4 Aubert Magnet Configuration	53
3-5 Shim-a-ring Magnet	54
3-6 Hall Effect Sensor	57
3-7 Hall Supply Circuit	57
3-8 Shim-a-ring Assembly Hardware	59
3-9 Assembled Shim-a-ring	59
3-10 Large Shim-a-ring Measured Field	60
3-11 Field Strength vs. Bore Size	61
3-12 Homogeneity and Axial Length	62
3-13 Homogeneity and Bore Size	63
3-14 Shim-a-ring with Custom Magnet	63
3-15 Small Shim-a-ring Measured Field	64
3-16 FID in Shim-a-ring	65
3-17 Shimming Prior Art	67
3-18 Coordinate System for Field Measurements	69
3-19 Magnetic Field Map	70
3-20 Change of Axes	71
3-21 Discrete Stream Function	75
3-22 First Order Shim Designs	77
3-23 Second Order Shim Designs	78
3-24 Higher Order Shim Designs	79
3-25 Flexible Circuit Composition	80
3-26 Shim Fabrication	82
3-27 Shim Assembly	83
3-28 Nesting Shims	84

4-1	Pulses in FT NMR and Stochastic NMR	99
4-2	Stochastic NMR Simulation	103
4-3	Magnetization Path in Stochastic NMR	105
4-4	Inhomogeneous Field Simulations	107
4-5	Slow Sampling Simulation	109
4-6	H ₂ O and D ₂ O Impulse Response	110
4-7	Measured Magnetization	111
4-8	Spin Density by Peak Value	112
4-9	Spin Density by Integrating	113
4-10	Parametric Fit of Impulse Response	114
4-11	Spin Density by Parametric Model	115
4-12	Stochastic Resonance Screenshot	117
A-1	FPGA Code	122

List of Tables

3.1	Comparison of compact magnet designs	56
3.2	Custom magnet specifications	62
3.3	Measured harmonic coefficients	72
3.4	Specifications for shim design	76
3.5	Efficiency of 6 mm shims	86
3.6	Efficiency to 10 mm shims	87
3.7	Correcting current for 6 mm shims	89
3.8	Correcting current for 10 mm shims	90
3.9	Total power dissipated by active shims	92

Chapter 1

Introduction

1.1 Motivation

Nuclear magnetic resonance (NMR) is used to take powerful measurements that are a staple in modern medicine and chemistry. At its core, the technique consists of sending and receiving radiofrequency signals from atomic nuclei that have been immersed in a magnetic field. The strength and homogeneity of the magnetic field dictate which types of measurements are appropriate. With massive superconducting magnets, Magnetic Resonance Imaging (MRI) performs medical imaging by measuring spatially localized NMR signals. In chemistry, similarly gargantuan superconducting magnets are used to perform spectroscopy. These spectra provide a chemical “fingerprint” characteristic of the measured species, and the technique is routinely used to confirm the products of chemical reactions. Specialized spectroscopic measurements provide even more detail about chemical structure, with each resonant nucleus acting as a small antenna transmitting details about the local chemical environment.

For applications such as mapping protein structure, the desire is to increase measurement resolution by building stronger magnets. Recently, there has also been interest in smaller devices with lower magnetic fields of 0.5-2 T, with 0.5 T representing the lower threshold suitable for spectroscopy [1]. Because the measurement of the system’s signal-to-noise ratio (SNR) scales roughly with the magnetic field to the 3/2 power [2], these smaller instruments are not suitable for cutting edge chemical

research. Their decreased cost and increased portability, however, opens up a new range of applications. Desktop and smaller spectrometers are used in labs to monitor the progress of reactions, freeing valuable time on the shared high-field machines [1]. Meat inspectors used desktop spectrometers to differentiate between beef and horse meat, after the 2013 scandal in Britain [3]. NMR relaxometers, which have less stringent requirements for field homogeneity, have likewise found a multitude of uses in various form factors: desktop relaxometers are used in quality assurance [4], a hand-held device was demonstrated to detect bladder cancer cells [5], and the open-faced NMR-MOUSE has been used to probe everything from tires to mummies [6], [7].

For these less-powerful devices, an underlying pattern is evident: each application must be individually scouted and proven. Once it has been shown that the desired information is obtainable, then the significant cost advantage of the miniaturized instruments comes into play. When the cost of the NMR device becomes low enough, it can be mass produced for use in a particular application, such as quality assurance.

To date, research efforts have demonstrated NMR spectroscopic measurements taken in a handheld magnet [8] and miniaturized NMR electronics on a single board or chip [5]. Significant barriers remain, however, to a low cost, portable device. A key challenge is a low-cost solution for a portable NMR magnet. Existing handheld magnets are expensive, difficult to assemble, and the procedure to correct variations in the magnetic field is arduous. Further areas for improvement include reducing power consumption, and making the experiments as simple and automated as possible in order to increase accessibility to unskilled users. To address these challenges is the objective of this thesis.

The remainder of this chapter introduces basic NMR concepts. Chapter 2 describes the desktop-sized spectrometer that was constructed in order to evaluate miniature magnets and experimental concepts. Chpater 3 details the design and testing of low-cost, portable NMR magnets. Finally, Chapter 4 explores the use of stochastic experimental techniques in the context of miniature NMR, and presents measurements taken stochastically in an inhomogeneous magnetic field.

1.2 Principles

The following section briefly presents the principles necessary to understand this thesis. More thorough explanations are available using quantum mechanics described in [2] and using classical mechanics in [9].

1.2.1 Spin

NMR signals can be measured from atomic nuclei that have spin [2]. Spin is a form of angular momentum in quantum mechanics. It does not result from any sort of motion or rotation, but is rather an intrinsic property of elementary particles. Even though spin does not arise from rotation, it affects the behavior of the particle in the same way as if it did. Thus, spin is considered part of the total angular momentum.

Because spin is a quantum mechanical property, it is allowed to take discrete values. Permitted values are integers (1, 2, 3...) and half-integers (1/2, 3/2, 5/2...) [2]. For example, the nucleus of ^1H is a single proton, and has a spin of 1/2. The nucleus of ^2H is a proton and a neutron, and has a spin of 1. In every nucleus, the spin from the component protons and neutrons will add or cancel in order to find the lowest energy configuration. In some cases, the spin of the protons and neutrons will exactly cancel and the nucleus will have zero net spin. This is the case for many isotopes abundant in organic substances: ^{12}C , ^{16}O and ^{32}S . However, most atomic nuclei do have spin. Two abundant nuclei with strong NMR signals are ^1H and ^{19}F , both with spin 1/2.

A spin of value S has $(2S+1)$ available configurations, called substates. Thus, spin-1/2 particles, for example, has two available substates, called spin up and spin down. In the absence of a magnetic field, all of the substates have equal energy, and there is no preferred configuration [2].

1.2.2 Magnetic Moment

Any nucleus with spin also possesses an intrinsic magnetic moment. The laws of quantum mechanics require that the strength of the magnetic moment be proportional

to the spin. For nuclei, this proportionality constant is called the gyromagnetic ratio, γ . In the language of quantum mechanics [2]:

$$\hat{\mu} = \gamma \hat{S}, \quad (1.1)$$

where the hats denote quantum mechanical operators.

A bar magnet such as a compass will rotate to align with an external magnetic field. The angular momentum and magnetic moment of a spin in a magnetic field will work together to create a different motion: rather than aligning with the field, the spin will *precess* about the axis of the field [2]. A spin tilted at an angle α from the magnetic field will rotate about the field while maintaining this angle α , sweeping out a cone (Fig. 1-1).



Figure 1-1: The nuclear magnetic moment, represented by small arrow, will precess about an external magnetic field, represented by the large arrow. Figure reproduced from [10].

The frequency of precession is called the Larmor frequency, and is proportional to the strength of the magnetic field B_0 scaled by the gyromagnetic ratio [2]:

$$\omega_0 = -\gamma B_0, \quad (1.2)$$

where ω_0 is the Larmor frequency. The negative sign in the equation above means that, for a positive gyromagnetic ratio, the spin will precess clockwise around the axis of the magnetic field. The gyromagnetic ratio of ^1H is $267.522 \text{ rad s}^{-1} \text{ T}^{-1}$, which means that the spin vector will complete over 40 million rotations per second in a 1 T field.

In the absence of a magnetic field, the spin and magnetic moment vectors are equally likely to point in any direction. When a magnetic field is applied, the degeneracy is broken, and allowed states with a magnetic moment that is aligned with the external field are slightly lower energy than states that oppose the field. This energy difference scales with the strength of the magnetic field, and the spins are biased towards lower energy states. The relative populations of the spin states depend on the ratio of magnetic and thermal energies. At room temperature, this bias is very small: for 10,000 spins in a field of 3 T, the state aligned with the field will have about one more spin than the state against the field [9]. Nevertheless, NMR samples routinely have 10^{20} spins, and the bias is sufficient to create a net magnetic moment aligned with the external magnetic field.

Compared to the precession of the spins, the development of the net magnetic moment is quite slow. As the spins precess, the angle between the spin vector and the magnetic field remains constant. Over time, small fluctuations in the magnetic field will cause the angle between the spin and magnetic field to slowly change. The spin vector will sample all possible directions, but will show a small preference towards aligning with the magnetic field, as discussed above. After being placed in a magnetic field, a sample will develop a net magnetic moment as the spins preferentially align with the external field. The growth of the net magnetic moment follows an exponential curve with time constant T_1 (Fig. 1-2), called the *longitudinal relaxation time constant*. This time constant is affected by temperature and viscosity of the sample, and is generally on the order of milliseconds to seconds, or even longer [2].

T_1 is the characteristic timescale for the spin system to come to equilibrium after any perturbation, and limits how rapidly NMR experiments can be repeated.

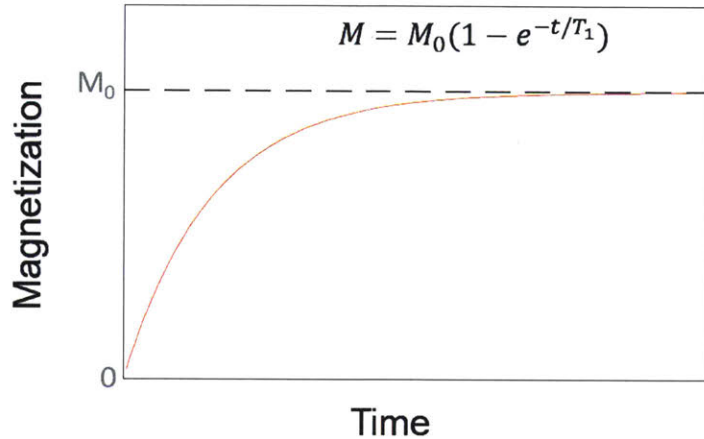


Figure 1-2: A net magnetization in a sample of spins will develop when placed in an external magnetic field, approaching equilibrium with characteristic timescale T_1 .

1.2.3 Radiofrequency Pulses

When a sample of spins is placed in a magnetic field, it develops a net magnetic moment aligned with the field, called longitudinal magnetization. It is not practical, however, to directly measure longitudinal magnetization. Instead, in NMR measurements, the *transverse* magnetization is measured—that is, the component of the magnetic moment *perpendicular* to the magnetic field.

Radiofrequency (rf) pulses whose frequency closely matches the Larmor frequency will tip the net magnetic moment away from the external field B_0 . The amount of rotation caused by the rf pulses is called the *flip angle*, and is proportional to both the strength and duration of the rf pulse [2]:

$$\beta_p = \omega_{nut} \tau_p, \quad (1.3)$$

where β_p is the flip angle, τ_p is the pulse duration, and ω_{nut} is the nutation frequency. The nutation frequency scales with the strength of the rf pulse [2]:

$$\omega_{nut} = \left| \frac{1}{2} \gamma B_{rf} \sin \theta_{rf} \right|, \quad (1.4)$$

where γ is the gyromagnetic ratio, B_1 is the peak value of the oscillating rf field, and

θ_1 is the angle between B_0 and the rf field.

This effect is the *resonance* in nuclear magnetic resonance. The static field B_0 is orders or magnitude larger than the oscillating rf field. Yet if the oscillating field is applied at the same frequency as the spin precession—their resonant frequency—then the small rf field can have a large effect on the spin state.

The duration of the rf pulse determines the range of frequencies excited. For a pulse of length T , a bandwidth of $1/T$ is excited. For example, a 1 ms pulse will excite a 1 kHz bandwidth. The excited band in the frequency domain is the Fourier transform of the pulse sent in the time domain. In the time domain, the excitation pulse is a box function multiplied by an infinite sine wave. In the frequency domain, therefore, the pulse is the convolution of these two components, after each has been Fourier transformed. The box function transforms to a sinc function, and the sine wave to a delta function at the excitation frequency. Convolving the two gives a sinc function centered at the excitation frequency. A shorter pulse in the time domain gives a wider sinc in the frequency domain.

1.2.4 Free Induction Decay

After being tilted away from the B_0 field, the net magnetization will precess at the Larmor frequency, because each of its component spins will also be precessing at that frequency [2]. This rotating transverse magnetization generates a rotating magnetic field, which can be detected using a coil of wire (Fig. 1-3). As the magnetic moment rotates, the magnetic flux through the coil changes with time, inducing a voltage in accordance with Faraday's law:

$$\epsilon = -N \frac{d\Phi_b}{dt}, \quad (1.5)$$

where ϵ is the electromotive force, N is the number of turns in the coil and Φ_B is the magnetic flux through the coil.

The NMR spectrometer is able to detect and record the oscillating voltage in the coil, which is called the *Free Induction Decay* (FID).

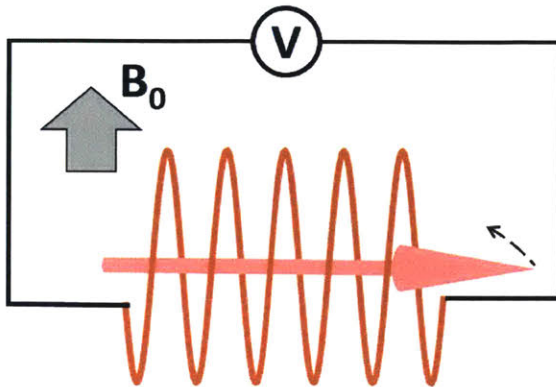


Figure 1-3: The net magnetic moment rotates in the transverse plane, inducing a voltage in a measurement coil.

As the net magnetization precesses, microscopic fluctuations in the magnetic field B_0 will perturb the rotation of individual spins, causing them to fall out of alignment with the group. The spins will become more and more out of phase, causing the NMR signal to decay. This decay follows once again an exponential curve, this time with time constant T_2 , the *transverse relaxation time constant*. In liquids composed of small molecules, T_2 will be about as long as T_1 , while in solids it will be significantly shorter [2].

The FID will look like an oscillating signal, due to the varying magnetic flux through the detection coil, modulated by a T_2 decay envelope, as shown in Fig. 1-4.

1.2.5 Inhomogeneous Magnetic Field

If the magnetic field B_0 has spatial variations, the resonant Larmor frequency will vary across the sample. At the start of the FID, all the spins of the sample will be in phase. Because different spins precess at different frequencies, however, their summed signal will quickly decay. Fig. 1-5 illustrates how the sum of sinusoids of different frequencies decays more quickly than the individual components.

The observed decay rate in an inhomogeneous field is given a new name: T_2^* . The value of T_2^* is less than or equal to T_2 , and is dependent of both T_2 and the field variations via the following equation [11]:

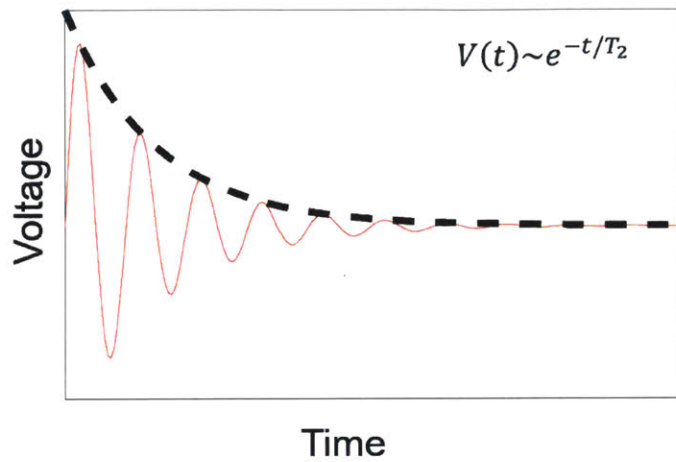


Figure 1-4: The measured NMR signal after an excitation pulse is called the Free Induction Decay. It oscillates due to the rotating magnetic moment, and slowly decays with time constant T_2 as the spins lose coherence.

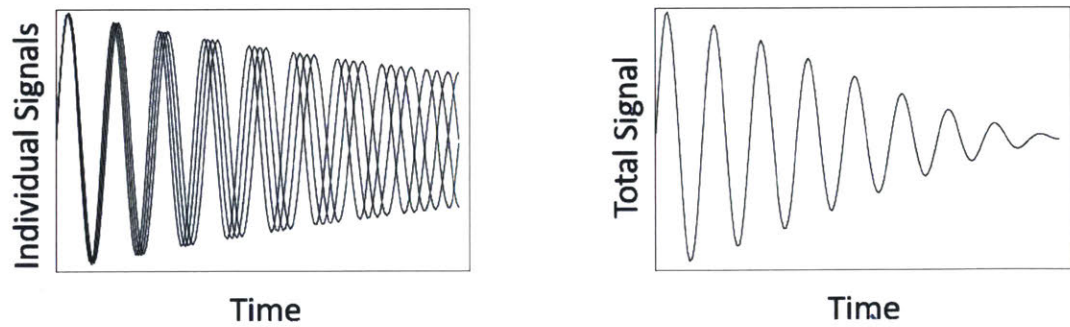


Figure 1-5: Summed sinusoids of slightly different frequency decay more rapidly than the individual components, much like the net signal of spins in an inhomogeneous magnetic field.

$$\frac{1}{T_2^*} = \frac{1}{T_2} + \gamma \Delta B. \quad (1.6)$$

For large variations in the magnetic field, the contribution of T_2 to T_2^* becomes negligible, and the observed decay rate becomes a good measure of the magnetic field variation ΔB .

1.2.6 NMR Spectra

The NMR spectrum is computed by taking the Fourier transform of the FID. A simple NMR spectrum is shown in Fig. 1-6.

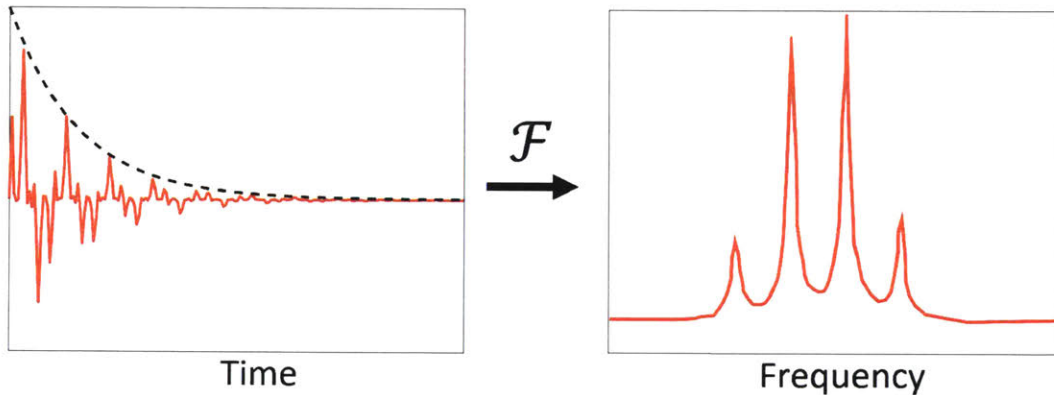


Figure 1-6: Fourier transform of the FID yields the NMR spectrum, with spectral peaks characteristic to the measured sample.

In general, the resonant frequencies of different nuclei vary widely, and the spectrometer is tuned to measure only one nuclear species at a time [2]. Even in measurements of a single isotope, however, multiple spectral peaks occur due local shifts in the magnetic field caused by nearby electrons and other magnetic nuclei. For example, in a molecule, the electron cloud is not evenly distributed among the nuclei. In a phenomenon known as chemical shielding, nuclei surrounded by a denser cloud of electrons will have their resonant frequency shifted to a lower frequency, while nuclei with less electron density will resonate at a higher frequency. Chemical shielding and other effects on the local magnetic field at a nucleus create characteristic spectra that

allow chemists to characterize the molecules of their sample.

Peak width gives a measure of T_2 : at half-height, the width in Hertz is equal to $1/(\pi T_2)$. In an inhomogeneous B_0 field, the Larmor frequency varies across the sample, and the peak in the frequency domain widens in a phenomenon known as inhomogeneous broadening. In this case, the width of the peak at half height gives a measure of T_2^* , rather than T_2 [2]. Inhomogeneous broadening can cause the peaks to overlap and obscure the spectrum, as depicted in Fig. 1-7.

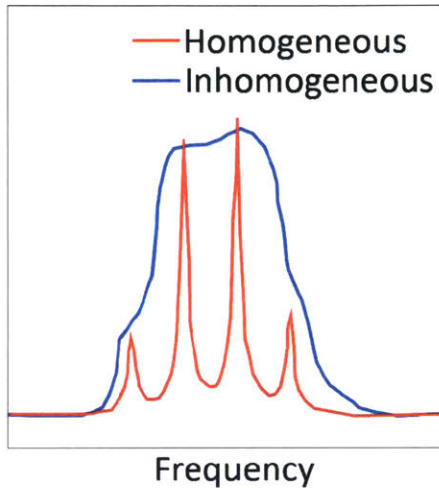


Figure 1-7: The spectral peaks widen in an inhomogeneous field, obscuring the spectrum.

A key challenge in NMR is to create a homogeneous magnetic field in order to measure clean spectra.

1.2.7 A Simple NMR Experiment

To consolidate the above concepts, consider the sequence of steps to perform a simple NMR measurement. After being placed in the magnetic field, the sample of spins develops a net magnetic moment aligned with the field. A 90° pulse flips the net magnetization into the transverse plane, where it rotates at the Larmor frequency. The receiver electronics are briefly saturated by the large excitation pulse, but after this *dead time*, the electronics recover and are able to record the voltage the FID induces in a nearby wire coil. Fourier transform gives the NMR spectrum. After

the rf pulse, the net magnetization slowly realigns with the B_0 field, following an exponential curve with time constant T_1 . After waiting about four times the length of T_1 , the magnetization will have fully recovered, and the experiment can be repeated to allow for averaging.

Experiments that record and perform the Fourier transform on the FID after a pulse or pulses are known at Fourier transform (FT) NMR. FT NMR is the most common type of experiment in current use.

1.2.8 Rotating Frame

Modeling the dynamics of the spins is mathematically simpler in a rotating reference frame [2]. In the rotating frame, the observer will rotate around the B_0 field with the spins. If the frame rotates at the Larmor frequency, then the spin vector appears stationary. If the frame rotates at 20 MHz, and the Larmor frequency is 20.000001 MHz, then the spin vector appears to rotate at 1 Hz. Any frequency ω in the stationary reference frame is shifted in the rotating frame to the relative frequency called Ω :

$$\Omega = \omega - \omega_{ref}. \quad (1.7)$$

The difference between the reference frequency and the Larmor frequency is called the *resonance offset*, and is given by

$$\Omega_0 = \omega_0 - \omega_{ref}. \quad (1.8)$$

NMR spectra are routinely plotted at the offset frequency.

1.2.9 Bloch Equations

Originally proposed by Felix Bloch in 1946 [12], the Bloch Equations model the motion of the magnetization vector in a spin-1/2 system. The model accounts for rf radiation, relaxation, and precession in the rotating frame. As shown below, the equations

account for the time evolution of the x , y , and z components of the magnetization vector. By convention, the B_0 field is chosen to point in the z -direction. The equations are as follows:

$$\frac{dM_x}{dt} = -\Omega_0 M_y + \gamma B_1 \sin \phi M_z - \frac{1}{T_2} M_x, \quad (1.9)$$

$$\frac{dM_y}{dt} = -\Omega_0 M_x - \gamma B_1 \cos \phi M_z - \frac{1}{T_2} M_y, \quad (1.10)$$

$$\frac{dM_z}{dt} = -\gamma B_1 \sin \phi M_x + \gamma B_1 \cos \phi M_y - \frac{1}{T_1} (M_z - 1), \quad (1.11)$$

where B_1 denotes the strength of the rf radiation and ϕ is the phase of the rf field with respect to the x -axis.

In 4.2, the exact solution to the Bloch equations will be used to model the behavior of a spin when excited by an extended sequence of pulses.

1.2.10 Quadrature Detection

The NMR signal occurs at high frequencies, typically hundreds of megahertz for superconducting spectrometers. This high-frequency signal is challenging to directly record with an analog to digital converter (ADC), and filtering to pass only the narrow frequency band where the signal is located is likewise untenable. By mixing down to a lower frequency, the signal can be tightly filtered and easily recorded using unspecialized electronics.

The NMR signal is shifted to a lower frequency by multiplication with a reference signal which oscillates close to the Larmor frequency. To retain the full information in the NMR signal, it is necessary to split the signal into two channels and multiply each by the reference signal, but with one reference signal shifted 90° relative to the other [13].

If the received NMR signal is given by

$$s''(t) = 2s_0 \cos(\omega_0 t), \quad (1.12)$$

and the reference signals by

$$s'_x(t) = \cos(\omega_{ref}t - \phi), \quad (1.13)$$

$$s'_y(t) = \sin(\omega_{ref}t - \phi), \quad (1.14)$$

then the product of the two will be, using trigometric identities, the sum and the difference frequencies:

$$s'_x(t)s''(t) = s_0\cos[(\omega_0 + \omega_{ref})t - \phi] + \cos[(\omega_0 - \omega_{ref})t + \phi], \quad (1.15)$$

$$s'_y(t)s''(t) = s_0\sin[(\omega_0 + \omega_{ref})t - \phi] + \sin[(\omega_0 - \omega_{ref})t + \phi], \quad (1.16)$$

where ω_0 is the Larmor frequency, ω_{ref} is the reference frequency, ϕ is the phase of the reference frequency, and $2s_0$ is the initial signal amplitude. By passing the product signals through a low-pass filter, the sum frequencies are filtered out and only the difference frequencies remain, though half the signal intensity is lost in this step. This difference frequency is equivalent to the relative frequency Ω . The complex sum of the two components gives the quadrature receiver signal, which contains the magnitude and phase in the rotating frame:

$$s^+(t) = s_x(t) + i \cdot s_y(t) = s_0 e^{i(\Omega_0 t + \phi)}. \quad (1.17)$$

Thus, quadrature detection is able to acquire all the information from the NMR signal by measuring two low-frequency channels [13].

Chapter 2

NMR Spectrometer Construction

At its core, an NMR spectrometer is a device that creates a net magnetic moment of spins, uses rf pulses to flip the net magnetization, and records the free induction decay (FID). Chapter 3 discusses the design of a portable magnet to polarize the sample. In this chapter, the electronics to generate the rf pulses and record the FID are detailed.

NMR electronics on a single chip have already been demonstrated [5], and it was not the objective of this work to reproduce that achievement. To allow complete control and customization, a spectrometer was built, sized to fit on a desktop or cart. As shown in the diagram below, the basic design is composed of three parts: a probe, which contains the sample and is placed inside the magnet, as well as transmitter and receiver electronics which are alternately connected to the probe via a transmit/receive (T/R) switch (Fig. 2-1).

Section 2.1 describes the probe, Section 2.2 the transmitter electronics, and Section 2.3 the receiver pathway. Section 2.4 details how the experiments were controlled and recorded using LabVIEW [14] and a myRIO device. Finally, Section 2.5 shows NMR signals recorded using the spectrometer, with an electromagnet providing the B_0 field.

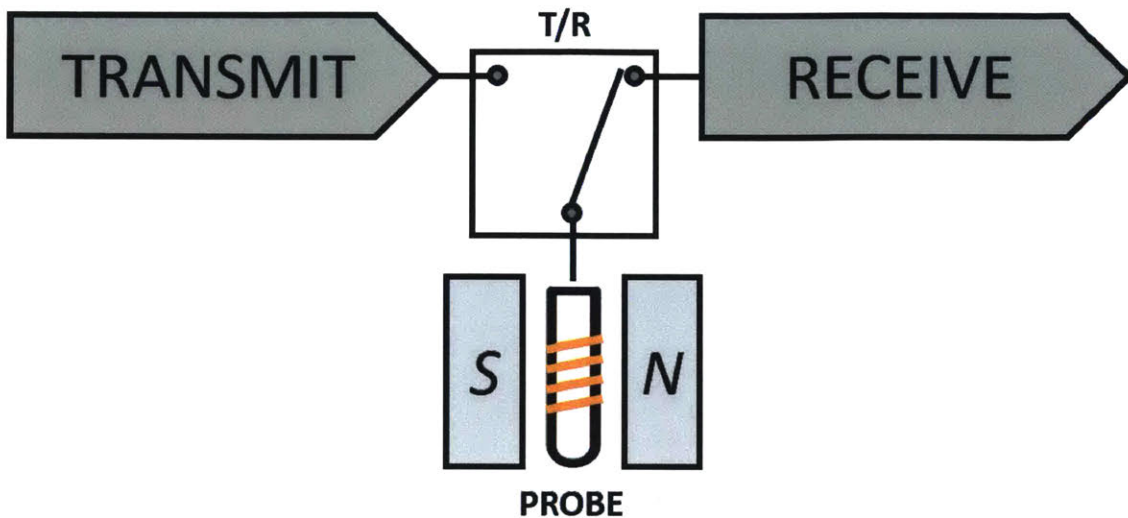


Figure 2-1: In the NMR spectrometer, the sample-containing probe is alternately connected to the transmit and receive paths via a transmit/receive switch.

2.1 NMR Probe

The NMR probe positioned the sample in the homogeneous B_0 field of the magnet. It contained a coil of wire which was used to transmit and receive the rf signals. To build the probe, magnet wire was wound directly around the glass sample tube and secured with a small amount of cyanoacrylate, as shown in Fig. 2-2.

A solenoidal coil is commonly used in NMR because it generates a homogeneous rf field while allowing a large fill factor [15]. Fill factor, the fraction of volume in the coil made up of the sample, is maximized by winding the wire directly around the sample tube [16]. A large fill factor increases the coil sensitivity and signal to noise [17].

Signal to noise also increases with the quality factor Q of the coil, which is given by [16]

$$Q = \omega_0 \frac{L}{r}, \quad (2.1)$$

where ω_0 is the Larmor frequency in rad/s, L is the coil inductance, and r is the coil resistance. Maximizing Q requires balancing the inductance and resistance. The

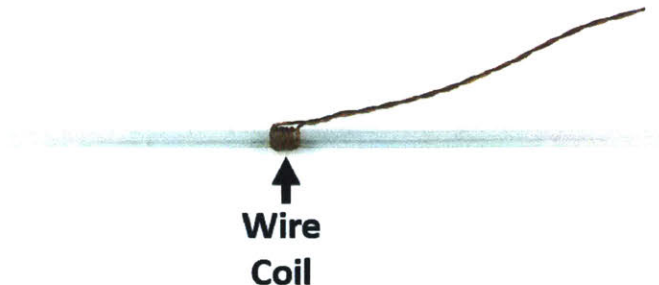


Figure 2-2: Wire wound directly around the sample tube is able to excite the sample and receive the NMR signal.

inductance increases with the number of turns, but to maintain a given coil size, more turns mean a smaller wire gauge and higher resistance. A good rule of thumb is that the coil height should be approximately equal to the diameter, and the spacing between the turns should be equal to the wire diameter. Q increases slowly for longer lengths, but decreases dramatically for shorter ones [16].

NMR signals were measured using coils of two sizes. The larger coil used 24 gauge (0.51 mm) magnet wire wound around a sample tube with 2.5 mm outer diameter (OD). The coil had 5 turns and a measured inductance of 120 nH and resistance of 200 m Ω , giving it a Q of 75 at 20 MHz. The smaller coil had 5 turns of 23 gauge (0.58 mm) wire wrapped around a 1.7 mm OD sample tube. The inductance was measured as 75 nH, and the resistance as 90 m Ω , giving a Q of 105 at 20 MHz.

A second 1.7 mm inner diameter (ID) coil of the identical geometry was fixed to the interior of a cylinder guide, allowing the sample tubes to be easily inserted and removed. This improvement allowed rapid testing of a series of samples while maintaining equivalent performance.

To interface with the transmitter and receiver electronics, the probe required a matched 50 Ω impedance. Otherwise, a fraction of the power would be reflected instead of transmitted across the boundary. A tank circuit, composed of capacitors

in series and parallel with the wire coil (Fig. 2-3), matched the impedance to 50Ω at the Larmor frequency.

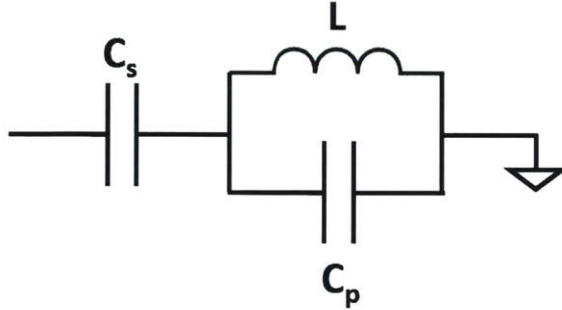


Figure 2-3: Series and parallel capacitors are used to impedance match the inductive probe coil at the Larmor frequency.

The inductance and resistance of the coil were set by the coil geometry, and the values of the capacitors were chosen as follows. The coil and parallel capacitor were considered first, with the capacitor value chosen to make the real impedance 50Ω . The impedance of the parallel capacitor and coil is given by

$$Z_{par} = \left(\frac{1}{i\omega_0 L + r} + i\omega_0 C_p \right)^{-1}, \quad (2.2)$$

where Z_{par} is the impedance of the parallel inductor and capacitor, C_p is the parallel capacitance, and r is the resistance of the coil wire. With the value of C_p chosen to set the real impedance at 50Ω , the role of the series capacitor was to cancel the remaining imaginary impedance at the frequency of interest. This canceling was accomplished by choosing the impedance of the series capacitor to be equal in magnitude to the imaginary parallel impedance:

$$\frac{1}{\omega_0 C_s} = \Im(Z_{par}), \quad (2.3)$$

where C_s is the series capacitance. The Bode plot in Fig. 2-4 below shows the impedance for an example circuit where the coil inductance and resistance were measured to be $1.25 \mu\text{H}$ and $400 \text{ m}\Omega$, and the resonant frequency was 24.25 MHz . The calculated values for parallel and series resistance were $C_p=31 \text{ pF}$ and $C_s=3 \text{ pF}$. The

impedance matched at the desired frequency, but only at that frequency: the values of the capacitors required retuning if the resonance changed significantly.

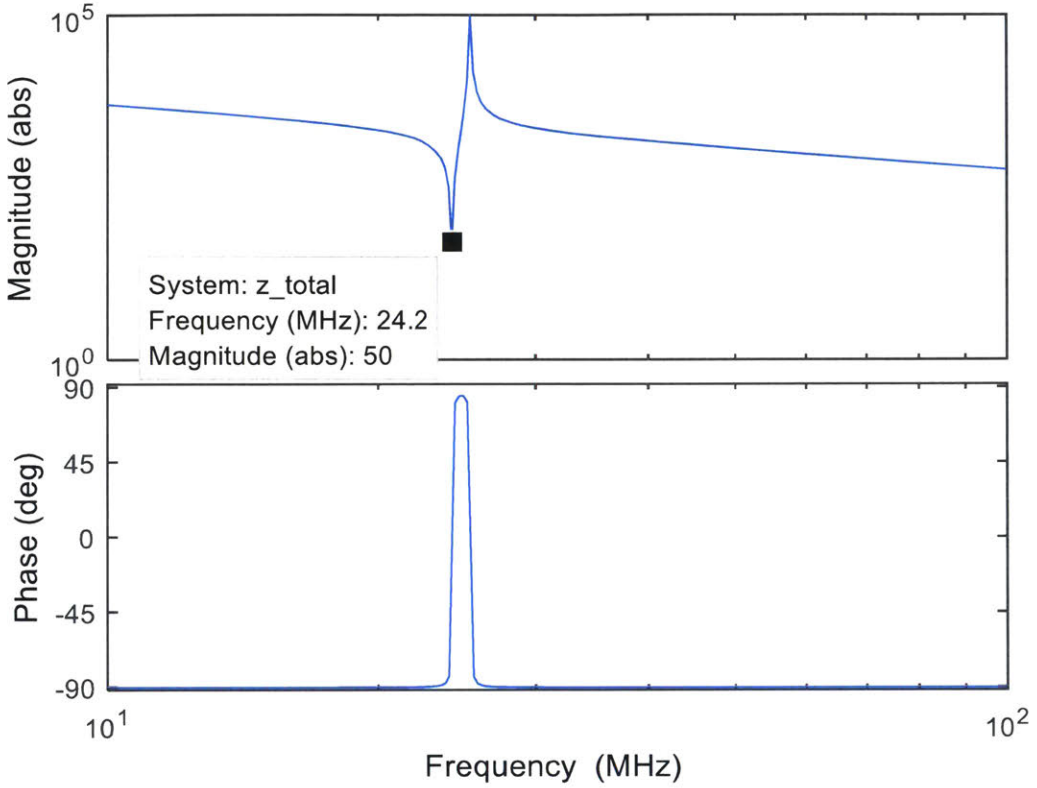


Figure 2-4: The Bode plot of the series-parallel tank, simulated in MATLAB [18], shows that the impedance is matched in the narrow band around the Larmor frequency.

Although the tank circuit impedance is a function of both capacitor values, the resonant frequency is more strongly coupled to the parallel capacitor, while the magnitude at resonance is more strongly coupled to the series capacitor. Thus, with variable capacitors, the two parameters could be fine-tuned independently.

The tank circuit was realized using a custom printed circuit board (PCB). It was found that it was sufficient to twist the leads from the coil and solder them directly to the board. Ceramic capacitors (Series 1111N; Passive Plus Inc., NY) were used for the parallel and series capacitance and behaved well at the high frequencies. Adjustable

capacitors with a range of 7 to 50 pF (TZ Series; Murata Electronics) were placed in parallel with the fixed capacitors to allow fine tuning of the resonant frequency and impedance. The tank circuit PCB is shown in Fig. 2-5.

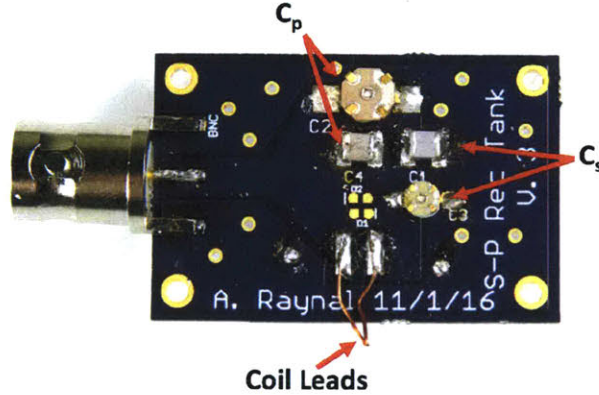


Figure 2-5: The parallel-series tank was realized on a custom PCB, to which the wire leads from the sample coil were directly soldered.

The impedance of the tank circuit measured on an impedance analyzer (4194A; Hewlett-Packard, CA) closely matched the simulation predictions, as seen in Fig. 2-6.

Tuning of the tank circuit was most easily accomplished using a network analyzer (E5071C; Agilent Technologies, CA) by looking at the S_{11} parameter. This parameter, which measures reflected power, sharply dips when the power is transmitted. The adjustable capacitors were tuned so that the drop in the S_{11} value was at the frequency of interest and as steep as possible.

2.2 Transmitter Pathway

In the transmitter pathway (Fig. 2-7), the rf excitation pulses were routed from a waveform generator (33500B Series Waveform Generator; Keysight Technologies, CA). The continuously running rf signal was gated by two active switches in series (ZYSWA-2-50DR+; Mini-Circuits, NY). The second switch served as the T/R switch and toggled the probe between the transmitter and receiver pathway. The first switch, while identical, served only to provide additional isolation between the rf excitation

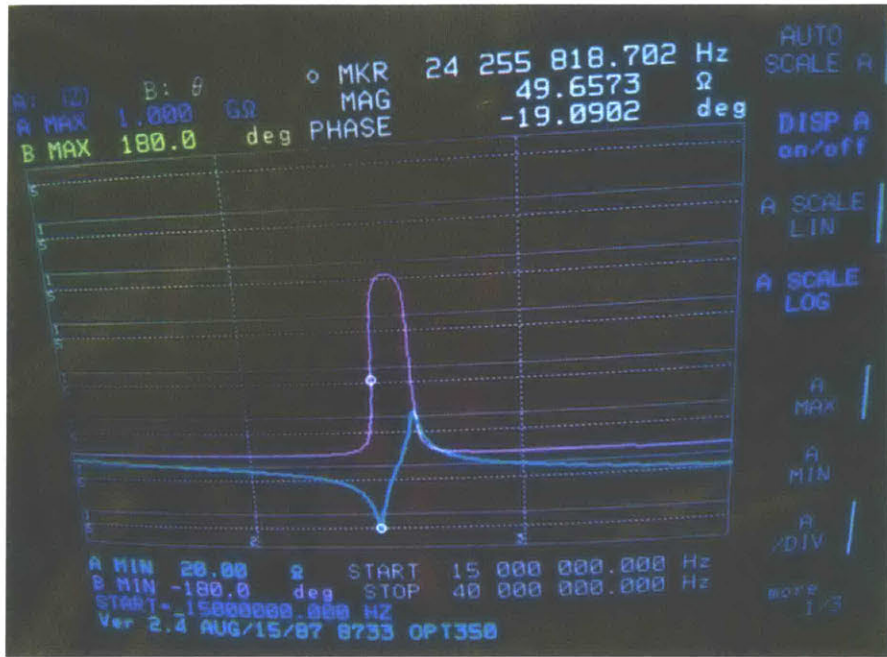


Figure 2-6: The impedance of the tank circuit, measured on an impedance analyzer, closely matches the simulated form.

and the receiver electronics. A small 0.7 W amplifier (MHW592; Motorola Solutions, IL, Fig. 2-8) was used in experiments employing 90° pulses, but low-power experiments did not require any amplification and the waveform generator signal was used directly.

2.3 Receiver Pathway

The receiver pathway measured the microvolt-level NMR signal and amplified it six orders of magnitude to be recorded by an ADC. The pathway used quadrature detection to record the NMR signal via two low-frequency channels, as described in Section 1.2.10. These channels were the real an imaginary parts of the NMR signal recorded at the relative frequency Ω . Fig. 2-9 below diagrammatically shows the receiver section of the spectrometer.

The receiver path started immediately after the T/R switch, where a low-noise preamplifier (AU-1467; L3 Narda-MITEQ, NY) amplified the voltage 2500 times. The

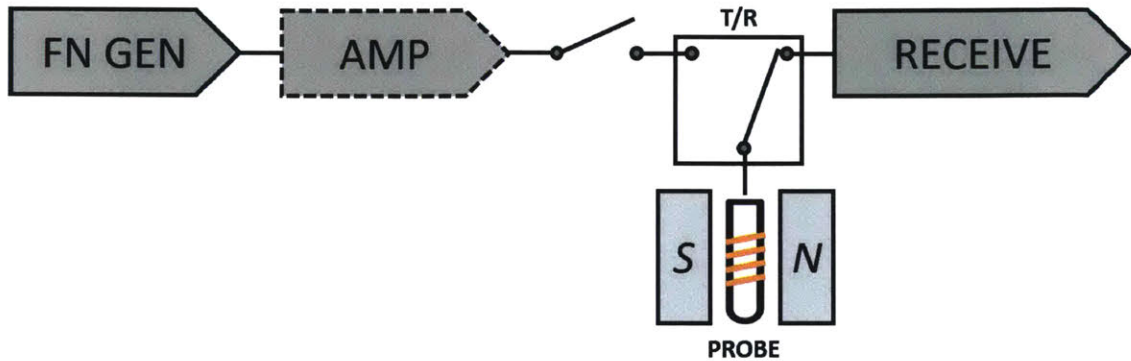


Figure 2-7: The transmitter pathway used a function generator to create the excitation signal, a small amplifier to boost the power if needed, and two switches with 50 dB isolation each to provide sufficient separation from the receiver electronics.



Figure 2-8: A small 0.7 W amplifier, kindly given by the Martinos Center from their Instructional Tabletop MRI [19], was used to amplify the transmit pulses for some experiments.

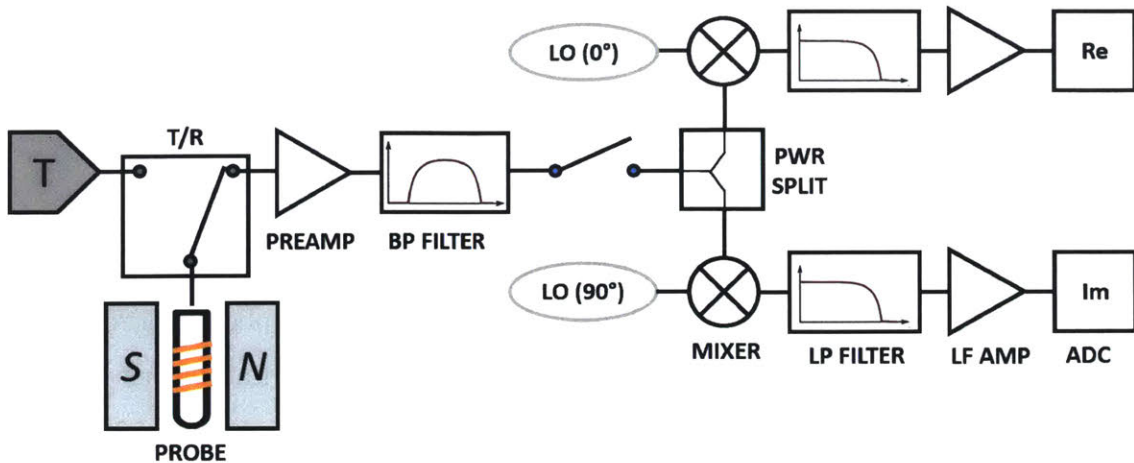


Figure 2-9: In the receiver pathway, a low-noise preamplifier boosted the tiny NMR signal. A bandpass filter passed the resonant frequency and screened out noise. The signal power was split into two paths, and each path was multiplied by a local oscillator (LO). Low-pass filters screened for the difference frequency, and low-frequency (LF) amplifiers further amplified the signal before recording by ADCs.

preamplifier was ideal for NMR measurements, with its high gain, low noise figure of 1.2 dB, and 1 μ s recovery time after saturation. As the preamp would saturate during the excitation pulses, the fast recovery time was key to minimizing the dead time before the NMR signal could be recorded.

The preamp was followed by a band-pass filter. Because the NMR signal occurs in a known narrow frequency band, the SNR can be improved by filtering around this frequency. For most experiments the resonance was close to 20.5 MHz, and the filter passband ranged from 20 MHz to 21 MHz (BBP-20R5+; Mini-Circuits). Preamplifier and band-pass are shown in Fig. 2-10.



Figure 2-10: The NMR signal was amplified by a low noise preamplifier and sent through a band-pass filter.

Because the preamp recovered more quickly from the excitation pulses than did

the downstream electronics, another switch (ZYSWA-2-50DR+; Mini-Circuits) was used after the band-pass filter. This switch provided isolation from the excitation pulses that leaked through the T/R switch, which were initially small but became problematic after amplified by the sensitive preamp.

Next a power splitter (PSC-2-1+; Mini-Circuits) divided the signal into two pathways for quadrature detection. In each path, the signal was multiplied by a reference local oscillator (LO) which ran at the same frequency as the excitation pulses. The LO signal was generated by a second channel of the same waveform generator used for excitation pulses, and yet another switch (ZYSWA-2-50DR+, Mini-Circutis), not shown in Fig. 2-9, isolated the LO signal from the downstream electronics during the transmit pulses. A power splitter (JSPQ-80+; Mini-Circuits) divided the LO into two channels offset by 90°. Each of the split NMR signal channels was multiplied by one of the LO channels using mixers (SRA-1+; Mini-Circuits). 20 kHz low-pass filters (EF122; Thorlabs, NJ) then selected for the difference frequency between the LO and NMR signal while screening out the sum frequency. The amplitude of each channel was then further amplified by a factor of 800 using a non-inverting operational amplifier circuit. Finally, each channel was fed to a separate 14-bit ADC (LTC1419 with demo board DC200A; Linear Technology, CA). The power splitter, mixers, and low frequency amplifiers are shown in Fig. 2-11.

2.4 MyRIO Controller

The experiments were controlled in real time using a National Instruments myRIO board interfacing with LabVIEW [14]. The digital input/output (DIO) pins on the myRIO were used to control the state of the switches and to read in the values from the ADCs. For precision in timing, the pins were controlled using myRIO's onboard Field Programmable Gate Array (FPGA), a Xilinx Z-7010. The DIO pins updated with every cycle of the 40 MHz clock. The myRIO was chosen to allow the convenience of programming in LabVIEW along with the timing precision provided by an FPGA.

Although the myRIO has multiple analog input channels, the device has only a sin-

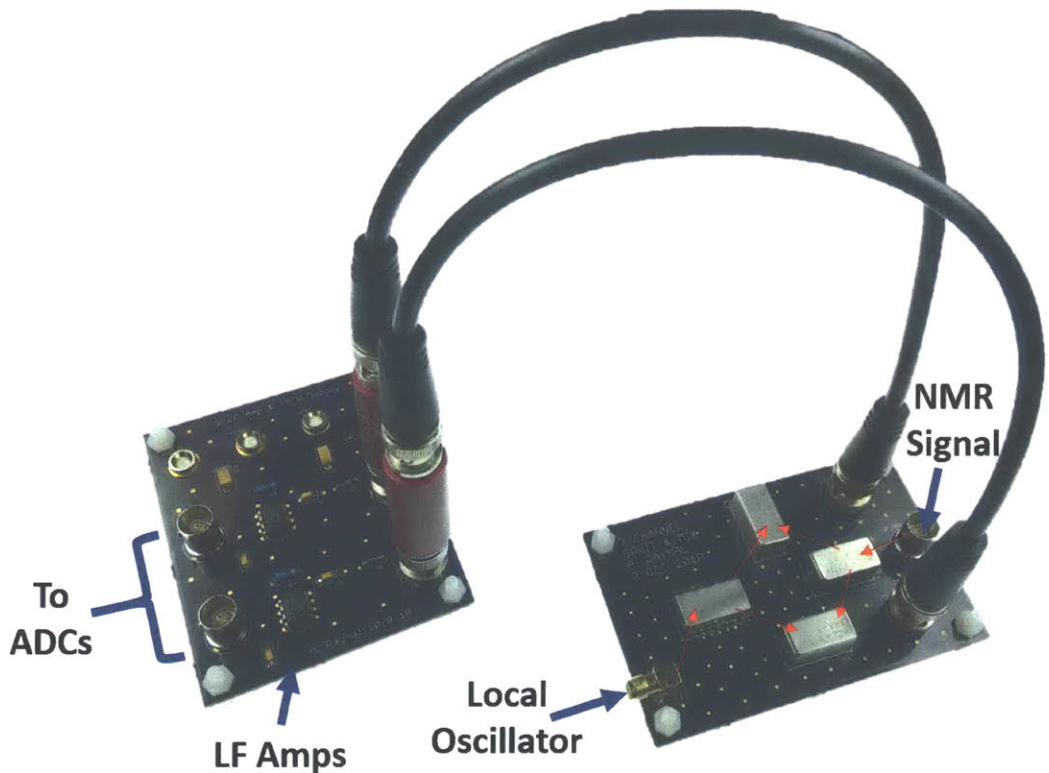


Figure 2-11: Coaxial inputs route the NMR signal and the local oscillator. Each signal is split, as shown by the dark orange arrows, and one branch of the LO is phase shifted by 90° . NMR and LO signals are mixed, then routed through low-pass filters and to low frequency amplifiers before measurement by ADCs.

gle ADC. Values from the analog inputs are not read simultaneously, but instead are offset by a $2 \mu\text{s}$ delay as the ADC sequentially reads the channels. Conventional analysis of NMR signals assumes that the two channels are read simultaneously. Therefore, two external ADCs were used, with the 14 bit measurements fed in parallel to myRIO DIO pins. An additional pin sent a signal to the ADCs to simultaneously start each new measurement. The myRIO with a single external ADC is shown in Fig. 2-12.

LabVIEW block diagrams used to run NMR experiments are included in Appendix A.1.

2.5 Example Measurements

NMR responses to single and double pulses were recorded in order to verify the functionality of the spectrometer. As shown in Fig. 2-13, a water-cooled electromagnet (2H2-45; Applied Magnetics Laboratory Inc, MD) was used to provide the B_0 field, with the current adjusted to set ^1H resonance to 26 MHz, equal to about 0.6 T. The nucleus of the ^1H isotope is a proton, and is one of the most commonly measured NMR species.

Using the 0.7 W amplifier, a $10 \mu\text{s}$ pulse was applied to stimulate the FID in a 2.5 mm sample of water. A paramagnetic salt, manganese chloride, was added to the water in 5 mM concentration to allow the experiment to be repeated 10 times a second, rather than waiting the several seconds required for pure water to relax. The response, recorded on an oscilloscope without mixing down the frequency, is shown in Fig. 2-14.

The decay constant T_2^* in Fig. 2-14 is about $80 \mu\text{s}$. By application of Eq. 1.6, it was found that the magnetic field exhibited a variation of about 80 ppm.

Shown in Fig. 2-15 is the FID after a single pulse, and the spin echo after a refocusing pulse. A series of refocusing pulses is commonly used to measure T_2 relaxation in an inhomogeneous field (see for example [20, 21, 22]). In this case, a $10 \mu\text{s}$, 90° pulse is applied, followed 250 μs later by a 20 μs , 180° pulse.

The same experiment is shown in Fig. 2-16 with a mixer used to downshift the

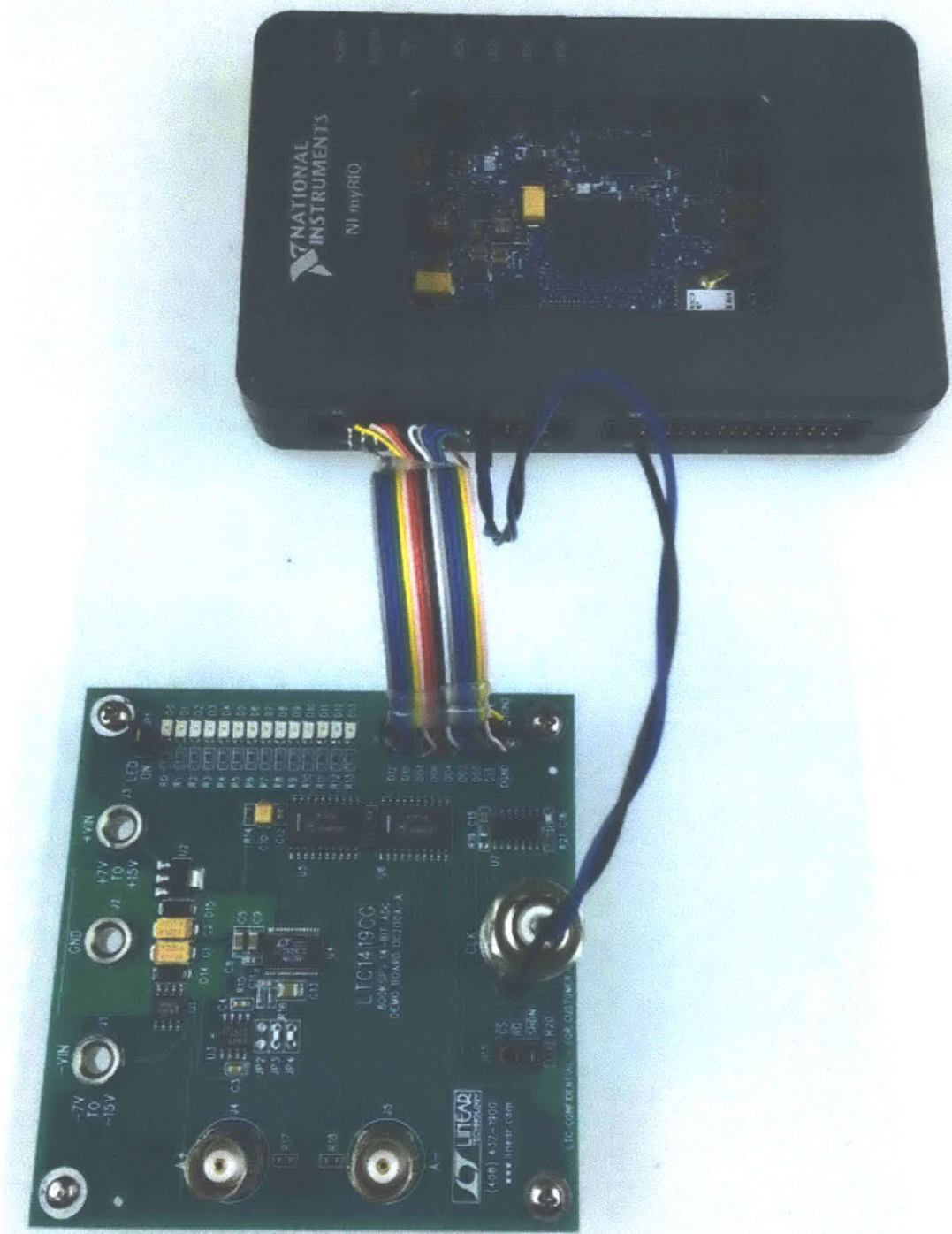


Figure 2-12: External ADCs recorded the NMR signal and passed the 14-bit measurement in parallel to the myRIO.

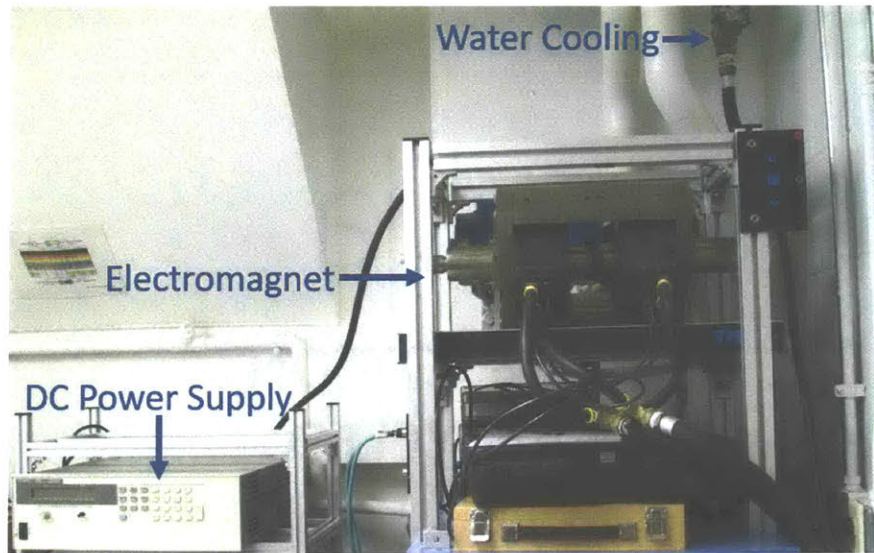


Figure 2-13: The magnetic field created by a water-cooled electromagnet was used to test the functionality of the spectrometer.

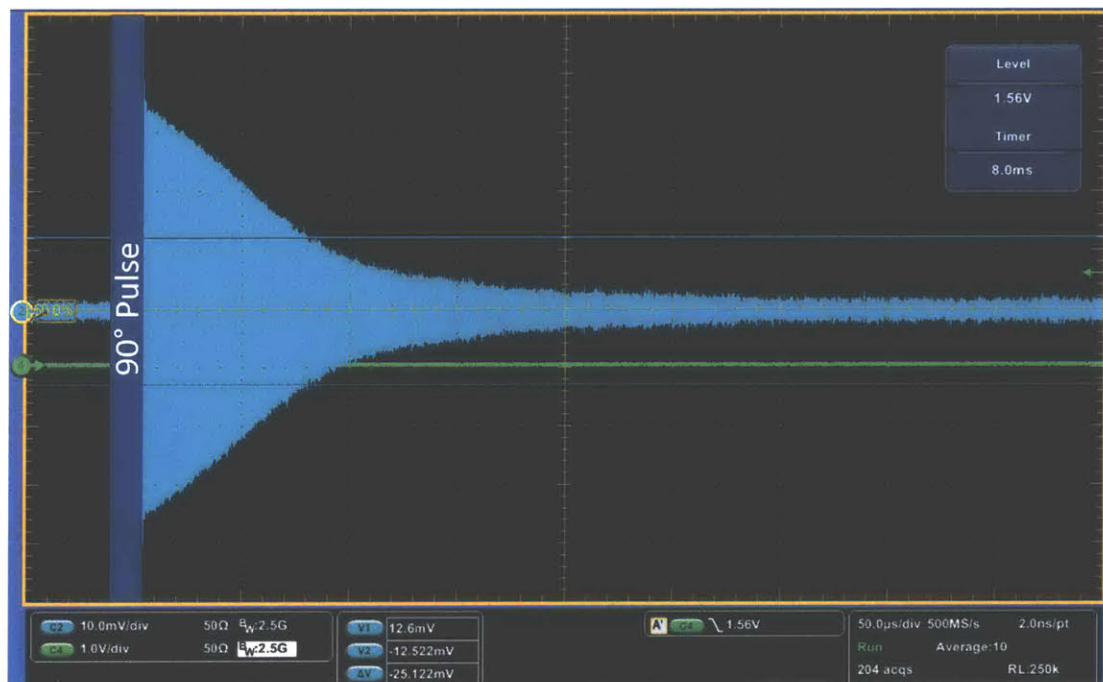


Figure 2-14: The FID taken in the electromagnet, recorded on an oscilloscope with 10 averages, showed that the spectrometer was able to stimulate and capture NMR signals.

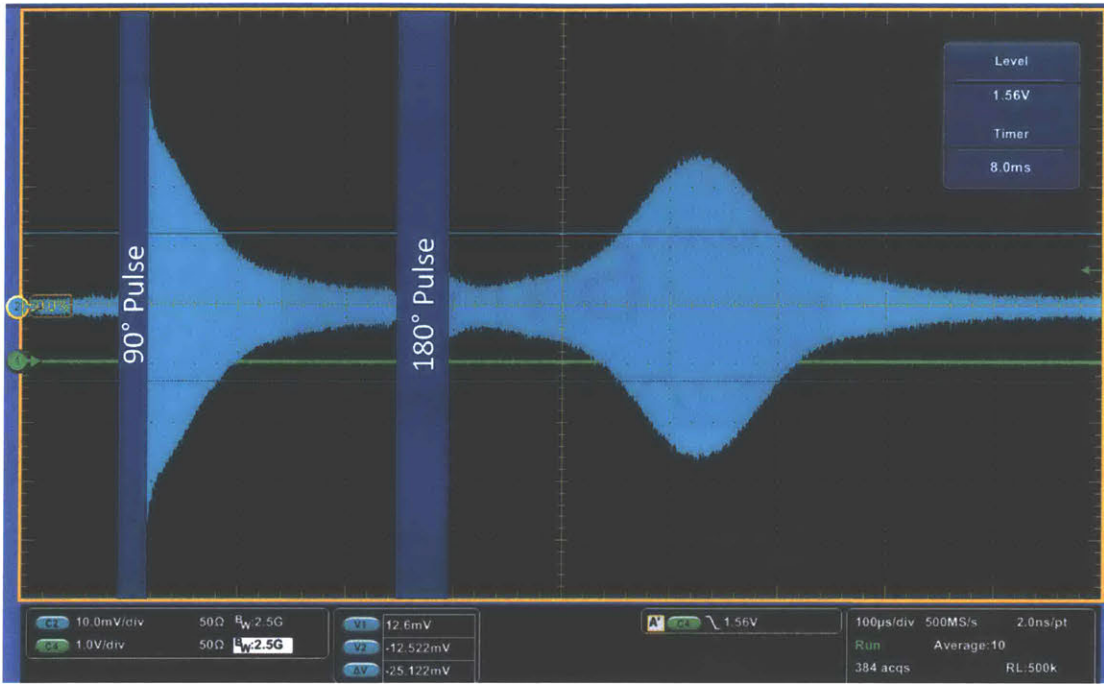
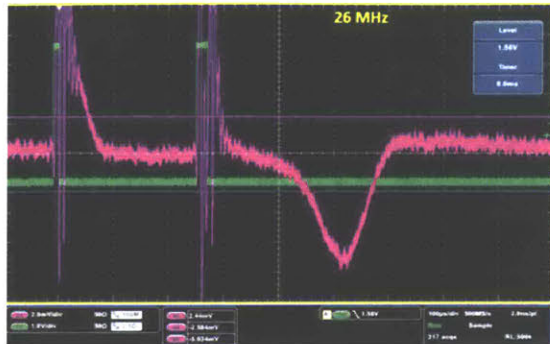


Figure 2-15: The spectrometer was also able to produce a spin echo in the electromagnet by following the 90° pulse with a 180° pulse.

frequency. At 26 MHz in (a) the reference frequency was on resonance, and the output signal contained only very low frequencies. Offsetting the reference frequency 10 kHz in (b) caused the output to oscillate at 10 kHz. Offsetting the reference frequency another 10 kHz in (c) caused the output to oscillate at 20 kHz.

Without using the mixer, the dead time for the receiver electronics to recover after an excitation pulse was about $10 \mu\text{s}$. It was observed that the recovery was slower when the mixer used, increasing the dead time to about $30 \mu\text{s}$. The mixer was the slowest equipment to recover after an excitation pulses, which is why it was chosen to uses switches to block any transmission from the preamp output and the LO during excitation pulses. With both inputs to the mixer gated, the dead time was reduced to under $5 \mu\text{s}$.



(a)



(b)



(c)

Figure 2-16: The measured NMR signal in a pulse echo experiment was multiplied by a reference frequency on resonance at 26 MHz (a), 10 kHz away from resonance at 26.01 MHz (b), and 20 kHz away from resonance at 26.02 MHz (c). After a low pass filter, the NMR signal oscillated at the difference frequency between resonance and the reference frequency.

Chapter 3

Portable NMR Magnet

Superconducting magnets used in NMR spectrometers are unsuitable for portable devices. They are expensive to purchase and maintain, require cryogenic cooling, and are colossal, even requiring a ladder to insert a sample in the bore. Although desktop-sized superconducting magnets are feasible [23], permanent magnets have become the method of choice for small NMR machines. Their simplicity, reduced cost, and minimal maintenance justify their limited field strength, which can go up to about 2 T [8]. Several desktop spectrometers are commercially available, ranging in mass from 5 to 150 kg with field strengths of 1 to 2 T [24, 25, 26, 27]. Smaller magnets have been demonstrated in the literature [28, 29, 6, 11, 30, 31, 20, 5, 32], but are not yet commercially available.

A minimum of 0.5 T is needed to perform NMR spectroscopy [1]. While this field strength is easily achieved with handheld permanent magnets, the challenge is maintaining a sufficiently large region of high field homogeneity. For a given magnet geometry, the ratio between the size of the magnet and the size of the region of homogeneous field remains constant [8]. Some researchers have addressed this issue by shrinking down the size of the sample in order to fill only the small homogeneous region, but this strategy results in decreased signal strength [32]. The alternative to decreasing sample size is to instead correct the variations in the magnetic field. This process, called *shimming*, can be accomplished with carefully placed ferromagnetic material, permanent magnets, or electromagnets. Shimming has allowed researchers

to take measurements using handheld magnets and standard 5 mm OD sample tubes [8].

This chapter explores design solutions for compact NMR magnets. In the first section, various portable magnet designs are compared, and one design is selected that best meets the functional requirements. The selected design, called the shim-a-ring, is optimized and tested in the second section. The third section explores a low-cost strategy for shimming the tested magnet.

3.1 Comparison of Magnet Designs

The functional requirements of a portable NMR magnet are as follows:

1. Low mass: The design must be small and light enough to be handheld.
2. Strong magnetic field: At least 0.5 T is required to perform spectroscopy.
3. Homogeneous: The region of interest should be as homogeneous as possible, or, alternatively, the homogeneous region should be as large as possible.
4. Manufacturability: The raw material and assembly costs should be minimized.

Four permanent magnet designs were evaluated according to these functional requirements. Two are widely used for compact NMR: the iron yoke [32, 33], and the Halbach array [8, 11, 28, 34]. The other two designs are not as well-known, but have particular aspects of interest. The Aubert configuration achieves unusually good homogeneity [30], while the shim-a-ring is notable for its manufacturability [35].

3.1.1 Iron Yoke

The iron yoke (Fig. 3-1) is a standard configuration for NMR magnets. Two magnets are separated by an air gap and oriented such that the magnetic flux travels from one to the other. Steel then completes the magnetic loop, forming the flux return path between the magnets. The steel captures the magnetic flux from the two magnets,

and channels the flux to pass through the small air gap. The NMR sample is placed in the air gap. The magnitude of the B_0 field depends on the size of the air gap, where a smaller gap creates a higher field, and the size of the magnets, where larger magnets create a higher field.

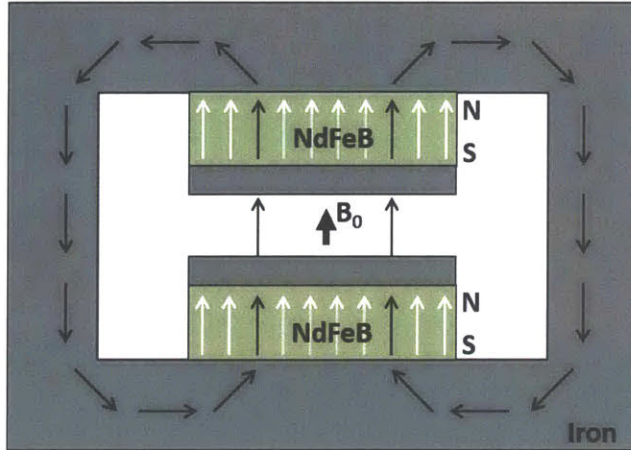


Figure 3-1: The iron yoke uses two permanent magnets and ferromagnetic pole pieces to shape the flux path and create a region of homogeneous field. Figure adapted from [19].

Assembling an iron yoke magnet is challenging due to the strong attraction between the magnets and the iron. A jig must be used to guide the magnets into the desired position and the large forces must be carefully managed.

Magnets of this type used for NMR range in size from about a meter in diameter, in a permanent magnet MRI system [36], all the way down to palm-sized [37]. Because the homogeneous region is so small in the palm-sized magnets, they have been used either for experiments requiring less homogeneity [5], or for spectroscopy with nanoliter-sized samples [32].

3.1.2 Halbach Array

The Halbach array is of interest for compact NMR magnets because the magnetic material itself provides the flux return path, meaning that a stronger field is achieved compared to designs of equivalent mass where steel is used [32]. The cylindrical Halbach array generates an intense magnetic field interior to the bore and no field

outside. The array is composed of an annulus of magnetic material, whose polarization varies sinusoidally. A particular subset of cylindrical Halbach arrays is of interest for NMR because they have the property that the magnetic field within the bore is uniform. The magnetization in this design is given in cylindrical coordinates by [38],

$$\vec{M} = M_r [\cos(\theta - \frac{\pi}{2})\hat{r} + \sin(\phi - \frac{\pi}{2})\hat{\theta}], \quad (3.1)$$

where M_r is the magnetic remanence and θ is the rotation around the cylinder. The design is illustrated in Fig. 3-2.

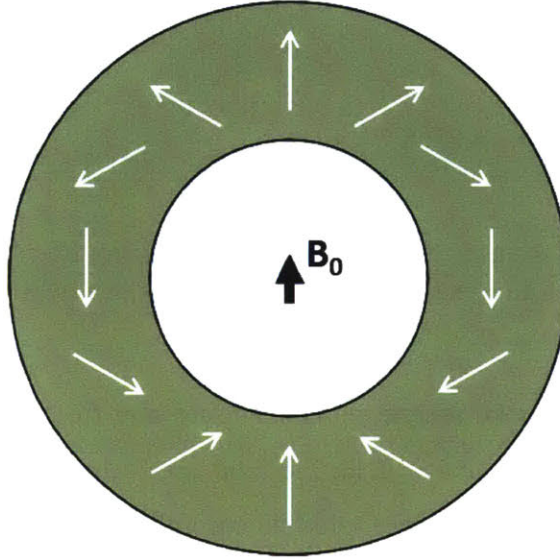


Figure 3-2: The direction of the magnetization in an ideal cylindrical Halbach array varies continuously.

As can be seen, the magnetic flux flows unidirectionally through the bore and is returned through each side of the magnet ring. The Halbach design differs from conventional NMR configurations in that the B_0 field is perpendicular to the bore rather than parallel to it. The strength of the field depends on the ratio of the inner and outer radii, and is given by [38],

$$B = B_r \ln \frac{r_{outer}}{r_{inner}}, \quad (3.2)$$

where B_r is the residual flux density. This formula assumes an infinitely long cylinder,

and the finite length in practice can cause distortions affecting field strength and homogeneity. These distortions can be partially alleviated by using two layers of magnets spaced an optimal distance apart [28].

A cylindrical magnet with continuously varying polarization such as in the Halbach is not practical to manufacture. Therefore, physical realizations approximate the ideal design using multiple discrete magnets. Trapezoidal magnets, shown in Fig. 3-3a, provide the most faithful approximation and largest field B_0 . Identical square or round magnets, show in Fig. 3-3b, are a more economical option, avoiding the need for custom magnets polarized in specific orientations.

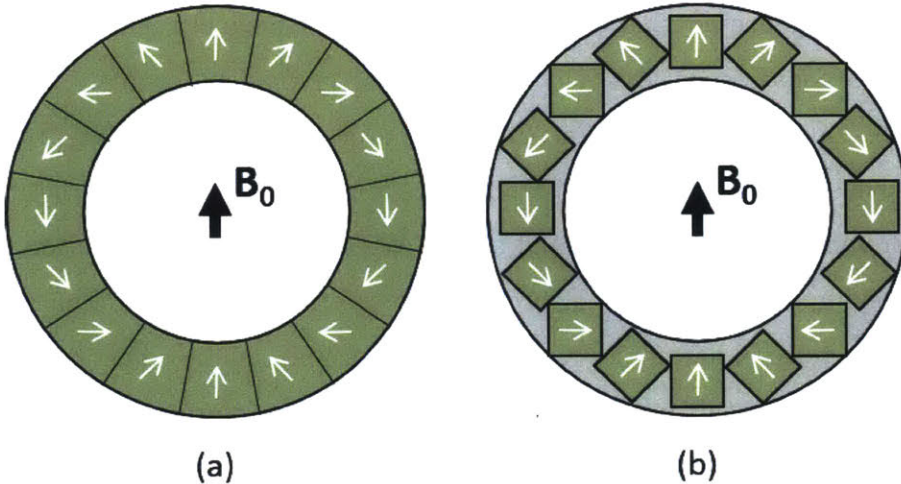


Figure 3-3: Physical realizations of the Halbach array use discrete magnets to approximate the ideal magnetization. In (a), trapezoidal magnets of various polarizations are used, while (b) shows a design using identical magnets. Figure adapted from [28].

Assembling the Halbach array is challenging, particularly for the last few pieces, which are strongly magnetically repelled. Rare earth magnets are brittle, and the large repelling and attracting forces can fracture or crush the magnets [11]. Techniques have been developed to ease assembly of Halbach geometries that use identical magnets [38, 39], but in every case specialized jigs and great care will be required. The challenges of assembling Halbach arrays significantly adds to their cost.

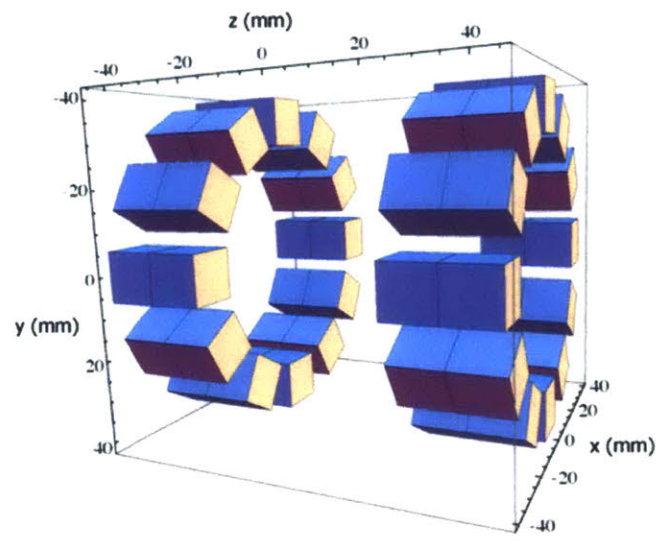
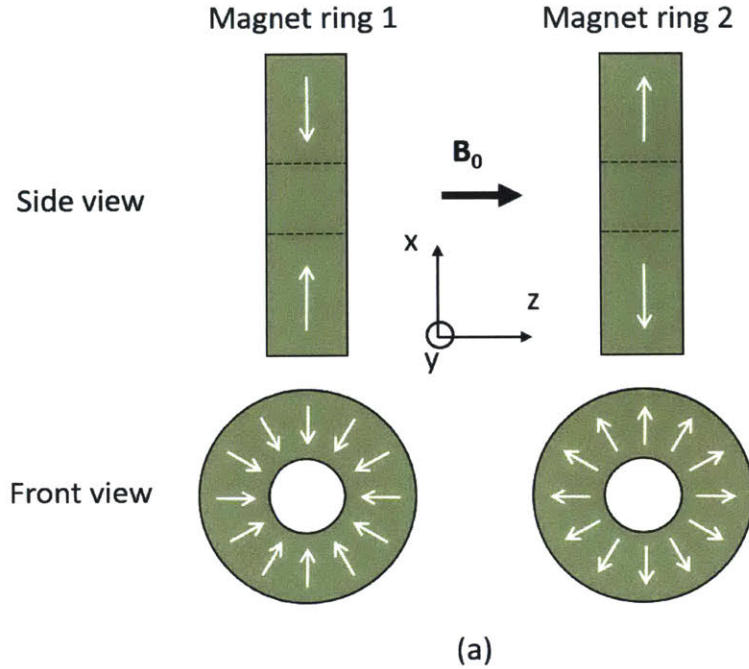
3.1.3 Aubert Configuration

The Aubert Configuration [30] is a simple, highly symmetric design to create a homogeneous magnetic field in the region of interest, where the sample will be located. The design consists of two rings of magnets placed an optimal distance apart, as shown in Fig. 3-4. In one ring, all the magnet pieces point radially inwards, while in the other ring, all the pieces point radially outwards. The magnetic flux pushed towards the center of the radially-inward ring is drawn towards the radially outward ring, creating a homogeneous field in the space between the rings. It is noteworthy that because the flux return path in this design is through air, the magnetic field generated is weak compared to designs using steel or magnets to close the magnetic circuit.

The principle behind this design is to model the magnetic field in terms of a spherical harmonic expansion, and then to place permanent magnets in a way to cancel terms of the expansion. The spherical harmonic expansion is an orthonormal basis set whose zero-order term represents the average field value B_0 , the first order terms represents linear gradients, and so on. With a magnet configuration of n -fold rotational symmetry, the first $n - 2$ orders of skew terms called tesseral harmonics are nulled. These tesseral harmonics represent variations in x and y when the field points along z . In addition, the antisymmetry of the two rings with respect to the xy plane cancels the even orders of the zonal harmonics, the ones varying with z . Finally, the spacing between the two rings is chosen to cancel the first odd zonal harmonic. The higher order terms are small and the variations they cause do not require correction. Thus, the symmetries and anti-symmetries of the magnet assembly are chosen to attain the desired field homogeneity.

3.1.4 Shim-a-Ring

The shim-a-ring assembly is the simplest of the designs considered. It consists of only two pieces: a single cylindrical magnet which is encased by a concentric, cylindrical steel shim (Fig. 3-5). The magnet is *diametrically* magnetized, meaning the magnetization is perpendicular to the bore. The steel shim provides the flux return



(b)

Figure 3-4: The many symmetries of the Aubert configuration create a highly homogeneous field. Flux is forced inwards in one ring, and outwards in the other, with the homogeneous field in the region in between (a). Identical discrete magnets are used to realize the design (b). Figure adapted from [40].

path. The result is a region of homogeneous field inside the magnet bore. As with the Halbach array, this magnetic field is orthogonal to the bore.

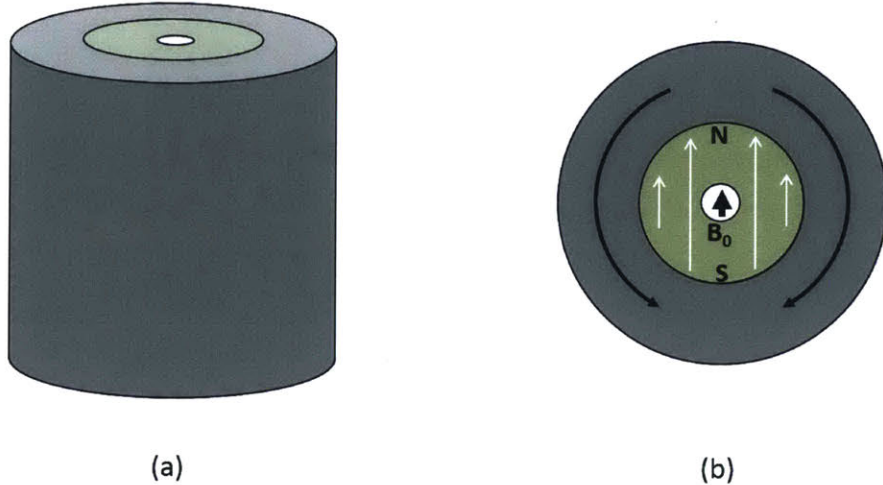


Figure 3-5: The shim-a-ring magnet consists of a cylindrical magnet inside a cylindrical steel shim (a). The magnet is diametrically polarized, and the shim provides the flux return path (b), creating a homogeneous field in the bore.

The shim-a-ring is remarkable for its ease of assembly. In sharp contrast to the Halbach array, the magnetic attraction of the pieces draws them into the desired configuration. Assembly is as simple as aligning the magnet and the steel and allowing them to pull together.

3.1.5 Design Comparison

The magnet of a portable NMR device presents an area for innovation and improvement. In miniature NMR, the more manageable size and cost is a worthwhile trade-off for the smaller magnetic field and reduced resolution. Sub-kilogram magnets for spectroscopy are complex and require significant manufacturing labor, which drives up the cost and lessens the attractiveness of a miniature instrument. Based on this insight, among small magnet designs with field strength and homogeneity sufficient for spectroscopy, the most easily manufactured magnet should be prioritized.

Comparisons were made between the four above designs in the areas of functional requirements: mass, field strength, field homogeneity, and manufacturability. Because

greater field strength can be achieved with larger magnet assemblies, the metric of field strength per assembly mass was used for comparison. Figures pertaining to size, mass, and magnetic field characteristics were pulled from the literature.

For some magnet configurations, information relevant to some functional requirements had not been published. Finite element simulations in COMSOL Multiphysics [41] were performed for each design to help fill in the gaps. Rather than optimizing the geometry, dimensions were copied from the designs in literature. The simulations yielded information about the strength and homogeneity of the magnetic field in the region of interest. The region of interest was chosen to be a 4 mm cube—large enough to accommodate a full-sized NMR sample tube. The homogeneity was computed by considering the magnetic field at 729 points on an evenly spaced grid in the region of interest, with each point separated by half a millimeter. The ppm homogeneity is then given using the following formula:

$$\frac{\sum_{i=1}^n \frac{|B_i - B_0|}{B_0} \times 10^6}{n}, \quad (3.3)$$

where B_i is the magnetic field at each sample point, B_0 is the magnetic field at the center of the homogeneous region, and n is the number of points considered.

The part per million (ppm) variation of the B_0 field in reality will be orders of magnitude larger than predicted by simulations. Sources of inhomogeneity include errors in aligning the magnets [39], variations in magnetic moment between the different pieces [32] and magnetization imperfections within the individual magnet pieces [8]. Several researchers have improved their results by screening the individual magnet pieces and selecting pieces with matched field strength [34, 30], though shimming afterwards is still needed. The homogeneity information extracted from simulations, therefore, represents a lower bound for the performance of physical magnets, and although not accounting for the above sources of error, it is still an indicator of relative performance between different magnet designs.

Table 3.1 shows results of the comparison. Due to the inexact estimates of the homogeneity simulations, the threshold requirement of 0.5 T for field strength, and

Table 3.1: Order-of-magnitude comparisons between the four designs, with Halbach as the standard for comparison, showed the shim-a-ring a standout for its manufacturability.

Functional Requirement	Iron Yoke	Halbach	Aubert	Shim-a-Ring
Field Strength per Mass	0	+	-	0
Field Homogeneity	0	0	+	0
Manufacturability	0	-	0	+

the fact that designs were copied from literature rather than optimized, only order-of-magnitude differences are noted. The most common NMR permanent magnet design, the Iron Yoke, was used as a baseline for comparison. Better performance in other designs is marked with a '+', worse performance with a '-', and equivalent with a '0'.

Based on the above comparison, it was chosen to pursue designs using the shim-a-ring magnet. This magnet configuration adequately met the functional requirements for field strength, mass, and predicted homogeneity, and its manufacturability promised to make it a low-cost option relative to other designs.

3.2 Shim-a-Ring Optimization

Simulations were performed in COMSOL to find the dimensions of the shim-a-ring magnet that would provide the best homogeneity; optimal configurations identified by the simulations were experimentally verified. For this, a Hall Effect sensor (HGT-2101; Lake Shore Cryotronics, OH) was used to assess the homogeneity of the magnetic field. Packaged in a 1.5 mm by 1.5 mm integrated circuit, the active area of the sensor was 0.127 mm by 0.127 mm, thus providing adequate spatial resolution to construct a field map. The sensor was mounted on a custom PCB, shown in Fig. 3-6 below. The PCB featured long arm with the sensor mounted 30 mm down to allow mapping inside the bore of a tall magnet.

The body of the PCB contained a simple operational amplifier circuit to supply constant current to the Hall sensor (Fig. 3-7). The output voltage of the sensor was proportional to both the supplied current and the local magnetic field. With a

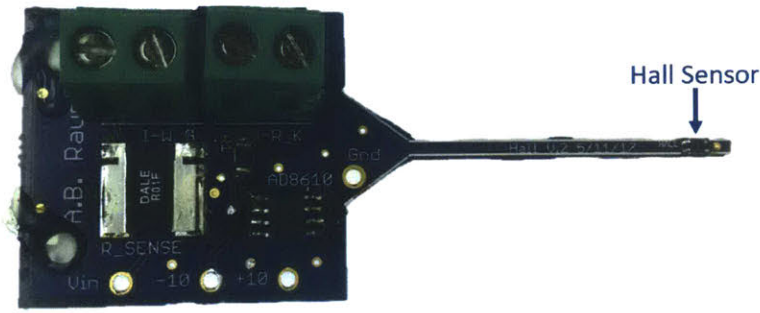


Figure 3-6: A small Hall effect sensor was mounted on a custom PCB to the end a of long arm to allow field mapping inside the magnet bore.

5 mA current supplied, the Hall sensor generated 192.5 mV per Tesla of field. Hall voltage was measured using a nanoVolt meter (34420A; Hewlett-Packard, CA). The Hall sensor was mounted on a 3-axis stage capable of 0.01 mm resolution, and the probe was displaced by hand within the magnet bore.

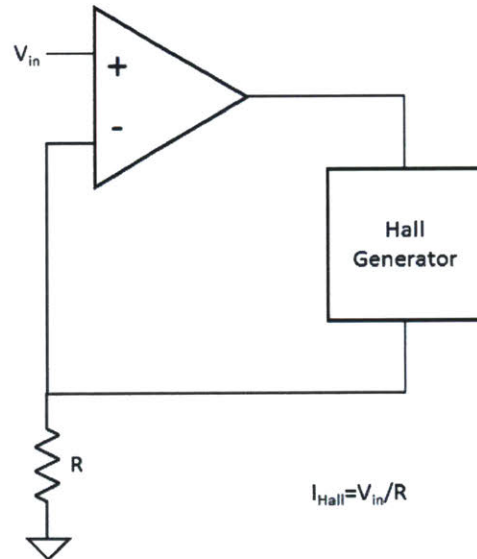


Figure 3-7: An op amp circuit supplied constant current to the Hall sensor, determined by the reference voltage V_{in} .

Two magnet geometries were modeled, constructed, and measured: first, using a commercially available magnet, and a custom shim, and next using a custom magnet and a commercially available shim. Both designs were predicted to give adequate

homogeneity for NMR measurements. Commercially-available magnets had a shorter lead time and were less expensive, though if a design were commercialized, the cost of custom magnets would decrease as production volume increased. Similarly, the decrease in machining time obtained by using a commercially available shim would decrease cost were a design to go to market.

3.2.1 Commercially Available Magnet

The commercially available magnet selected was 50.8 mm tall, with a diameter of 50.8 mm and a bore of 6.35 mm (RY04Y0DIA; K&J Magnetics, PA). The N42 grade neodymium iron boron magnet had a residual flux density of $B_r=1.32$ T. The shim was made from low-carbon steel (e.g. 1018), with the inner diameter of 50.8 mm set to match the magnet dimensions. The shim outer diameter of 101.6 mm was designed to be thick enough to return all the magnetic flux without saturating, thus maximizing the strength and homogeneity of the magnetic field. Simulations predicted a 0.72 T field and a homogeneity of 50 ppm in a 4 mm cube at the center of the bore.

Available tubing with a 101.8 mm outer diameter had insufficient wall thickness, and thus the shim was manufactured from a solid rod. To assemble the shim and magnet, a series of acrylic discs were bolted to the top of the magnet, as shown below in Fig. 3-8. The shim was slipped over the discs, which thus aligned the magnet and shim while maintaining a separation between the two pieces such that the attractive forces between them were moderate. With the shim fitted over the acrylic disks, it was released and energetically pulled into place around the magnet. Thus, the assembly was simple and rapid, as predicted, though care was still needed to manage the large magnetic forces.

The completed assembly (Fig. 3-9) had a mass of 3.16 kg.

The measured field strength in the bore was 0.60 T, 17% less than the predicted value. The field was measured with the Hall effect sensor along three orthogonal axes within the bore, where the origin was at the geometric center. These axis measurements, Fig. 3-10, showed that the ppm variation of the magnetic field was 2 orders of magnitude larger than the predicted 50 ppm in a 4 mm cube. As discussed

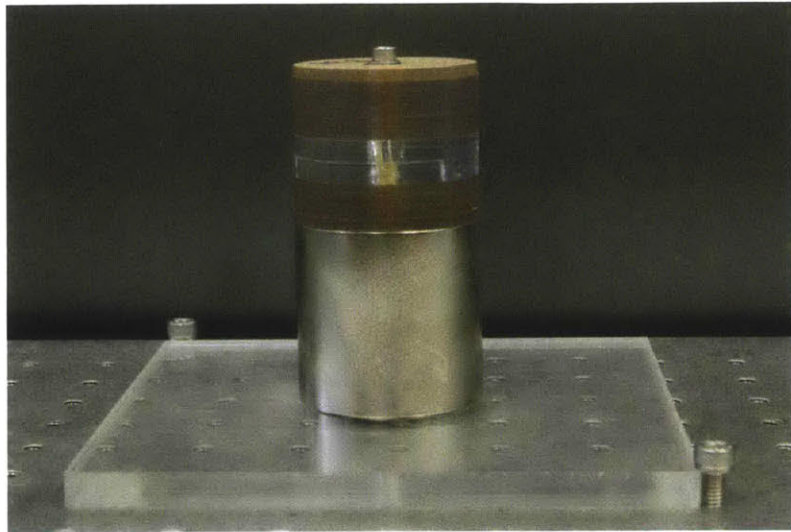


Figure 3-8: Acrylic disks were mounted to the cylindrical magnet to allow alignment of the shim without interference from strong magnetic forces.



Figure 3-9: The complete shim-a-ring was easily assembled.

in Section 3.1.5, NMR magnet assemblies routinely perform much worse in practice than in simulation. In this single-magnet design, the degradation can be attributed to the imperfections of the magnetization strength or direction within the magnet.

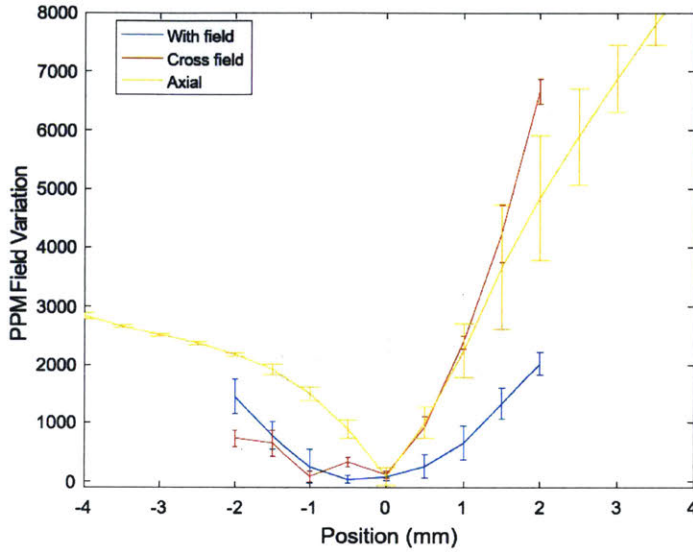


Figure 3-10: The ppm variation of the first shim-a-ring was orders of magnitude larger than predicted by simulations.

3.2.2 Custom Magnet

Better results were obtained using a shim made from commercially available stock. COMSOL simulations showed that a low carbon steel tube with 38.1 mm outer diameter and 19.05 mm inner diameter had sufficient wall thickness to return the magnetic flux of an inset magnet without saturating. Modifying this standardly-sized stock to serve as a magnet shim was trivial: the steel tubing was cut to length, and a flexible cylinder hone was used to smooth the inner surface.

The outer diameter of the custom magnet was set to match the inner diameter of the tubing stock, because simulations showed best results for zero gap between the pieces. The bore size and total length were varied in COMSOL simulations to optimize for field strength and homogeneity. The allowed dimensions were limited by manufacturing capabilities. Although these capabilities varied between manufactur-

ers, in general creating a ring magnet longer than 60 mm was not feasible. Similarly, a bore size of 10 mm or larger was preferred in order to accommodate the probe and allow enough space to add field-correcting shims.

Models were created assuming that the magnet material was N55 grade neodymium iron boron magnets, with a residual flux density of 1.48 T. As with the Halbach array, enlarging the size of the bore relative to the magnet outer diameter caused a decrease in magnetic field strength (Fig. 3-11). Therefore, it was decided not to exceed the nominal desired bore size of 10 mm. A 0.53 T field was predicted for a 10 mm bore—reduced from the previous design, yet still meeting the 0.5 T threshold recommended for spectroscopy.

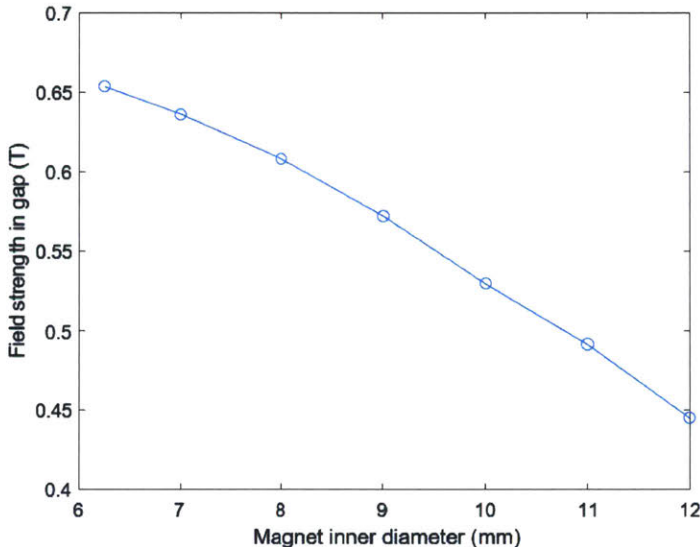


Figure 3-11: Simulations predicted a decrease of field strength in the bore as the bore size increased. Here the models used an axial length of 50.8 mm, a magnet outer diameter of 19.05 mm, and a shim outer diameter of 38.1 mm.

With the inner diameter set to 10 mm and the outer diameter set to 19.05 mm, the axial length in simulations was varied. The simulations showed homogeneity increasing rapidly as the axial length increased, and then leveling off or slowly increasing as the length increased beyond about 50 mm (Fig. 3-12). The minimum prediction variation was 10 ppm in the 4 mm cube.

Similarly, with the length set to 50.8 mm and the outer diameter to 19.05, the

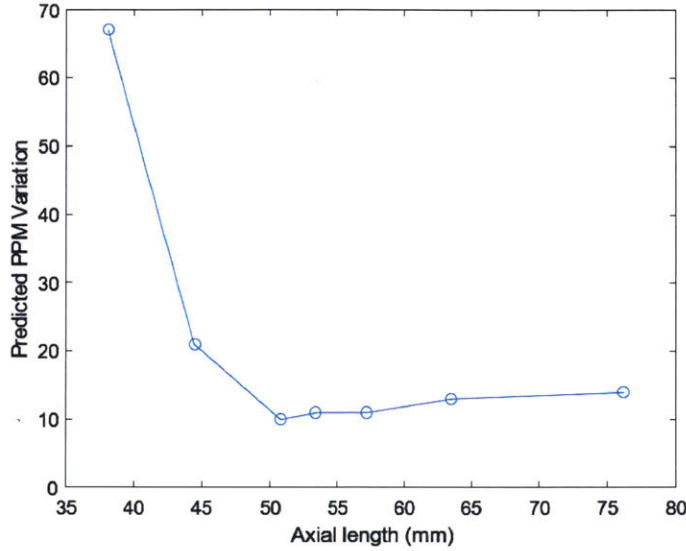


Figure 3-12: Homogeneity in the shim-a-ring increased as axial length increased, appearing to reach a minimum around 50 mm. Here the simulations used a magnet inner diameter of 10 mm, magnet outer diameter of 19.05 mm, and a shim outer diameter of 38.1 mm.

best homogeneity was found for an inner diameter of 10 mm (Fig.3-13).

Additional simulations were performed for larger and smaller inner diameters, and longer and shorter axial lengths. In each case, an optimal geometry existed with a field homogeneity of 10 ppm. Based on these results, custom magnets were made (SM Magnetics, AL) according to the specifications summarized below in Table 3.2.

Table 3.2: Custom shim-a-ring magnets were manufactured according to the below specifications.

Parameter	Value
Magnet Grade	N55 NdFeB
Magnet Inner Diameter	10 mm
Magnet Outer Diameter	19.05 mm
Shim Inner Diameter	19.05 mm
Shim Outer Diameter	38.1 mm

This smaller shim-a-ring, shown below in Figure 3-14, had a mass of 418 g after assembly.

Figure 3-15 below shows the variation of the magnetic field measured by the Hall

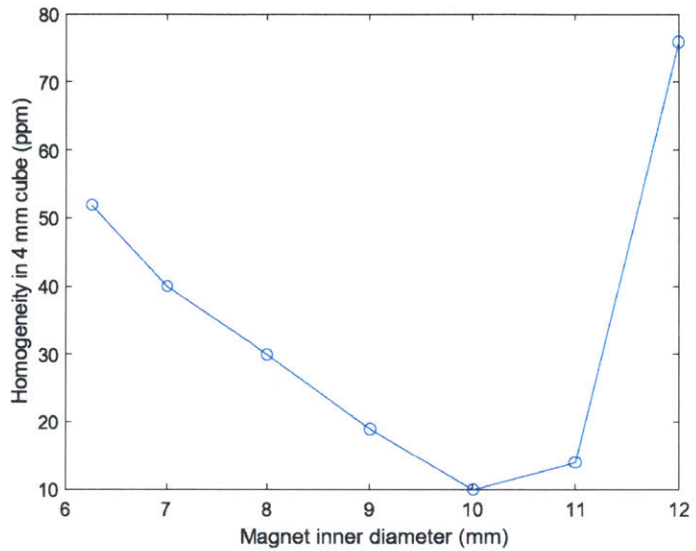


Figure 3-13: For a 50 mm length, simulations showed maximum homogeneity with a 10 mm bore. Here the models used an axial length of 50.8 mm, a magnet outer diameter of 19.05 mm, and a shim outer diameter of 38.1 mm.



Figure 3-14: The shim-a-ring made with a custom magnet was significantly narrower.

Sensor along three axes. The field homogeneity, while still orders of magnitude larger than the predicted value, was a significant improvement over the previous iteration. The magnitude of the field, at 0.48 T, was 10% smaller than the predicted value. This decline relative to the expected performance, as discussed in Section 3.1.5, is expected, given the imperfections of the magnetic material and the magnetizing process.

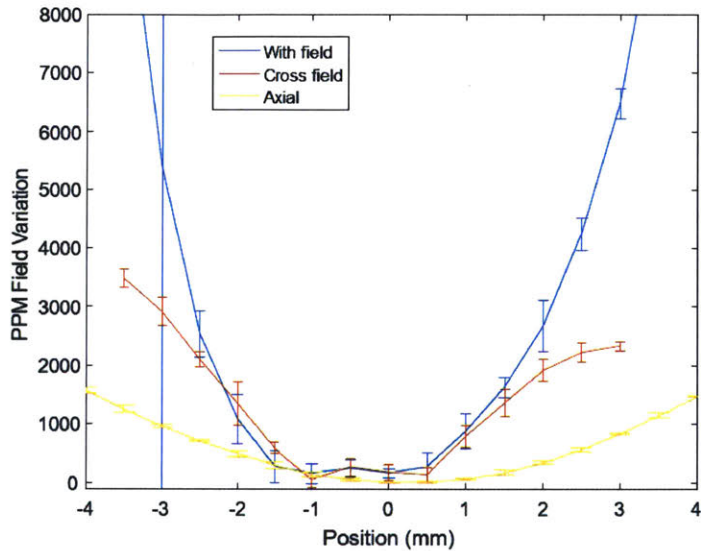
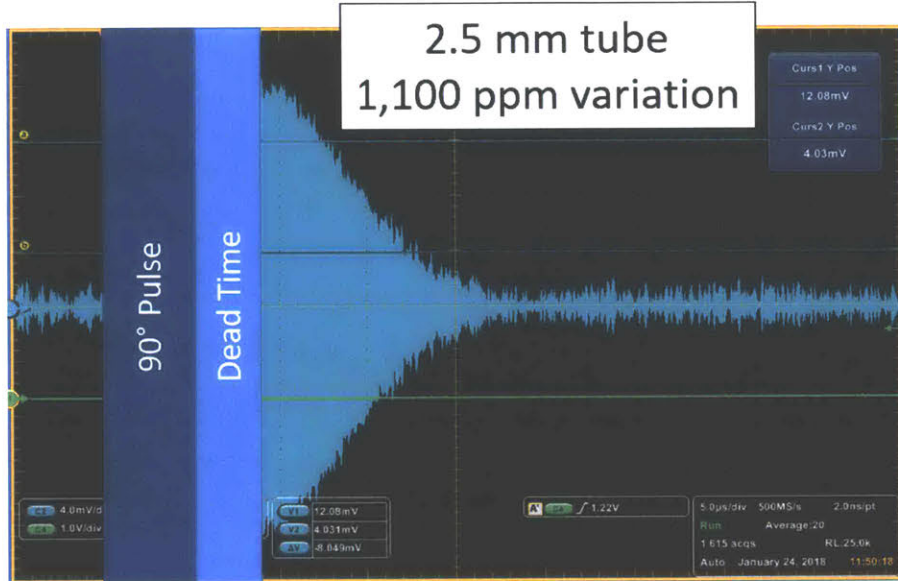


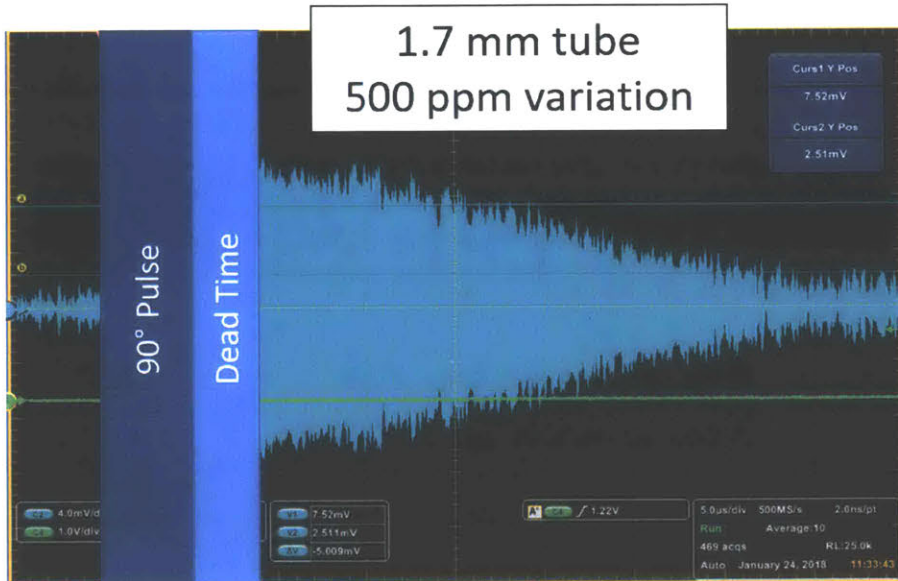
Figure 3-15: Measured homogeneity in the smaller shim-a-ring was an improvement over the previous iteration.

The homogeneity of the field in the smaller shim-a-ring was sufficient to allow measurement of the NMR signal. Figure 3-16 shows NMR signals measured using a 2.5 mm OD sample tube and a 1.7 mm OD sample tube of 5 mM manganese chloride. These signals were measured on an oscilloscope immediately after the preamp, without mixing down the frequency. Using Eq. 1.6, the field variation is computed to be 1100 ppm in the 2.5 mm sample and 500 ppm in the 1.7 mm sample. As expected, the smaller sample has less signal amplitude, but better homogeneity, because it spatially samples a smaller volume of the field.

The smaller shim-a-ring magnet with a 1.7 mm OD sample tube provided adequate signal strength and duration for meaningful measurements, and was used to explore stochastic NMR capabilities as detailed in Chapter 4. Spectroscopy, however, requires



(a)



(b)

Figure 3-16: The FID measured in the smaller shim-a-ring has a larger amplitude with a larger sample tube (a), but longer duration in a smaller tube (b), indicative of smaller ppm variation.

sub-ppm homogeneity and was out of reach. The following section explores a cost-effective strategy for shimming the field of this magnet in order to allow spectroscopic measurements.

3.3 Active Shim System

Historically, spectrometer magnets have been shimmed using ferromagnetic material or electromagnets, with each shim designed to modify one spherical harmonic of the magnetic field [42]. In compact NMR magnets, small permanent magnets have become the method of choice to correct the field [8, 34, 30, 43]. The permanent magnets need to be positioned once during the calibrations stage, then remain in place. They are a type of *passive* shim, correcting large field inhomogeneities without consuming power. Permanent magnet shims are limited by the mechanical precision with which they can be moved, with even micron-level displacements causing a large modification of the field. Therefore, fine corrections are achieved using *active* shims.

Unlike passive shims, active shims continuously consume power. They are electromagnets, whose correction of the field scales with the strength and direction of the current supplied. To limit power consumption and heat generated, active shims are employed to make small field corrections, with the gross corrections performed by passive shims.

The results obtained using this dual approach are impressive. In their 2010 paper, Danieli *et al.* obtain sub-ppm spectra using a half kilogram magnet assembly [8]. Their magnet is a Halbach array, with three stacked rings of trapezoidal magnets. Interspersed with the trapezoidal magnets are rectangular magnets, which can be displaced radially to correct the magnetic field, as shown in Fig. 3-17.

Calibrating the passive shims is laborious and iterative. First, a map is made of the magnetic field, either using MRI to take a picture, or point by point with a small Hall sensor or NMR probe. Next, the measured field is decomposed into spherical harmonic components. The required shim magnet displacements to null these components are computed, then effected. Finally, the magnetic field is mapped

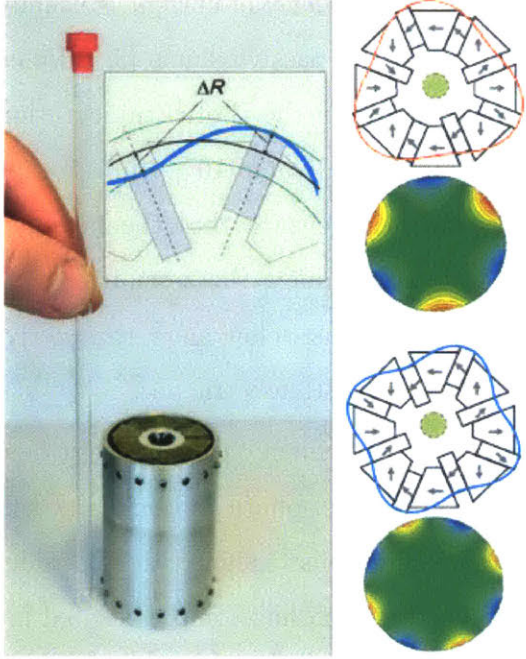


Figure 3-17: The magnet field can be shimmed using moveable magnets embedded in the array, as performed by Danieli *et al.*. Figure adapted from [8].

again, and the process is repeated until the desired homogeneity is obtained.

Although effective, correcting the magnetic field using dozens of moveable shim magnets is not a scalable, low-cost option. In the remainder of this section, the feasibility of using active shims only is examined.

An active shim system would provide numerous benefits. Rather than using moveable magnets whose positioning corrects a specific magnetic field, identical shim coils would be installed in every unit. Instead of arduous micron-level mechanical displacements, the level of field correction would be easily controlled by the current polarity and amplitude. Finally, mapping the field would not be necessary. Instead, an optimization routine could find the ideal current for each shim by measuring the NMR signal and searching for the longest duration in the time domain, or the narrowest peak in the frequency domain [44].

The limitation, of course, is the power required for the active shims to correct large inhomogeneities. In continuous operation, the current density in copper is often

limited to about 10^7 A/m² [45]. This level of current is usually insufficient to correct the field, thus compelling the use of passive shims [8]. Higher current densities are possible, however, for brief periods. In the BioInstrumentation Lab, we have pushed the current density in linear motors as high as 10^8 A/m² for rapid, needle-free injection [46]. The primary limitation is to ensure that the heat generated due to ohmic resistance in the copper does not damage the assembly. In the case of the smaller shim-a-ring magnet, the computations below show that active shims could be used for short experiments to measure NMR spectra.

Section 3.3.1 discusses the measurement of the magnetic field of the smaller shim-a-ring magnet, and the calculation of the spherical harmonic coefficients of the measured field. Section 3.3.2 presents shim coils designed to fit inside the shim-a-ring bore, with one shim designed to correct each harmonic presented in Section 3.3.1. Finally, Section 3.3.3 compares the efficiency of the designed shim coils to the magnitude of correction required in order to estimate the current required to actively correct the field.

3.3.1 Measurement of Spherical Harmonics

To assess the level of shimming required, the magnetic field of the smaller shim-a-ring was measured in terms of an orthogonal basis set, the spherical harmonic expansion. The spherical harmonic coefficients were measured using the technique presented by Mackenzie *et al.* [47], which is a realization of the more general approach given by Romeo and Hoult [48]. The measurements and analysis are detailed below, using the spherical polar coordinate system shown in Fig. 3-18. As usual, the z -axis is set to align with the magnetic field.

Each spherical harmonic of order n has m degrees, where m ranges from $-n$ to n . Harmonics of degree zero are called zonal harmonics, and harmonics of degree other than zero are called tesseral harmonics. The key to measuring the harmonics is isolating the zonal and tesseral harmonics. The zonal harmonics are nonzero along the z -axis, but invariant with ϕ , and are given by,

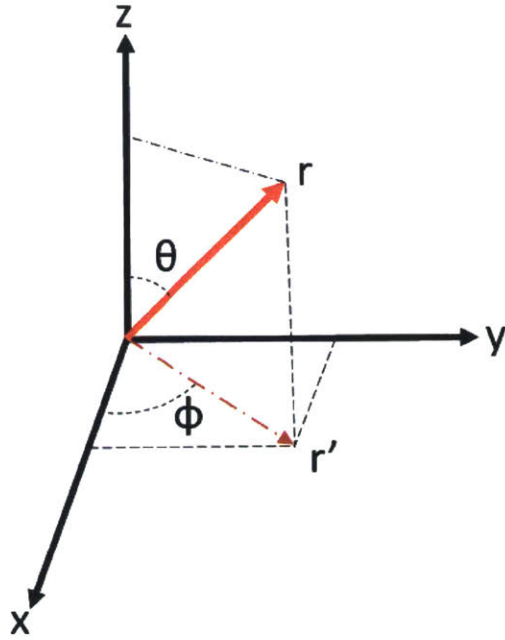


Figure 3-18: Field measurements were performed using the coordinate system shown.

$$T_n = br^n P_n(\cos \theta); m = 0, \quad (3.4)$$

where b is the harmonic coefficient and P_n is the Legendre function of order n . The tesseral harmonics are null along the z -axis and vary sinusoidally with ϕ , and are given by,

$$T_{nm} = br^n P_{nm}(\cos \theta) \left(\frac{\sin}{\cos} m\phi \right), \quad (3.5)$$

where b is again the harmonic coefficient and P_{nm} is the associated Legendre function of order n and degree m . Thus measurements taken along the z -axis give information about the zonal harmonics without interference from the tesseral harmonics. Similarly, measurements taken at constant θ and varying ϕ —that is, measurements that form a circle around the z -axis—give information about the degree m of tesseral harmonics present. To determine the order n of the tesseral harmonics, a common strategy is to measure several rings of points with equivalent radii r' at various heights

z , essentially taking measurements on the surface of a cylinder.

The field mapping procedure proposed by Mackenzie measures the magnetic field at 7 points along the z -axis, and three rings of eight points each at different z . The field measurements allow calculation of the first, second, and some third order tesseral harmonics, and the first through fourth order zonal harmonics. The points mapped are shown in Fig. 3-19.

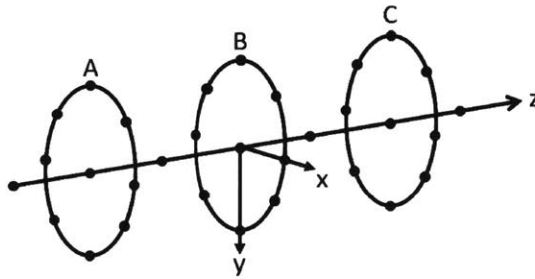


Figure 3-19: The field was mapped at 31 data points on the surface of a cylinder and along the z -axis.

In the smaller shim-a-ring magnet, the magnetic field was perpendicular to the bore. It was chosen to maintain the z -axis aligned with the magnetic field, and the coordinate system used is depicted in Fig. 3-20. The origin was set at the geometric center of the magnet. The HG-2101 Hall Effect sensor with custom PCB, introduced in Section 3.2, was used to map the field. Measurements along the z -axis were spaced every 1 mm from $z=-3$ mm to $z=3$ mm. The three circles had a radius of 2 mm and were located at $z=-2$, $z=0$, and $z=2$ mm.

A discrete Fourier transform of the eight points around each circle yielded the first and second degree harmonic components: $a_i \cos \phi$, $b_i \sin \phi$, $c_i \cos 2\phi$, and $d_i \sin 2\phi$, where i is the index denoting the coefficients derived from circles 1, 2 and 3. The coefficient for each degree contained contributions from every order which had a harmonic of each degree. For example, the first degree $\cos \phi$ term contained contributions from the first, second, third and higher orders. The second degree $\cos 2\phi$ term contained contributions from the second, third and higher orders, but not from the first order, because the first order harmonic has no second degree.

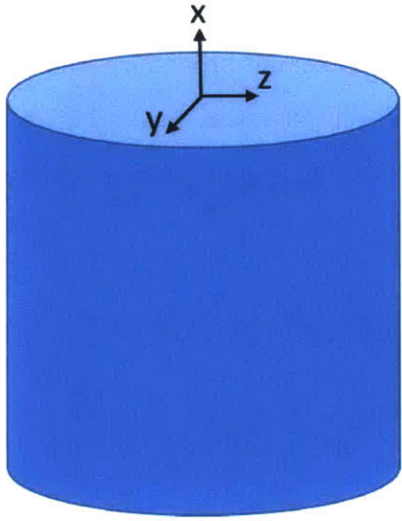


Figure 3-20: The coordinate system was set to maintain the z -axis in the field direction, perpendicular to the bore.

In cylindrical coordinates, the first degree $\cos \phi$ component of the field is given by,

$$B(z, \rho) = [S(X)\rho + 3S(ZX)z\rho + S(Z^2X)[6z^2\rho - \frac{3}{2}\rho^3] + \dots] \cos \phi, \quad (3.6)$$

where $S(X)$ is the amplitude of the X shim, $S(ZX)$ the amplitude of the ZX shim, and $S(Z^2X)$ the amplitude of the Z^2X shim. The field variations created by these shims in Cartesian coordinates are available in Table 3.3 below. In Eq. 3.6, the first term is the field contribution from the first order, the second term from the second order, and so on. To extract the contributions of each order, measured data was fit to the polynomial. Because there were three measured values for a_i , it was possible to include coefficients from the first three orders in the polynomial fit, where the coefficients of the polynomial were exactly determined. In the same way, the $S(Y)$, $S(ZY)$ and $S(Z2Y)$ amplitudes were computed from the $\sin \phi$ contributions to the field and the three values of b_i .

The $\cos 2\phi$ component of the field in cylindrical coordinates is given by,

$$B(z, \rho) = [3S(X^2 - Y^2)\rho^2 + 15S(Z(X^2 - Y^2))z\rho^2 + \dots] \cos 2\phi. \quad (3.7)$$

A least squares fit was used to determine the second- and third-order coefficients using the three values of c_i . The same procedure was used to compute the $S(2XY)$ and $S(Z(2XY))$ amplitudes using the three values of d_i .

For the zonal harmonics, the field generated by the zeroth through first orders is,

$$B(z, \rho) = S(Z^0) + S(Z^1)z + S(Z^2)[z^2 - \frac{1}{2}\rho^2] + S(Z^3)[z^3 - \frac{3}{2}\rho^2z] + S(Z^4)[z^4 - 3z^2\rho^2 + \frac{3}{8}\rho^4]. \quad (3.8)$$

The shim coefficients were again computed with a least squares fit, this time using all 31 data points.

The measured coefficients are shown in Table 3.3. The largest coefficients are for the zonal harmonics, corresponding to significant variations in the direction of the field.

Table 3.3: The results of the field mapping are shown via the measured harmonics coefficients, with the harmonic equations in Cartesian coordinates given for reference.

Harmonic	Name	Equation	Measured Coefficient
$T_{0,0}$	Z^0	(Constant)	0.4785
$T_{1,-1}$	Y	y	8.828×10^{-5}
$T_{1,0}$	Z	z	-8.006×10^{-4}
$T_{1,1}$	X	x	2.451×10^{-4}
$T_{2,-2}$	$2XY$	$3(2xy)$	6.024×10^{-6}
$T_{2,-1}$	ZY	$3zy$	-1.809×10^{-5}
$T_{2,0}$	Z^2	$z^2 - \frac{1}{2}(x^2 + y^2)$	-2.553×10^{-4}
$T_{2,1}$	ZX	$3zx$	-6.184×10^{-6}
$T_{2,2}$	$X^2 - Y^2$	$3(x^2 - y^2)$	8.171×10^{-5}
$T_{3,-2}$	$Z(2XY)$	$15z \cdot (2xy)$	1.694×10^{-7}
$T_{3,-1}$	Z^2Y	$\frac{3}{2}y \cdot [4z^2 - (x^2 + y^2)]$	2.345×10^{-6}
$T_{3,0}$	Z^3	$z^3 - \frac{3}{2}(x^2 + y^2) \cdot z$	6.027×10^{-5}
$T_{3,1}$	Z^2X	$\frac{3}{2}x \cdot [4z^2 - (x^2 + y^2)]$	4.872×10^{-6}
$T_{3,2}$	$Z(X^2 - Y^2)$	$15z \cdot (x^2 - y^2)$	4.292×10^{-6}
$T_{4,0}$	Z^4	$z^4 - 3z^2(x^2 + y^2) + \frac{3}{8}(x^2 + y^2)^2$	-1.705×10^{-5}

Shim designs to correct each of these measured harmonics are presented in the following section, and in Section 3.3.3 the current required to shim the magnetic field measured in this section is estimated.

3.3.2 Shim Design

Design Approach

Shims were designed using the technique described by Liu *et al.* [45], which was developed for correcting the field of Halbach arrays. As with most shim designs, each separate shim coil corrected a single spherical harmonic, and the shim was designed to lie along the inner surface of the magnet bore. Liu used a modified target field approach, where the current distribution across the surface of a cylinder is calculated such that it generates a desired magnetic field shape. By using a continuously distributed current, the target field approach is able to match the desired field shape over a larger region than is possible with traditional methods [49], which employ a superposition of discrete arcs and loops of current [48].

In superconducting magnets, the field is parallel to the bore, which by convention is denoted as the z -axis. In the Halbach array and the shim-a-ring, the magnetic field is perpendicular to the bore, and established shim designs must be modified. For this reason, Liu used an optimization routine to calculate the currents on the surface of the cylinder. Analytical solutions are available for shimming the Halbach geometry [50, 51], but the optimization speed and accuracy were sufficient for the purposes of this work.

The current on the cylinder surface was not computed directly; instead, the scalar stream function was used. Use of the stream function allows optimization of surface currents, given constraints in the desired electromagnetic properties [52, 53]. Surface current can be computed from the stream function, as shown:

$$\vec{J}_s(\vec{r}) = \nabla \times S(\vec{r})\hat{n}(\vec{r}), \quad (3.9)$$

where \vec{r} is the position vector, \vec{J}_s is the surface current density, S is the stream function, and \hat{n} is the outward unit normal. The stream function was fixed to the coil surface, meaning that \hat{n} pointed radially outwards. It is important to note that the above equation fulfills the requirement that the surface current density be divergence free, and that no current flows into or out of the surface along the \hat{n} direction.

When interpreting the stream function, it is helpful to note that \vec{J}_s is the largest where S changes the most rapidly, due to the ∇ in Eq. 3.9. Due to the cross product in Eq. 3.9, \vec{J}_s will point in the direction perpendicular to the direction of most rapid change in S , meaning that \vec{J}_s flows along isolines of S . These properties are important for translating optimization results into a physically realizable coil.

Simulation Details

It was desired that, after shimming, the homogeneous region be able to accommodate a full-sized NMR sample tube. Therefore, the shims were designed to match the desired harmonics over the volume of a 4 mm diameter sphere, equal to the inner diameter of a standard sample. One hundred target points were chosen within this 4 mm diameter sphere, and the desired magnetic field at each point was specified. For example, when designing the first order z -gradient, the magnetic field at each target point was chosen to vary linearly with z .

In the optimization, the magnetic field generated by the coil was constrained to match the desired value at the target points, with 5% tolerance. The field values were computed from the stream function values on the surface of the coil. For this work, the stream function was computed at 4,500 discrete points, and approximated to be constant in the small area surrounding each point. The magnetic field at the target points was computed by summing the effects of the 4,500 discrete S -points.

The stream function was computed on the surface of the shim coil, which was designed to fit inside the magnet bore. Thus, the maximum shim diameter was 10 mm, equal to the bore diameter. Each successive shim would be nested inside the previous, with a slightly smaller diameter each time. To account for this effect, shims for each harmonic were computed at two diameters: 10 mm, representing the largest diameter possible, and 6 mm, representing an inner nested shim. In both cases, the shim was set to 50 mm high, again matching the magnet dimensions. Each point at which the stream function was modeled in the 10 mm case is shown in Fig. 3-21.

In the optimization, the objective function minimized was the power dissipation. Power dissipation is a logical parameter to optimize for this application, because the overall strategy is to boost the current in the shims while carefully managing

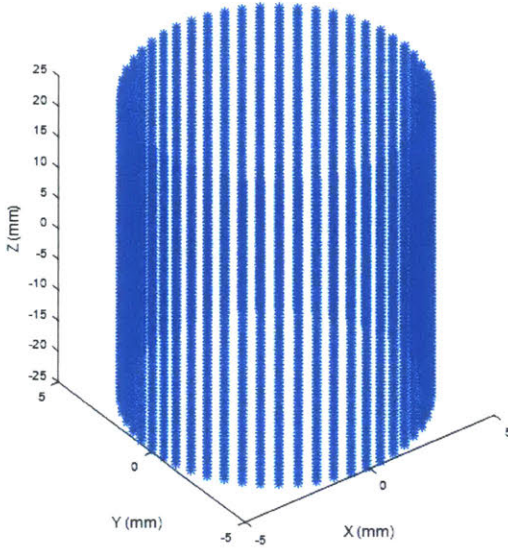


Figure 3-21: The stream function was calculated at 4500 discrete points forming the surface of a cylinder.

dissipated heat. As derived by Liu, the power dissipation of each element is given by,

$$\Delta P = \frac{\rho}{h} [(S_{q+1} - S_q)^2 + (S_{q+Q_c} - S_q)^2], \quad (3.10)$$

where q is the index of the discretized stream function, Q_c is the number of columns formed by the grid of points in Fig. 3-21, ρ is the electrical resistivity of copper, and h is the copper thickness. In the equation above, the first squared term is the difference between horizontal neighboring stream function points, and the second squared term the difference between vertical neighbors. The objective function to minimize is given by removing the scaling constants and summing the contribution of every element:

$$P \sim \sum [(S_{q+1} - S_q)^2 + (S_{1+Q_c} - S_q)^2]. \quad (3.11)$$

Because the objective function was quadratic, it was possible to efficiently perform the optimization using the quadratic programming function *quadprog* in MATLAB's Optimization Toolbox [18]. The optimization script was used to find stream function values that gave the desired magnetic field while minimizing power consumption and can be found in Appendix A.2. A summary of the key design choices for the

optimization are given in Table 3.4 below.

Table 3.4: Simulations to optimize the shims designs were performed according to the below specifications.

Parameter	Value
Region of Interest	4 mm sphere
Shim Dimensions	6 & 10 mm diameter 50 mm height
Discrete S points	4,500
Target Field Points	100
Allowed Field Deviation	5%
Objective Function	Power Dissipation

When adapting standard techniques for application in a Halbach array, with its field transverse to the bore, Liu followed convention by setting z along the bore, and chose to designate the field direction as x . The field at the target points varied just as for a superconducting magnet, with the difference that the target field pointed in the x -direction. In the general case, it is possible to use shim coils designed for B_z to shim a magnetic field pointing any direction, but two to three coils are required to shim each channel [50]. In order to be able to directly translate standard techniques for shimming superconducting magnets, it was chosen in this work to instead use a change of variables. The same coordinate system was used as in Section 3.3.1 (see Fig. 3-20), with the z -axis designated as the field direction, transverse to the bore.

Shims were designed to correct each of the harmonics fitted in the previous section. Results of the optimization are shown in Figs. 3-22 through 3-24. Fig. 3-22 shows contour maps of the stream function for the first order harmonics for both the 6 mm and 10 mm diameters. The features are similar in the two cases, with the maps in the 6 mm case vertically compressed compared to the 10 mm case. Figure 3-23 shows the contour maps of the second order for the 10 mm case only, and Figure 3-24 the contour maps of the computed third and fourth harmonics, again for the 10 mm case only.

In the contour maps of the stream function, there frequently appears to be an underlying symmetry with some distortions imposed. The evident symmetry shows

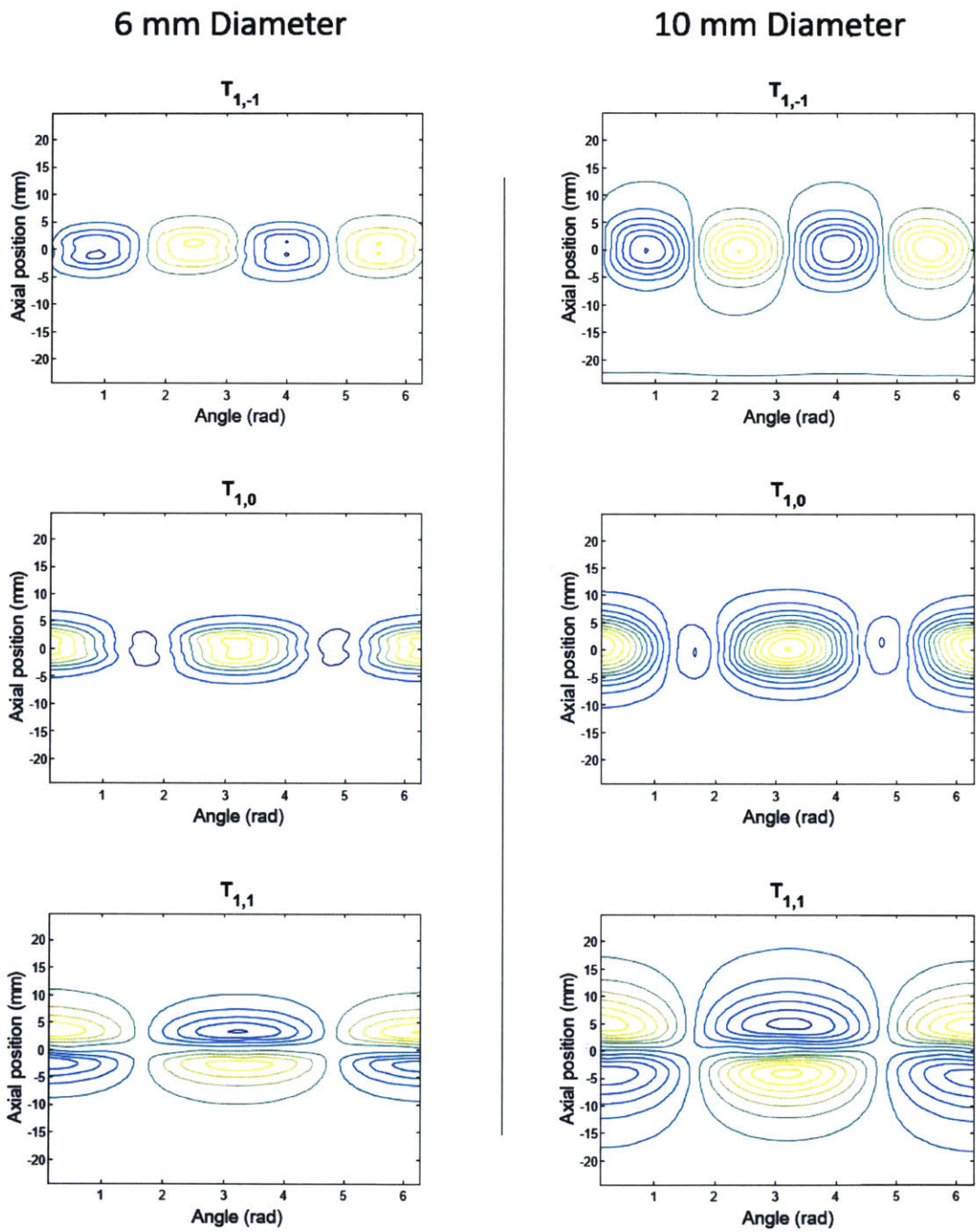


Figure 3-22: Contour maps of the stream function for the first order shims give the path that current should follow. Shown are designs made to wrap inside a 6 mm and 10 mm diameter cylinder.

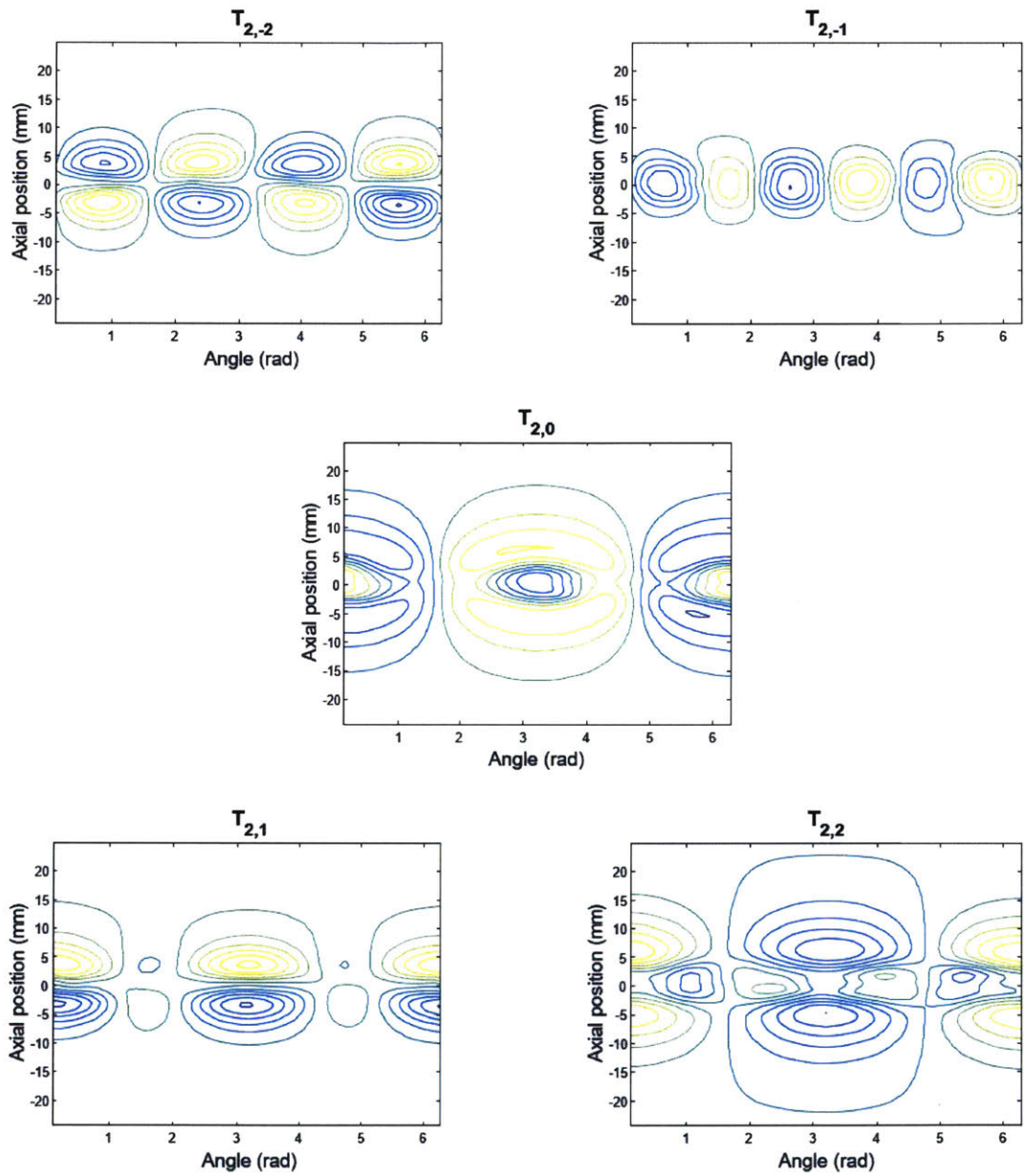


Figure 3-23: Contour maps of the stream function for the second order shims, with designs to fit in the 10 mm diameter cylinder shown.

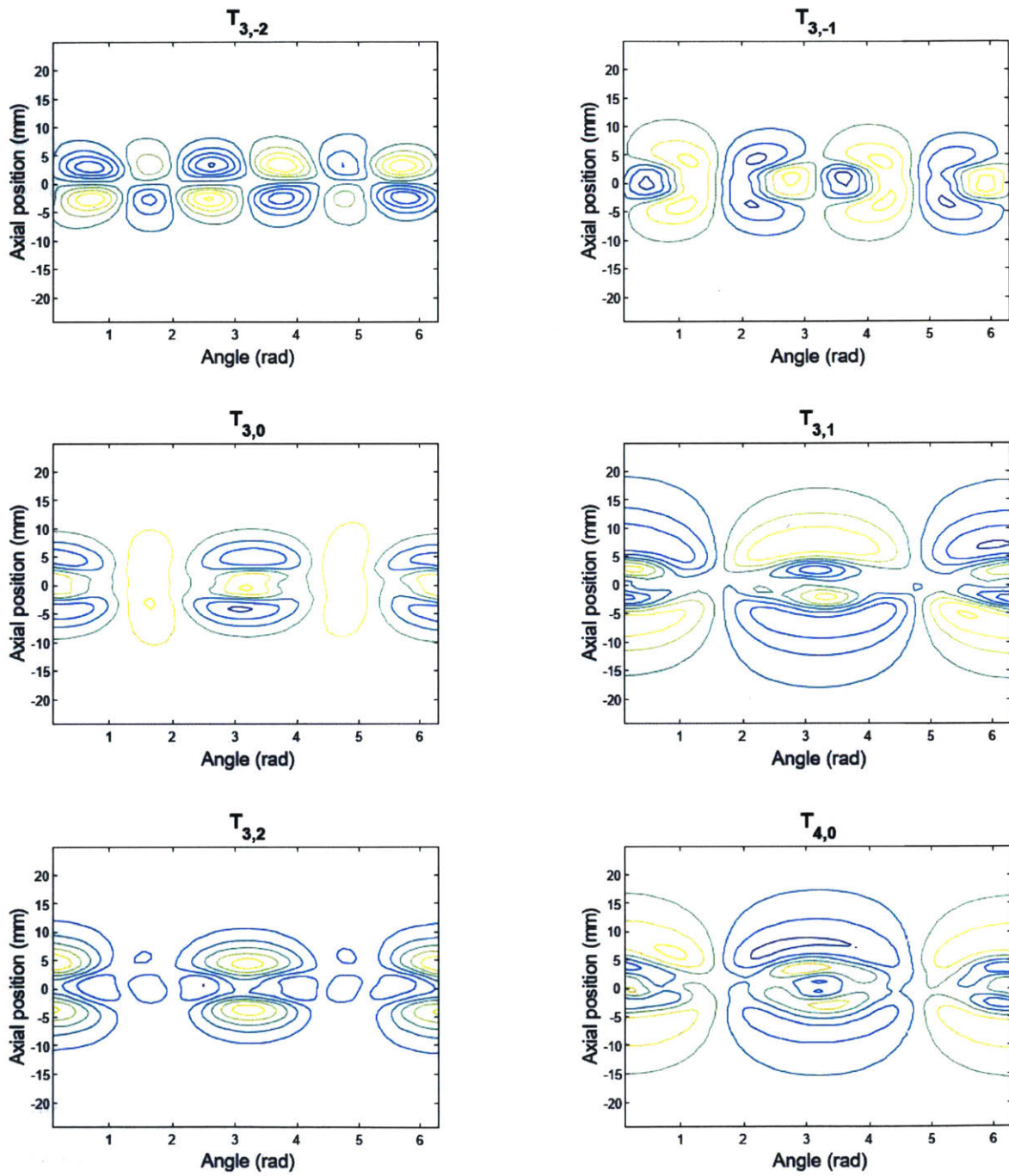


Figure 3-24: Contour maps of the stream function for the higher order shims, with designs to fit in the 10 mm diameter cylinder shown.

the shapes needed to generate the harmonics, and the distortions are an artifact of the optimization. The magnetic field in the optimization is constrained to match 100 target points randomly distributed in the region of interest. For each different distribution of target points, the distortions change to find the optimum for those points, but the underlying symmetry remains unchanged. The accuracy of the contour maps was sufficient for the purposes of this analysis, as the harmonic coefficients used in later calculations varied by less than 5% between point distributions. These distortions should be removed, however, before manufacturing the designs.

To physically realize the shim designs, a flexible circuit presents an ideal medium. In a flexible circuit, wiring is printed onto a flexible base material, and the circuit is able to bend. As shown in Fig. 3-25a, a two-layer board has a layer of copper on each side of a flexible plastic substrate, with an insulating cover layer added on the exposed faces. A feature called a via (Fig. 3-25b) can be used to provide an electrical connection between the two copper layers.



Figure 3-25: The copper layers of a flexible circuit are separated by a compliant substrate, and an adhesive attaches a cover layer to the outward-facing faces (a). Connections can be made between the copper layers using a copper-plated through hole called a via (b). Figure adapted from [54].

As previously stated, the current flows parallel to the stream function contour lines. The contour map can be etched onto the copper of a flexible PCB, with current flowing in the tracks between the contour lines. Current cannot, however, flow in infinite loops, and therefore modifications are required for physically realizable shims. As shown in Fig. 3-26, connections can be added between each of the tracks, allowing the current to spiral inwards. At the center of a spiral, a via funnels the

current to the back side of the flexible PCB. The same contour map is etched on the reverse side, and the current spirals back outwards. Channels connecting the various features allow the current to wind through all the features of the contour map on both the front and back faces, with the two layers reinforcing each other and doubling the strength of the generated magnetic field. This fabrication strategy has been successfully demonstrated and tested in [55].

After printing, the circuit is rolled and inserted into the magnet bore, as shown in Fig. 3-27. Each successive shim would nest inside the previous (Fig. 3-28). Manufacturing guidelines recommend that the flexible circuit bend radius be at least ten times larger than the board thickness, for a two-layer board [56]. The two-layer board would be about $200 \mu\text{m}$ thick [57]. Therefore, the bend radius should be at least 2 mm, and the 3 mm to 5 mm bore radii considered in simulation meet the guidelines. The fourteen shims together would reduce the bore radius from 5 mm to 2.2 mm.

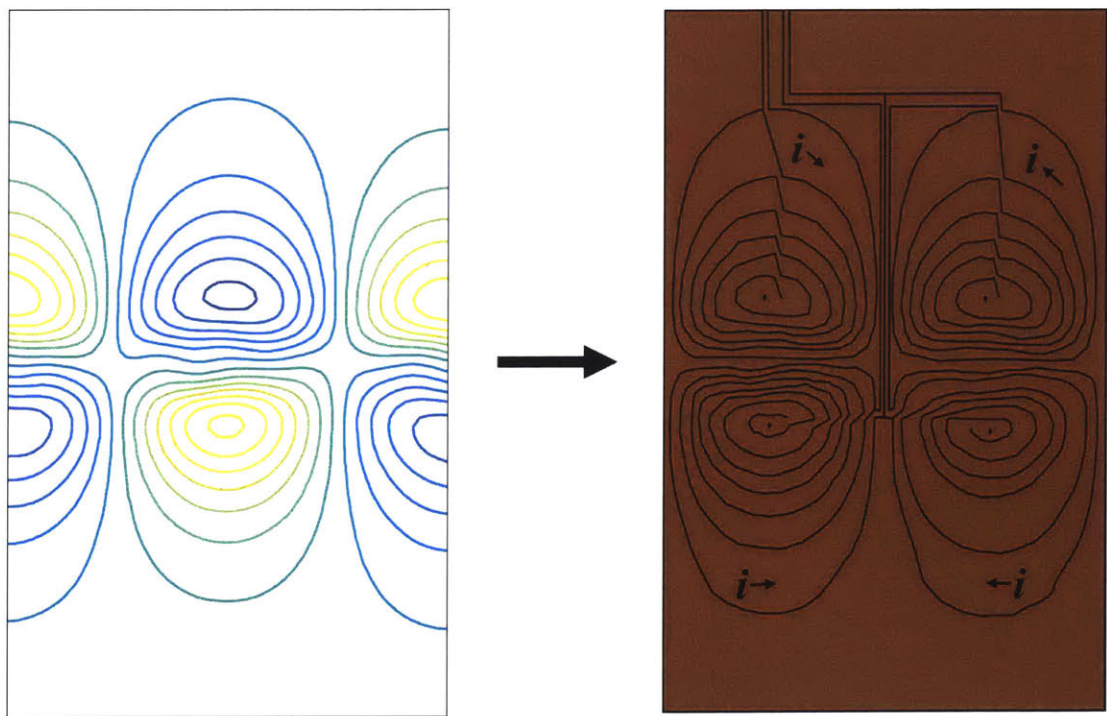


Figure 3-26: To turn the contour maps into shims, connections are added to connect the tracks and vias connect the front and back layers, allowing the current to flow continuously.

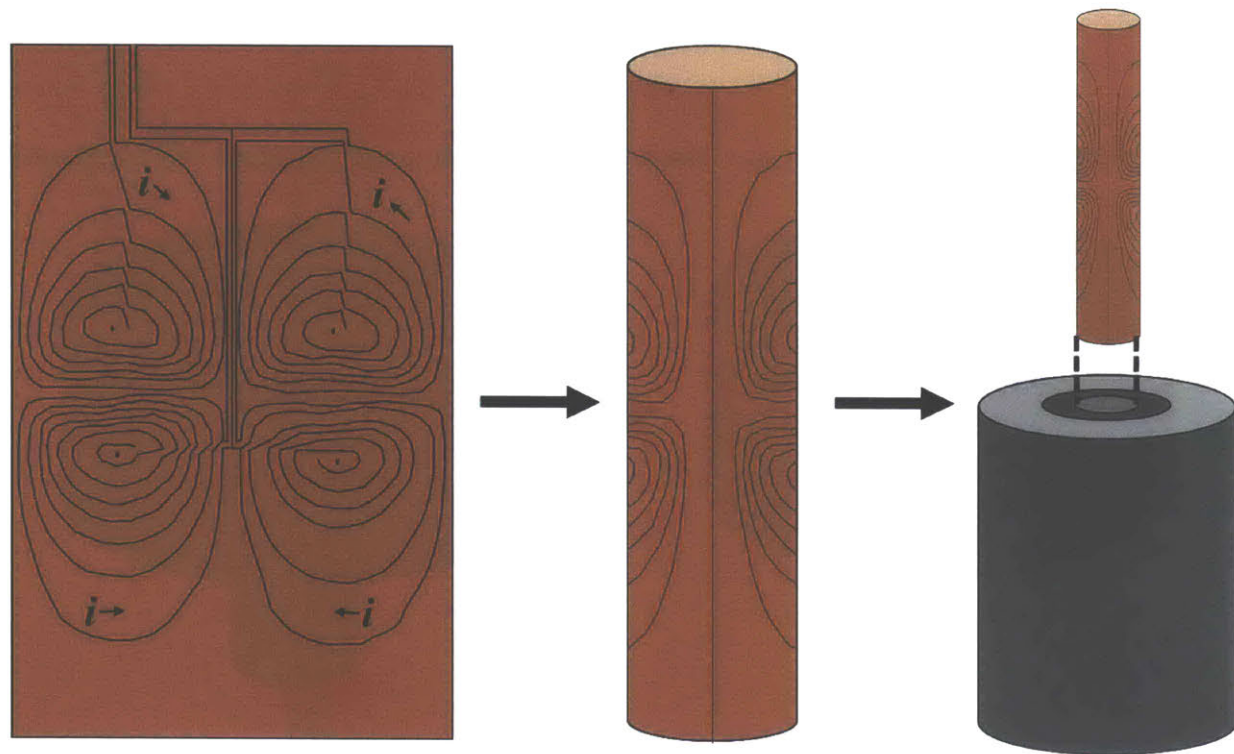


Figure 3-27: After printing, the flexible circuit will be rolled and inserted inside the magnet bore.

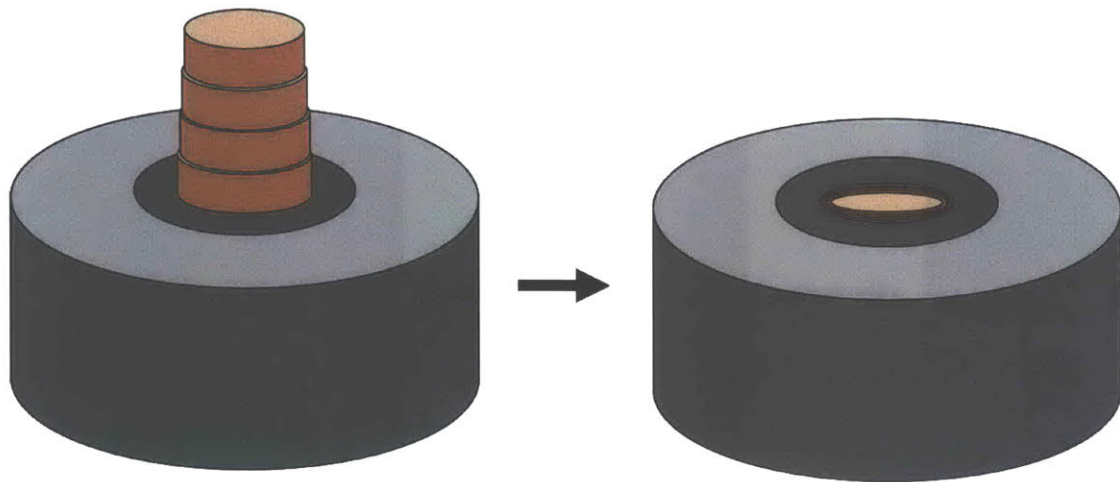


Figure 3-28: The shims to correct each harmonic would nest inside one another within the bore.

By placing limits on the copper geometry to ensure manufacturability, the efficiency of each shim coil can be estimated. The spacing between the traces was constrained to a minimum of 0.4 mm, with a 0.1 mm gap between traces. The copper thickness was set to 70 μm thick, corresponding to the 2 oz. thickness offered by PCB manufacturers. This thickness was chosen rather than the more common 35 μm (1 oz.) thickness in order to maximize the cross-sectional area of the conductor and increase the allowed current. With the given specifications, the current density is $4.76 \times 10^7 \text{ A/m}^2$ for 1 A of current in the minimum cross-section.

Tables 3.5 and 3.6 give the projected shim efficiencies based on these geometric limits for the 6 mm and 10 mm diameters, respectively. Shown are the per unit current results for the maximum compensating field B_{cmps} , the ppm corrected, the harmonic coefficients and the dissipated power. The harmonic coefficient b gives the scaling factor for each spherical harmonic, for example bx for the X shim or $b[2z^2 - (x^2 + y^2)]$ for the Z^2 shim, where the field is in Tesla and the length scale in mm.

Table 3.5: The 6 mm diameter results for the maximum compensating field, maximum ppm corrected in a 0.5 T magnet, and harmonic coefficient with mm length scale are given for each of the shims, assuming 1 A of current supplied.

Harmonic	$B_{cmpl} (\mu\text{T})$	PPM Corrected	Harmonic Coefficient	Power Dissipated (mW)
$T_{1,-1}$	1,200	2,488	6.366×10^{-4}	296
$T_{1,0}$	1,300	2,662	7.069×10^{-4}	329
$T_{1,1}$	850	1,701	4.761×10^{-4}	287
$T_{2,-2}$	496	993	4.425×10^{-5}	314
$T_{2,-1}$	671	1,342	1.310×10^{-4}	227
$T_{2,0}$	528	1,507	1.617×10^{-4}	210
$T_{2,1}$	321	642	2.353×10^{-4}	183
$T_{2,2}$	296	592	3.279×10^{-5}	206
$T_{3,-2}$	214	429	6.787×10^{-6}	199
$T_{3,-1}$	344	689	2.831×10^{-5}	195
$T_{3,0}$	255	510	4.211×10^{-5}	126
$T_{3,1}$	178	356	1.190×10^{-5}	181
$T_{3,2}$	140	280	4.048×10^{-6}	117
$T_{4,0}$	156	313	1.148×10^{-5}	143

Table 3.6: The 10 mm results for the maximum compensating field, maximum ppm corrected in a 0.5 T magnet, and harmonic coefficient with mm length scale are given for each of the shims, assuming 1 A of current supplied.

Harmonic	$B_{cmpl} (\mu\text{T})$	PPM Corrected	Harmonic Coefficient	Power Dissipated (mW)
$T_{1,-1}$	684	1,368	3.630×10^{-4}	639
$T_{1,0}$	927	1,854	4.437×10^{-4}	790
$T_{1,1}$	551	1,102	3.403×10^{-4}	807
$T_{2,-2}$	172	344	1.195×10^{-5}	1,002
$T_{2,-1}$	270	540	4.947×10^{-5}	540
$T_{2,0}$	273	545	6.906×10^{-5}	535
$T_{2,1}$	171	342	9.859×10^{-5}	469
$T_{2,2}$	129	258	1.297×10^{-5}	258
$T_{3,-2}$	49	99	1.861×10^{-6}	683
$T_{3,-1}$	106	213	6.768×10^{-6}	504
$T_{3,0}$	47	94	9.737×10^{-6}	309
$T_{3,1}$	47	94	3.976×10^{-6}	558
$T_{3,2}$	45	90	1.274×10^{-6}	424
$T_{4,0}$	19	37	1.923×10^{-6}	395

Notable from the results is that the 6 mm shims provide a larger magnetic field correction than the 10 mm shims, with the same current supplied. Recall from the Biot-Savart law that the magnetic field generated by a current source scales inversely with the distance squared. This observation suggests a strategy where less efficient shims could be placed at a smaller diameter, closer to the target field area, and more efficient shims could be placed at a larger diameter, closer to the magnet walls.

In the results above, it is typical that more power is required to achieve the same ppm correction for higher order harmonics. However, the magnitude of each harmonic order n scales as $(r/r_0)^n$, where r starts at the center of the region of interest, and r_0 is the maximum radius where the analysis is valid, namely the radius of the largest sphere that contains no magnetic sources [30]. Thus, the level of correction required diminishes with higher orders, helping to balance the decreasing shim efficiencies. In the following section, the efficiency of these shims is compared to the field measured in Section 3.3.1 in order to estimate the current and power requirements for active shims.

3.3.3 Active Shim Feasibility

The purpose of the field measurement and shim analyses is to assess whether shimming the magnetic field of a small portable magnet would be possible using active shims only, at least for short experiments. As a final step, this section estimates how much current the shims of Section 3.3.2 would require to shim the field measured in Section 3.3.1, and discusses the outlook for this strategy.

Required Current

Harmonic coefficients are used to make the comparison. Section 3.3.1 reported measurements of the harmonics of the smaller shim-a-ring magnet, and Section 3.3.2 the computation the harmonics of the shims with 1 A of current supplied. By taking the ratio of these two coefficients, the current and current density required to correct the field is found. Tables 3.7 and 3.8 below give this analysis for the 6 mm and 10 mm diameter shims.

Table 3.7: The current and current density required to correct each harmonic of the measured field are computed by taking the ratio of the measured coefficients and the **6 mm diameter** simulation results for 1 A supplied current.

Harmonic	Measured Coefficient	Shim Coefficient (6 mm)	Correcting Current (mA)	Current Density (A/m ²)
$T_{1,-1}$	-2.370×10^{-4}	6.366×10^{-4}	372	1.77×10^7
$T_{1,0}$	-8.006×10^{-4}	7.07×10^{-4}	1,132	5.39×10^7
$T_{1,1}$	-4.25×10^{-5}	4.76×10^{-4}	89	4.25×10^6
$T_{2,-2}$	9.037×10^{-6}	4.43×10^{-5}	204	9.72×10^6
$T_{2,-1}$	-6.184×10^{-6}	1.31×10^{-4}	47	2.25×10^6
$T_{2,0}$	-2.553×10^{-4}	1.62×10^{-4}	1,578	7.52×10^7
$T_{2,1}$	-1.809×10^{-5}	2.35×10^{-4}	77	3.66×10^6
$T_{2,2}$	-6.891×10^{-5}	3.28×10^{-5}	2,101	1.00×10^8
$T_{3,-2}$	-1.694×10^{-7}	6.79×10^{-6}	25	1.19×10^6
$T_{3,-1}$	-5.32×10^{-6}	2.83×10^{-5}	188	8.95×10^6
$T_{3,0}$	-6.028×10^{-5}	4.21×10^{-5}	1,431	6.82×10^7
$T_{3,1}$	9.610×10^{-6}	1.19×10^{-5}	808	3.85×10^7
$T_{3,2}$	-4.292×10^{-6}	4.05×10^{-6}	1,060	5.05×10^7
$T_{4,0}$	-1.705×10^{-5}	1.15×10^{-5}	1,485	7.07×10^7

Table 3.8: The current and current density required to correct each harmonic of the measured field are computed by taking the ratio of the measured coefficients and the **10 mm diameter** simulation results for 1 A supplied current.

Harmonic	Measured Coefficient	Shim Coefficient (10 mm)	Correcting Current (mA)	Current Density (A/m ²)
$T_{1,-1}$	-2.370×10^{-4}	3.63×10^{-4}	653	3.11×10^7
$T_{1,0}$	-8.006×10^{-4}	4.44×10^{-4}	1,804	8.59×10^7
$T_{1,1}$	-4.250×10^{-5}	3.40×10^{-4}	125	5.95×10^6
$T_{2,-2}$	9.037×10^{-6}	1.91×10^{-5}	472	2.25×10^7
$T_{2,-1}$	-6.184×10^{-6}	4.95×10^{-5}	125	5.95×10^6
$T_{2,0}$	-2.553×10^{-4}	6.91×10^{-5}	3,696	1.76×10^8
$T_{2,1}$	-1.809×10^{-5}	9.86×10^{-5}	183	8.74×10^6
$T_{2,2}$	-6.891×10^{-5}	1.30×10^{-5}	5,314	2.53×10^8
$T_{3,-2}$	-1.694×10^{-7}	1.86×10^{-6}	91	4.34×10^6
$T_{3,-1}$	-5.32×10^{-6}	6.77×10^{-6}	786	3.74×10^7
$T_{3,0}$	-6.028×10^{-5}	9.74×10^{-6}	6,190	2.95×10^8
$T_{3,1}$	9.610×10^{-6}	3.98×10^{-6}	2,417	1.15×10^8
$T_{3,2}$	-4.292×10^{-6}	1.27×10^{-6}	3,368	1.60×10^8
$T_{4,0}$	-1.705×10^{-5}	1.92×10^{-6}	8,870	4.22×10^8

As noted in the previous section, the shims designed for a smaller diameter are significantly more efficient. Based on the results in the tables above, it would be possible to keep the current density in every shim 10^8 A/m² or less, by placing the more efficient shims in the outer layers and the less efficient shims in the inner layers. The maximum current would be 2.10 A, in the $T_{2,2}$ shim.

In steady state, the system will rise to a constant, elevated temperature, and the heat from the shims will be dissipated into the surroundings. Curves from the IPC-2221 standard for PCB design can give an estimate of how high the temperature would rise [58]. The tightly packed shims would not be exposed to air on their faces, making them comparable to internal PCB traces. According to the IPC -221 curves, internal traces with the minimum cross-section permitted in the shims (0.3 mm x 70 μ m) would experience a temperature rise of 45°C when carrying 1.5 A. Extrapolating the curves further [59], a continuous current of 2.1 A would result in a temperature rise of 80°C. A temperature rise of this magnitude would not compromise the integrity of the flex PCB [54].

The shims, however, only carry current for the duration of the NMR measurement, which in many cases is less than a second: experiments need last only as long as the FID is detectable. If averaging is desired, it is necessary to wait about four times the length of T_1 before repeating the experiment, during which time the shims could be dormant. Estimating the power dissipated by the operating shims provides further insight into their transient behavior.

To approximate the total power dissipation, the 6 mm diameter shim values were used for the 7 least efficient shims ($T_{1,0}$, $T_{2,0}$, $T_{2,2}$, $T_{3,0}$, $T_{3,1}$, $T_{3,2}$ and $T_{4,0}$), and the 10 mm shim values for the 7 most efficient shims ($T_{1,-1}$, $T_{1,1}$, $T_{2,-2}$, $T_{2,-1}$, $T_{2,1}$, $T_{3,-2}$, $T_{3,-1}$). Of course, each nested shim would in actuality have a slightly different diameter, but employing the simulation results in this way mimics the proposed strategy of placing the less efficient shims towards the center. The estimated power dissipated by each shim when applying the required correcting current is given in Table 3.9.

Table 3.9: To estimate the total power dissipated by the correcting shims, the less efficient shims are modeled at the narrower diameter and the more efficient shims at the wider diameter, and the power dissipation is calculated based on the required correcting current.

Harmonic	Modeled Diameter	Required Correcting Current (A)	Power Dissipated (mW)
$T_{1,-1}$	10 mm	0.65	272
$T_{1,0}$	6 mm	1.13	422
$T_{1,1}$	10 mm	0.12	13
$T_{2,-2}$	10 mm	0.47	223
$T_{2,-1}$	10 mm	0.13	8
$T_{2,0}$	6 mm	1.58	523
$T_{2,1}$	10 mm	0.18	16
$T_{2,2}$	6 mm	2.10	910
$T_{3,-2}$	10 mm	0.09	6
$T_{3,-1}$	10 mm	0.79	311
$T_{3,0}$	6 mm	1.43	258
$T_{3,1}$	6 mm	0.81	118
$T_{3,2}$	6 mm	1.06	132
$T_{4,0}$	6 mm	1.49	315

From the sum of the above estimates, the total power required for all the shims is a modest 3.5 W. The total mass of copper in the shims is on the order of 100 g, where 100 g is a lower bound estimate. Modeling the copper as a lumped parameter of uniform temperature, the temperature rise can be estimated by the specific heat formula:

$$Q = mc\Delta T, \quad (3.12)$$

where Q is the heat energy, m is the substance mass, c is the specific heat (385 J/kg·K for copper), and ΔT is the change in temperature. Plugging in, the temperature change for 3.5 W of power is found to be only 0.1°C per second. This estimate neglects any heat dissipated into the surroundings, giving an upper-bound estimate of the average temperature in the copper during short experiments.

For the stochastic techniques presented in the following chapter, the experiment needs to be at least ten times longer than T_1 . Most substances could be measured in less than a second. Pure water has an exceptionally long relaxation T_1 time, 4 seconds, but even performing a stochastic experiment on water would raise the copper temperature by only about 4°C. Thus, actively correcting the field looks promising.

Further Development

While these results show that it would be feasible to actively correct the shim-a-ring magnet, further development work is needed. These results are based on the measurements of a single magnet, and to realize its potential the design must be shown to work for all or most magnets of the same geometry. Additionally, although the current to correct every measured harmonic is manageable, more extensive measurements including higher harmonics are needed for two reasons. First, it must be ascertained whether achieving sub-ppm homogeneity requires correction of additional harmonics. Secondly, any significant content in the unmeasured higher orders is aliased down into the lower order coefficients [30]. Higher and higher orders need to be added to the measurement until the coefficients stabilize and converge.

Careful attention will need to be paid to heat dissipated into the magnet, because

the strength of the magnetic field shifts with temperature [60]. The temperature coefficient for a grade 48 NdFeB magnet is 1200 ppm/ $^{\circ}$ C, meaning that even a 1 $^{\circ}$ C change in the 0.5 T magnet would shift resonance by 25 kHz.

In the end, the main limitation of this design is space, rather than heat management. The fourteen computed shims, each with a thickness of about 200 μ m, would reduce the bore diameter from 10 mm to 4.4 mm, which is not large enough to accommodate a standard 5 mm sample tube. This issue could be solved by increasing the scale of the magnet design to enlarge the bore, at the cost of assembly mass. Alternatively, the sample size could be reduced, at the cost of signal strength.

The active field correction strategy would be ideal for designs requiring correction only up to the second order. The shim-a-ring was selected for its ease of assembly and favorable field strength at reasonable mass. As with all magnet designs, the field homogeneity of the physical realization is orders of magnitude worse than the simulation. With only a single magnet, errors in alignment have been circumvented. The remaining errors, then, are most likely due to imperfections in the magnetizing field. Deeper investigation is warranted into the manufacturing of the magnets, with the goal of improving the homogeneity such that fewer harmonic orders require correction.

Chapter 4

Stochastic Spin Density

NMR experiments that use stochastic excitation hold great promise for miniaturized spectrometers. They are low power, making them ideal for a portable device. They use excitation pulses that are orders of magnitude smaller than those in the more common Fourier transform (FT) NMR techniques, which greatly simplifies requirements for the electronics. The experiments are exceedingly simple [61], making them ideal for a low-cost device available to unspecialized users. Lastly, higher dimensional experiments hold a special promise. Where FT NMR must painstakingly measure one at a time the varying delays between pulses employed in 2D or 3D experiments, stochastic NMR gathers all the information in a single experiment that lasts no longer than a simple 1D measurement [62]. These short experiments would make multidimensional measurements possible using the low-cost active shimming strategy explored in Section 3.3.2.

While the promise of multidimensional experiments is left to future work, this chapter starts the exploration of miniature, stochastic NMR by taking 1D measurements in an inhomogeneous magnetic field. Section 4.1 takes a more detailed look at stochastic excitation and data processing, and explores uses for the technique in an inhomogeneous magnetic field. Section 4.2 presents simulations of stochastic experiments using exact solutions to the Bloch equations. Finally, Section 4.3 presents experimental measurements taken with the spectrometer of Ch. 2 and the magnet of Ch. 3.

4.1 Correlation Techniques

Stochastic NMR has been an area of interest since the late 1950's. Despite its long history, the technique never gained popularity, due to its non-intuitive nature and the systematic noise inherent in multi-dimensional measurements [62]. Single-dimensional measurements, however, are free from systematic noise [63]. Furthermore, the data processing lends itself to automation, which would actually be preferable in a low-cost device.

4.1.1 Derivation

The core idea behind stochastic excitation is to send in a series of pulses, each one of which provokes a free induction decay. If the pulses are sufficiently low power, then the NMR response will be linear. Then the measured NMR signal at a given time will be a superposition of the responses to all the previous pulses, given by the convolution of the FID and the input:

$$O(t) = \int_{-\infty}^t I(\tau) \cdot F(t - \tau) d\tau, \quad (4.1)$$

where $F(t)$ is the FID, $I(t)$ is the input signal, and $O(t)$ is the output signal. In the equation above, the FID is equivalent to the impulse response used in system analysis [64]. The response to the pulses can be approximated as linear for flip angles less than 30° , where the small angle approximation is valid. In this region, the transverse magnetization is given by,

$$M^+ = M_0 \sin \alpha \approx \alpha M_0, \quad (4.2)$$

where M^+ is the transverse magnetization, M_0 is the magnetization magnitude, and α is the flip angle. Similarly, the longitudinal magnetization M_z is given by,

$$M_z = M_0 \cos \alpha \approx M_0. \quad (4.3)$$

After sending a series of pulses and measuring the response, the challenge is to

then extract the FID. For particular types of inputs, recovering the FID becomes possible using correlation techniques. The autocorrelation $A(t)$ of the input is given by,

$$A(t) = \lim_{T \rightarrow \infty} \frac{1}{2T} \int_{-T}^{+T} I(\tau) \cdot I(t + \tau) d\tau. \quad (4.4)$$

The autocorrelation multiplies then averages the input signal with a time-shifted version of itself, thus finding the level of correlation [65]. Similarly, the input-output crosscorrelation $C(t)$ measures the correlation between the input and time-shifted output:

$$C(t) = \lim_{T \rightarrow \infty} \frac{1}{2T} \int_{-T}^{+T} I(\tau) \cdot O(t + \tau) d\tau. \quad (4.5)$$

Using these definitions, Eq. 4.1 can be rewritten as [66],

$$C(t) = \int_{-\infty}^t A(\tau) \cdot F(t - \tau) d\tau. \quad (4.6)$$

For an ideal white noise input, extracting the FID is trivial. Because any two samples of white noise are statistically independent, the signal correlates to itself only with zero time shift, and the autocorrelation function is proportional to a delta function $\delta(t)$. Then Eq. 4.6 becomes $C(t) = F(t)$, and the FID can be found simply from the cross-correlation.

Unfortunately, it is not possible to experimentally produce the infinite frequency bandwidth of ideal white noise [65]. Computation of the FID is still possible, however, using pseudo-noise, whose autocorrelation approximates a delta function. A certain type of pseudo-noise called a maximum length sequence, or m-sequence, has attractive properties. The m-sequence is a deterministic, periodic signal with very low redundancy, meaning that it has a low incidence of repeating portions of the waveform. An n -stage shift register can be used to produce a sequence of $M = 2^n - 1$ elements, as described in detail elsewhere [65, 66, 67, 68]. The sequence then repeats after M elements. In $(+1, -1)$ notation, the sequence contains $(M + 1)/2$ minus ones, and $(M - 1)/2$ plus ones, in seemingly random order. The autocorrelation of

the m-sequence is one for zero time shift, and $-1/M$ for all other time shifts. For a sequence, the autocorrelation is given by,

$$A_j = \frac{1}{M} \sum_k I_k \cdot I_{j+k}, \quad j, k = 0, \dots, M-1, \quad (4.7)$$

where the sum is taken cyclically to represent an infinitely repeating excitation sequence. Similarly, the crosscorrelation of a discrete sequence is given by,

$$C_j = \frac{1}{M} \sum_k I_k \cdot O_{j+k}, \quad j, k = 0, \dots, M-1, \quad (4.8)$$

and thus Eq. 4.6 becomes

$$C_j = \sum_k = A_{j-k} \cdot F_k, \quad j, k = 0, \dots, M-1, \quad (4.9)$$

where the sums are again taken cyclically.

Once again, the input autocorrelation must be deconvolved from the input-output crosscorrelation to find the FID, and once again the autocorrelation properties of the input hold the key. Using the autocorrelation properties of m-sequences, Eq. 4.9 becomes

$$C_j = F_j - \frac{1}{M} \sum_k F_k + \frac{1}{M} F_j, \quad j, k = 0, \dots, M-1,$$

and thus,

$$(M+1)F_j = C_j + \sum_k F_k, \quad j, k = 0, \dots, M-1.$$

Using the m-sequence property that $\sum_j I_j = -1$, the expression above can be used to show that $\sum_j F_j = -\sum_j O_j$, which allows us to write,

$$(M+1)F_j = C_j - \sum_j O_j, \quad j, k = 0, \dots, M-1. \quad (4.10)$$

In this way, the FID is written in terms of known quantities. This analysis has largely been adapted from [66], where Kaiser also shows how to write Eq. 4.10 in

the form of matrix multiplication. Data gathered from simulation and experiment were processed using this simple matrix multiplication, and the MATLAB code is included in Appendix A.2. After performing deconvolution to find the FID, the Fourier transform can be applied as usual to compute the NMR spectrum.

4.1.2 Experimental Details

The analysis above shows how to use m-sequence excitation to find the FID. The sequence is composed of plus and minus ones, and requires a sample of the magnetization concurrent to each element. In practice, excitation pulses are sent at every timestep dt , and the magnetization is sampled between the pulses. The amplitude, phase, duration or frequency of the pulses can be modulated according to the m-sequence. For example, pulses could be sent with two different phases, depending on the current value of the m-sequence. Similarly, the amplitude of the pulses at each time step could either be zero or some fixed value, again determined by the m-sequence.

Because the excitation power is spread throughout the duration of the experiment, the magnitude of the individual pulses is much smaller than in FT NMR, as depicted in Fig. 4-1.

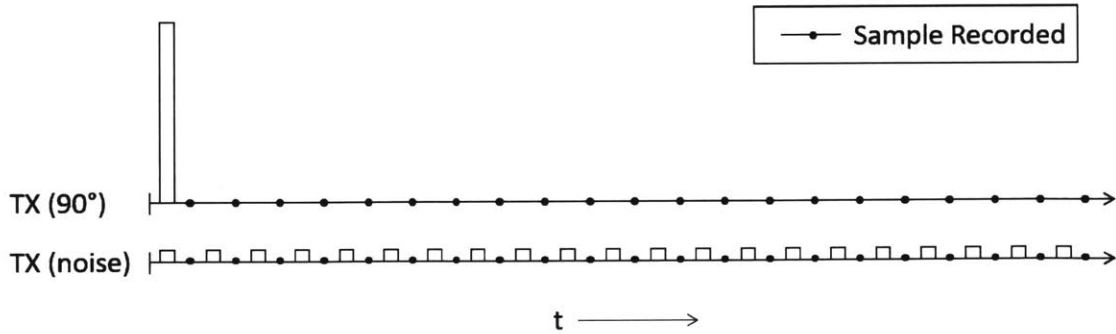


Figure 4-1: In FT NMR, the magnetization is sampled after a single large transmit (TX) pulse. For stochastic excitation, the input energy is spread throughout the experiment with a series of small pulses, and the magnetization is sampled after each one.

These smaller pulses give stochastic excitation its characteristic lower power require-

ments.

No special equipment is needed to perform experiments with stochastic excitation: the same spectrometer can be used for both stochastic and FT NMR [69]. Similarly, in both cases, the sampling frequency and maximum pulse width are determined by the system bandwidth. Because the frequency is mixed down, it is not necessary to sample as fast the Larmor frequency. As explained in Section 1.2.10, the signal is shifted to low frequencies, and sampling must be fast enough to capture the range of frequencies present in the spectrum, or the range of frequencies due to an inhomogeneous magnetic field. In either case, the sampling frequency must be at least twice the system bandwidth, in order to avoid aliasing. Likewise, the pulses must be short enough to excite the entire system bandwidth (see Section 1.2.3).

In a fully-realized low-cost device, the excitation sequence could be preprogrammed, and the user would simply need to press play. The excitation power would need to be adjusted for different samples. The optimal excitation power depends on the T_1 relaxation time of the sample [70], but can be found heuristically by testing different excitation levels. Overall, stochastic excitation holds great promise in the context of miniature NMR, as a low power technique with simple experiments and the potential for automated data processing.

4.1.3 Measurement in an Inhomogeneous Field

The NMR spectrum carries powerful, detailed information about the sample. In an inhomogeneous magnetic field, the spectra are obscured due to inhomogeneous broadening (Section 1.2.5). Techniques have been developed in FT NMR, however, to recover some information: the pulse-echo experiment (Section 2.5) can be used to find relaxation times in the presence of field inhomogeneity. Comparable techniques have not been demonstrated using stochastic excitation, though finding relaxation times from a three dimensional measurement in an inhomogeneous field should be possible [71].

Using only a linear analysis, the FID found through correlation techniques should match what is observed after a 90° pulse: the total signal amplitude rapidly decays

due to interference between the nuclei of different resonant frequencies. One type of information still remains even in this case: the initial amplitude is proportional to the number of nuclei present.

The measured NMR signal is the sum of the contributions from all the individual nuclei. Thus, the total signal amplitude scales directly with the number of resonant nuclei in the sample. After an excitation pulse, the magnetization of the nuclei are initially aligned, even in an inhomogeneous field. Then as the spins precess at different frequencies, they become more and more out of phase. Assessing the quantity of resonant nuclei by looking at the initial FID amplitude is called a *spin density* measurement.

Although simple, the spin density measurement provides valuable information. It can, for example, measure the oil content in food [72], seeds [73], and wastewater [74], the hydrogen content in fuel [75], and the fluorine content in toothpaste [76], industrial waste [77], and raw materials [78]. The measurement is made by comparing the signal amplitude to that of reference samples. Two samples at minimum are required to define the calibration curve, which linearly connects them.

Spin density measurements can be performed with either stochastic or FT NMR methods, but there is one particular advantage to the stochastic technique: the reduction of dead time. Dead time refers to how much time passes before the receiver can start recording the NMR signal after an excitation pulse. The receiver electronics are extremely sensitive in order to detect the tiny NMR signal, and they saturate during the excitation, even though the pulses are attenuated by the T/R switch. The speed with which the receiver recovers from saturation is the dead time. Because the excitation pulses are much smaller in stochastic NMR, the dead time is reduced, and the initial signal amplitude can be recorded with more accuracy because there has been less time to dephase.

The following sections verify the efficacy of measuring stochastic spin density in simulation (Section 4.2) and experiment (Section 4.3). Measuring NMR spectra using stochastic excitation in a compact device is theoretically possible using the shim system outlined in Section 3.3.2, and is left for future work.

4.2 Bloch Simulations

The Bloch equations (Section 1.2.9) are frequently used to model NMR behavior. In FT NMR, the pulses are short relative to the relaxation times, and it is reasonable to neglect relaxation during the pulses. This assumption makes solving the equations straightforward [9]. In stochastic NMR, however, pulses continue throughout the experiment, and neglecting relaxation is no longer a good assumption. Numerical solutions have in the past been used to overcome this difficulty [67]. Here we create a model using the exact solution to the Bloch equations, derived in the 2010 paper by Bain *et al.* [79]. Although the solution is unwieldy, simulations are rapid once implemented in MATLAB. The MATLAB code is available in Appendix A.2.

Data processing for simulations and experiments is identical, which allowed verification that the code worked as expected. Fig. 4-2 shows the results of a simulation. The simulated experiment used amplitude modulation and a ten stage shift register, meaning that a pulse of rf radiation was sent at zero or full amplitude for every time step of the 1023-element m-sequence. The pulses were sent and the system sampled at a rate of 2 kHz. The simulated system had a resonant frequency in the rotating frame of $\Omega_0 = 70$ Hz (see Section 1.2.8), and a T_2 relaxation of 0.2 s. These system parameters display as expected in the impulse response (FID), where a 70 Hz sinusoid decays exponentially with a time constant of 0.2 s. After Fourier transform there is a resonant peak at 70 Hz, offset slightly due to the coarse resolution of the spectrum.

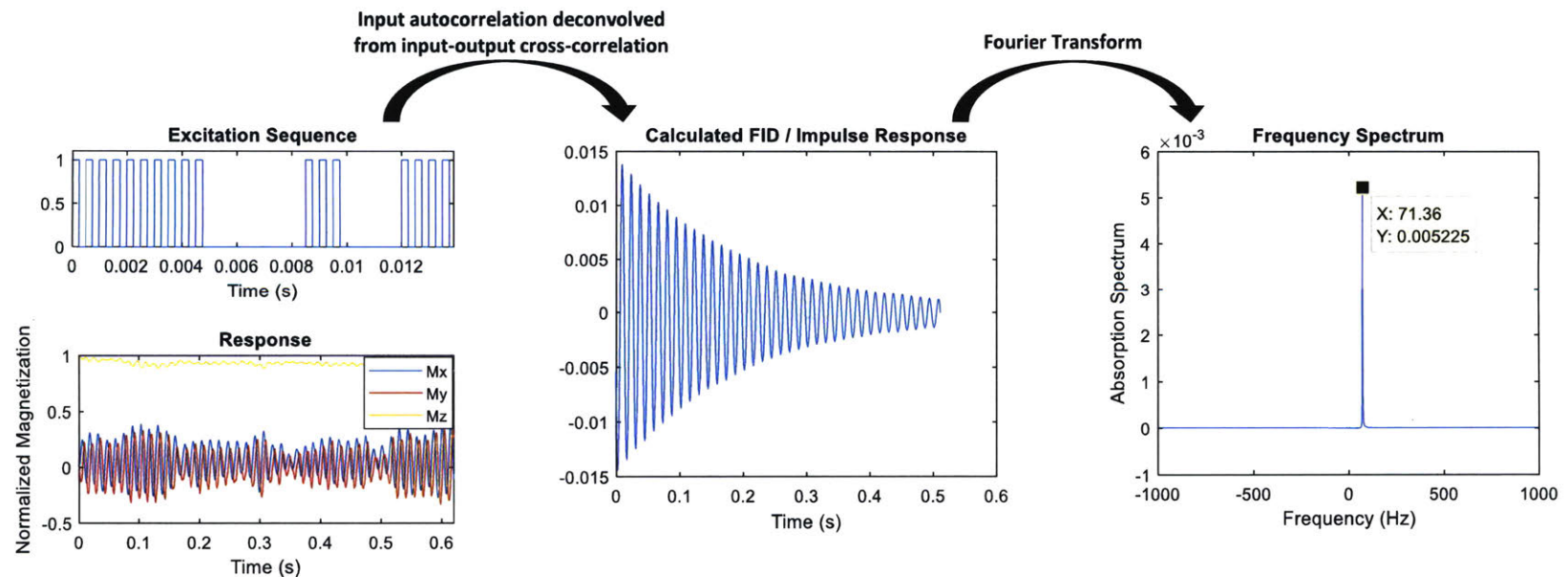


Figure 4-2: A stochastic experiment and data processing were simulated. A packet of rf excitation is sent with every pulse, which is amplitude modulated according to an m-sequence. The M_x and M_y components can be experimentally recorded, and in the simulation the M_z component is available as well. The FID is obtained by deconvolving the input and output, and displays the appropriate resonant frequency and decay rate. Likewise, Fourier transform of the FID gives a peak at resonance.

Only the beginning section of the pulse sequence is shown in Fig. 4-2, in order to display individual pulses that gate the rf excitation. In the response, the x - and y -components of the magnetization oscillate at the Larmor frequency and are offset by 90° , showing the precession of the magnetization about the z -axis. The z -component of the magnetization remains close to unity, indicating that the magnetization vector remains relatively aligned with the B_0 field throughout the experiment. It is critical that this be the case. The strength of the net magnetic moment will shrink if kept out of alignment with the external field for periods long relative to T_1 , a phenomenon called saturation.

There exists a great trade-off in stochastic NMR. The farther the magnetization tilts away from the z -axis, the greater the transverse magnetization and larger the measured signal (Section 1.2.3). At the same time, departing from alignment with the B_0 field introduces a saturation nonlinearity [67], which decreases the strength of the net magnetization and distorts the data. Fig. 4-3 maps the path of the magnetization vector with pulses of increasing flip angle. For very small flip angles, the transverse magnetization becomes too small to detect. For large angles, the system becomes highly nonlinear. There exists in between these extremes a range of excitation amplitudes that tickle the magnetization enough for it to be measurable and reasonably linear so as not to distort the measured spectra.

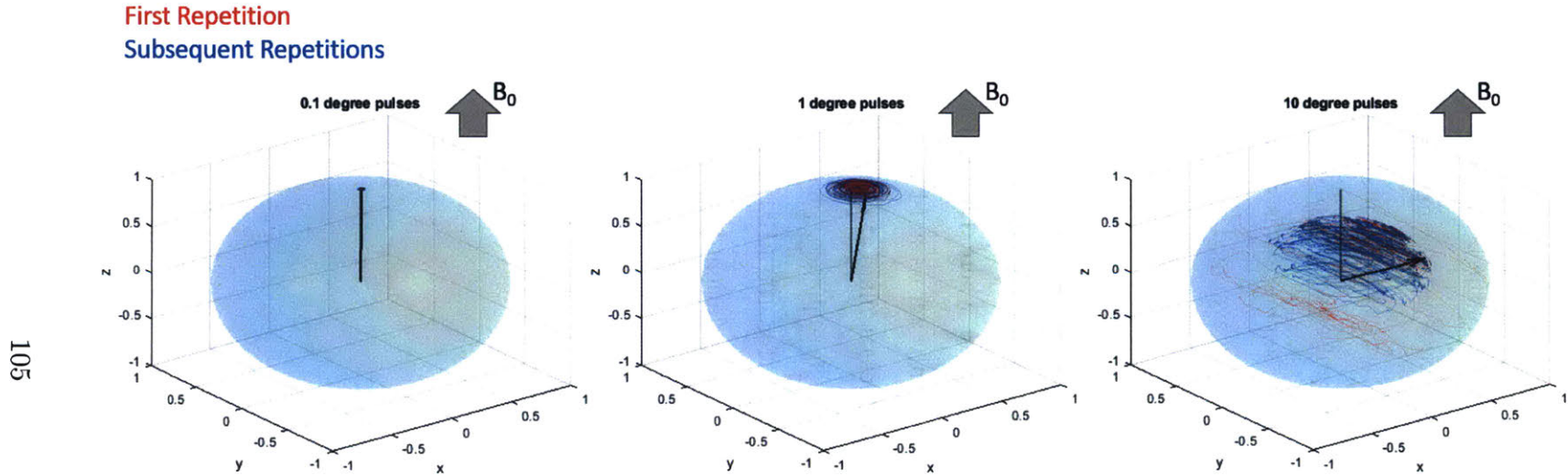


Figure 4-3: The magnetization path is traced during a stochastic experiment with using various flip angles. With excitation too small, transverse magnetization is not generated (0.1° pulses). With excitation too large, the system saturates, decreasing the magnitude of the magnetization vector (10° pulses). An intermediate value (1° pulses) generates transverse magnetization while maintaining linearity. The modeled system has $T_1 = T_2 = 10$ ms, $\Omega_{\text{ref}} = 1$ kHz. The amplitude-modulated experiment was set to run at 50 kHz with a 50% duty cycle, and the 2047 pulse sequence was repeated 10 times. The magnetization path for the first repetition is traced in red, and the following nine repetitions in blue.

The analysis of Section 4.1 assumes a time-invariant system. This requirement is satisfied by allowing the system to reach a dynamic equilibrium. The excitation sequence is repeated multiple times, with only the later repetitions included in analysis. In practice, it is usually sufficient to discard the first repetition of the sequence [67]. The sequence must run for a duration longer than T_1 , so that the system will not have memory of the time before the pulses were applied. For the simulations and experiments of this thesis, the excitation sequence was repeated 10 times. The first response was discarded, and the other 9 are averaged, reducing the measured noise.

To confirm that spin density measurements would be possible in an inhomogeneous field, simulations with different resonant frequencies were summed. As expected, the initial value of the impulse response was large, then decayed rapidly compared to the T_2 time of the individual frequencies.

Fig. 4-4 shows the results for a system where 1280 different frequencies were summed, with the resonance spread evenly across a 14 kHz bandwidth. Unlike in Fig. 4-2, the measured magnetization does oscillate at one particular frequency. This experiment used a 2047 element excitation sequence, phase modulation, a flip angle of 0.3° per pulse and a 50% duty cycle for 100 kHz sampling. The sample was modeled to have $T_1 = T_2 = 0.2$ s. In this simulation, the information is carried in the imaginary channel. By shifting the phase of the excitation, the energy of the signal can be shifted between the two channels. In FT NMR, the phase of the excitation is commonly adjusted so that the NMR signal is entirely recorded in the real channel [1].

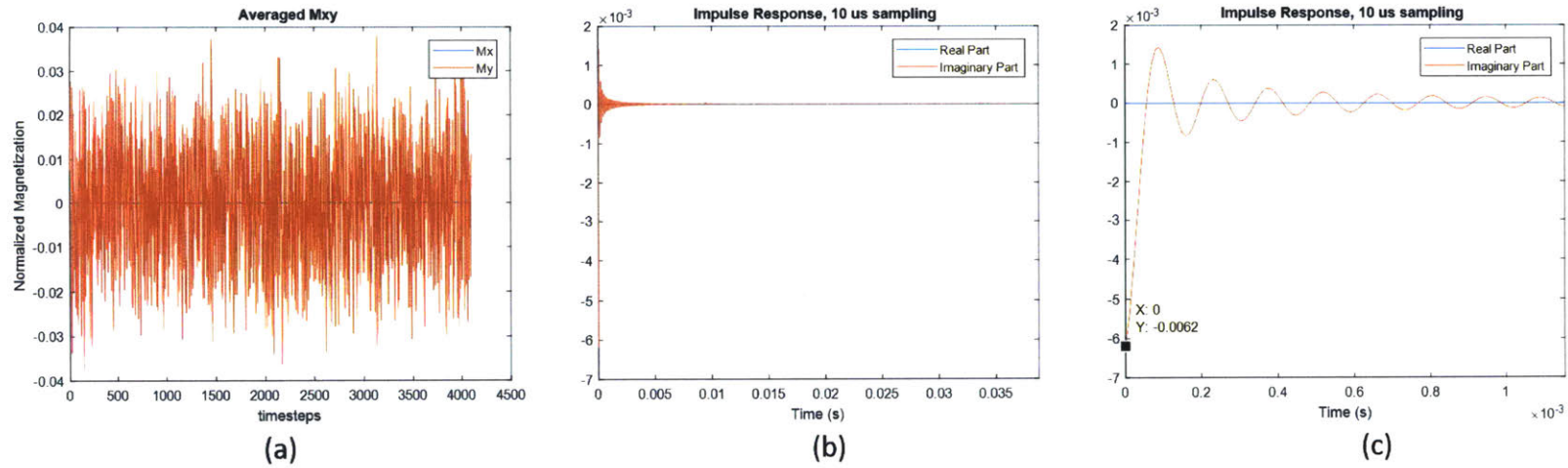


Figure 4-4: The magnetization measured in a stochastic experiment in an inhomogeneous field looks like random noise (a). The impulse response decays rapidly (b), but the initial value remains proportional to the number of spins present (c).

The measurement is robust even with slow sampling and noise. Fig. 4-5 shows the impulse response for the same system as Fig. 4-4 with 33 kHz sampling, both with and without random noise added to the measured signal. The modeled system had a 14 kHz bandwidth, meaning the 33 kHz sampling was close to the Nyquist frequency (28 kHz). The magnitude of the random noise added to the measurement was five times larger than the signal amplitude, though the noise was attenuated by averaging the nine measurements. In spite of these less-than-ideal conditions, the strong signal amplitude at the start of the measurement remains, with the peak value attenuated by only about 6% in the presence of noise. Therefore, stochastic measurement of spin density looks promising, even in an inhomogeneous field.

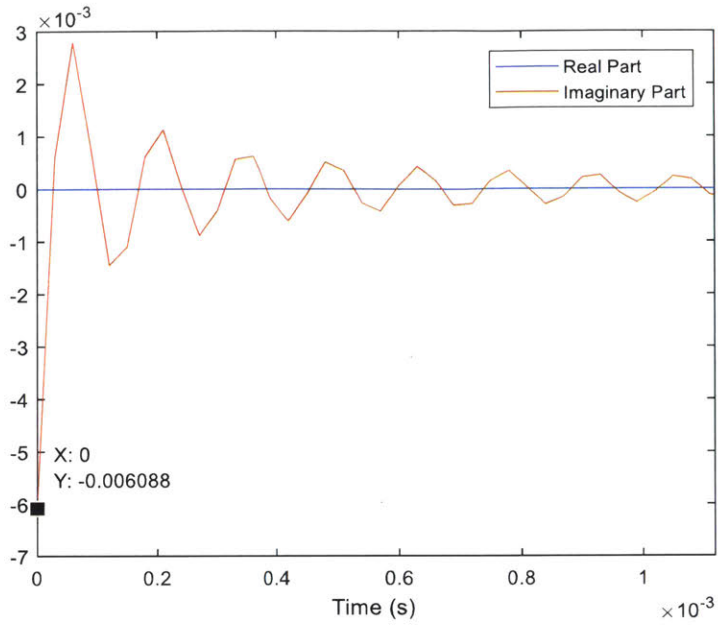
In the following section, the feasibility of stochastic spin density is confirmed experimentally.

4.3 Experimental Measurements

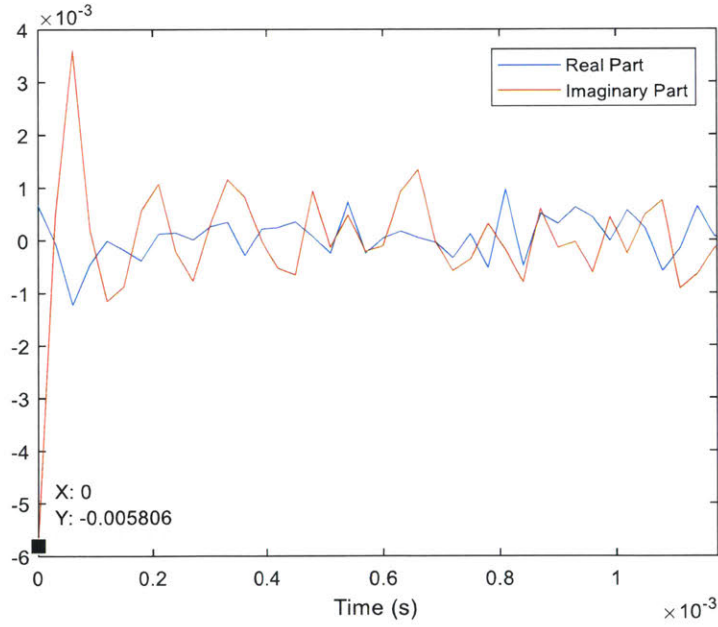
The proposed method of measuring spin density with stochastic excitation appeared promising in simulation (Section 4.2). To verify the technique experimentally, samples containing different ratios of water and heavy water were tested. In water, 99.98% of the hydrogen atoms are protium, whose nucleus is a single proton. Heavy water contains the hydrogen isotope deuterium, whose nucleus is composed of one proton and one neutron. The two isotopes are chemically equivalent, but have different Larmor frequencies because they contain different nuclear species.

Using the spectrometer described in Chapter 2 and the shim-a-ring magnet of Section 3.3.1, samples were excited at the ^1H resonant frequency of around 20.5 MHz. The protons in the water produced an NMR signal, while the nuclei of the heavy water remained silent. The amplitude of the NMR response could then be compared to the known ratio of protium and deuterium in the sample, thus verifying that spin density was accurately measured.

Fig. 4-6 shows the magnitude of the impulse responses measured for water and heavy water. Both samples were doped with a paramagnetic salt, 5 mM manganese



(a)



(b)

Figure 4-5: Even with sampling close to the Nyquist frequency (a) and noise larger than the NMR signal (b), the initial value of the impulse response changes by less than 10%.

chloride, in order to speed up the relaxation. Pulses were sent and magnetization measured at a rate of 100 kHz. The duty cycle was 25%, meaning each excitation pulse was $2.5 \mu\text{s}$ long. The output of the preamplifier and the local oscillator were both disconnected from the mixer for $3 \mu\text{s}$ after each pulse, to allow noise from the T/R switch to attenuate. Magnetization was sampled at the end of each $10 \mu\text{s}$ cycle. The 1 V_{pp} pulses were sent at the resonant frequency of 20.49 MHz from the signal generator without further amplification. The volume of the excited sample was approximately $10 \mu\text{L}$.

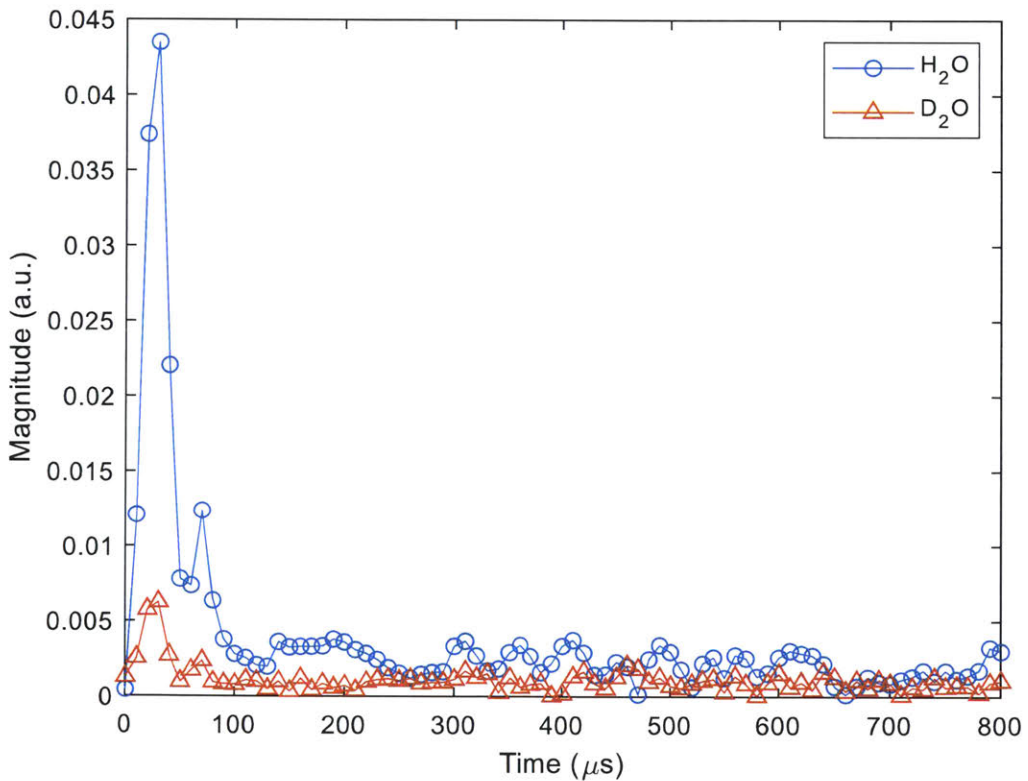


Figure 4-6: The impulse response found for water with 100 kHz sampling was significantly larger than for heavy water, showing that the technique indeed captured the NMR signal.

Signal was present in both the real and imaginary channels, though the raw data from the ADCs appeared to be just noise (Fig. 4-7a). Fig. 4-6 included information

from both channels by plotting the magnitude. For reference, the signal measured for each channel is plotted with the magnitude in Fig. 4-7b.

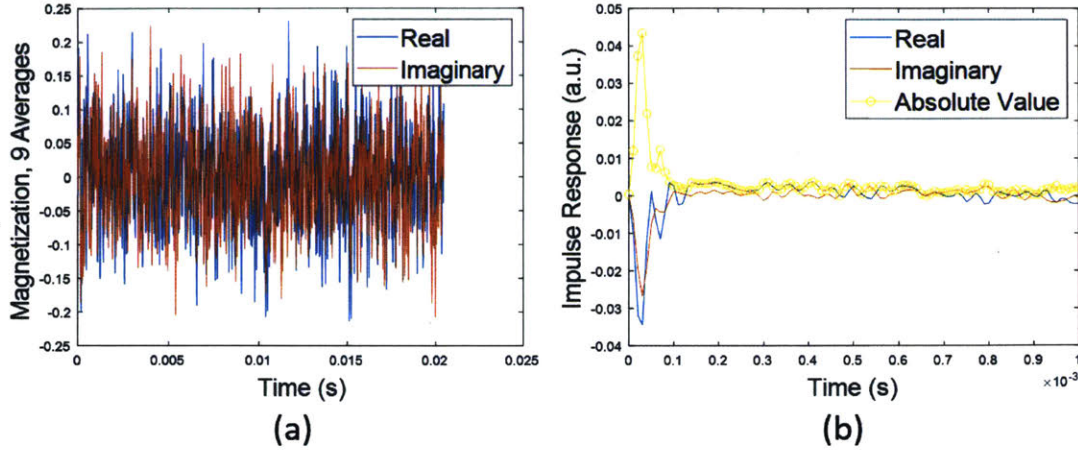


Figure 4-7: The measured signal (a) looked like noise, even after the nine repetitions were averaged. The impulse response (b) showed that NMR signal was present in both the real and imaginary channels, and thus the signal magnitude is considered when performing further analysis.

As can be seen in Fig. 4-6, an artifact from the excitation appears as a small initial peak in the heavy water impulse response. This peak likely came from the mixer, because it decreased in magnitude when switches were in place to isolate the mixer from the preamp output and the LO during the excitation pulses, using the configuration described in Ch. 2. With the mixer sufficiently isolated the response is dominated by the NMR signal, and the excitation artifact simply adds an offset. The maximum amplitude measured for various ratios of water and heavy water is shown in Fig. 4-8. Although the peak value for heavy water is higher than the noise floor, there is no departure from linearity in the measurements of water/heavy water ratios.

The linearity of these measurements confirms that the method accurately captures spin density information. The measurements are repeatable: the 95% confidence interval, found by repeating the measurements 10 times, encompasses a range only 3% of the peak water magnitude.

The linear relationship was also present using other types of analysis. Excellent correlation was obtained by integrating the FID magnitude. Fig. 4-9 shows the results

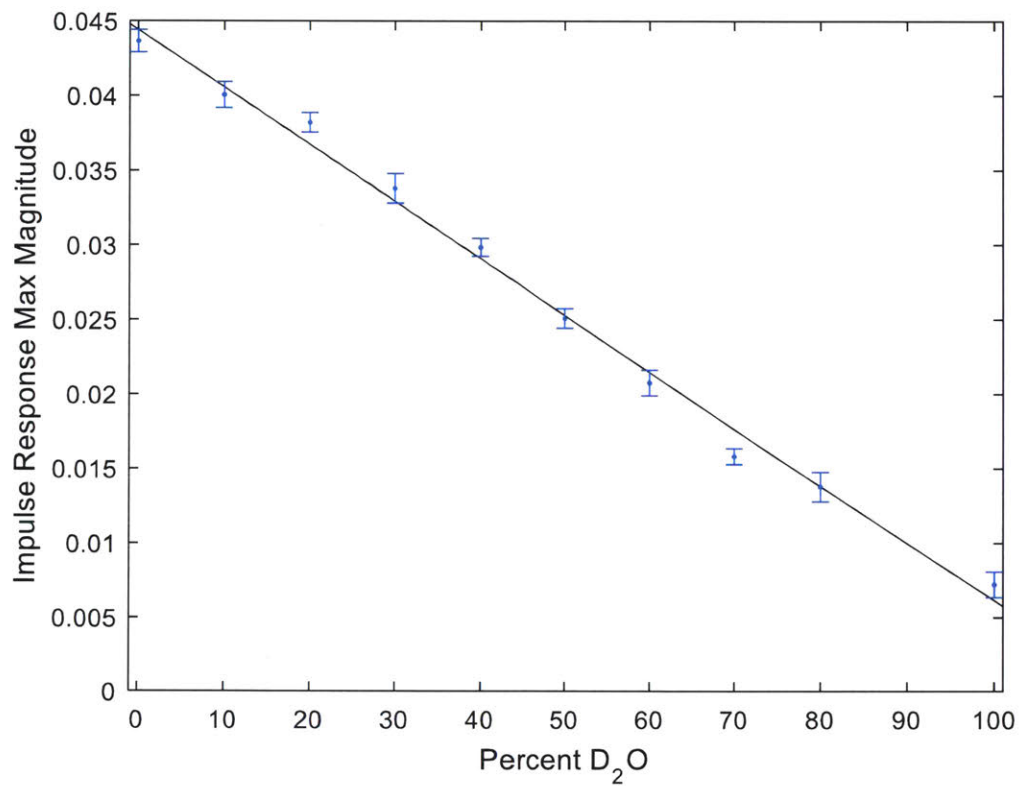


Figure 4-8: The peak value of the impulse response varied linearly with the ratio of heavy water when sampling at 100 kHz.

when the first 12 points were integrated. Similarly excellent results were obtained by fitting a second order model to just the first six data points, and then integrating the parametric model. The assumption is that with infinite averages of experimental data, the impulse response would look like the fitted function. Fig. 4-10 shows the fit for a water sample, and Fig. 4-11 the linear correlation from integrating the fit model.

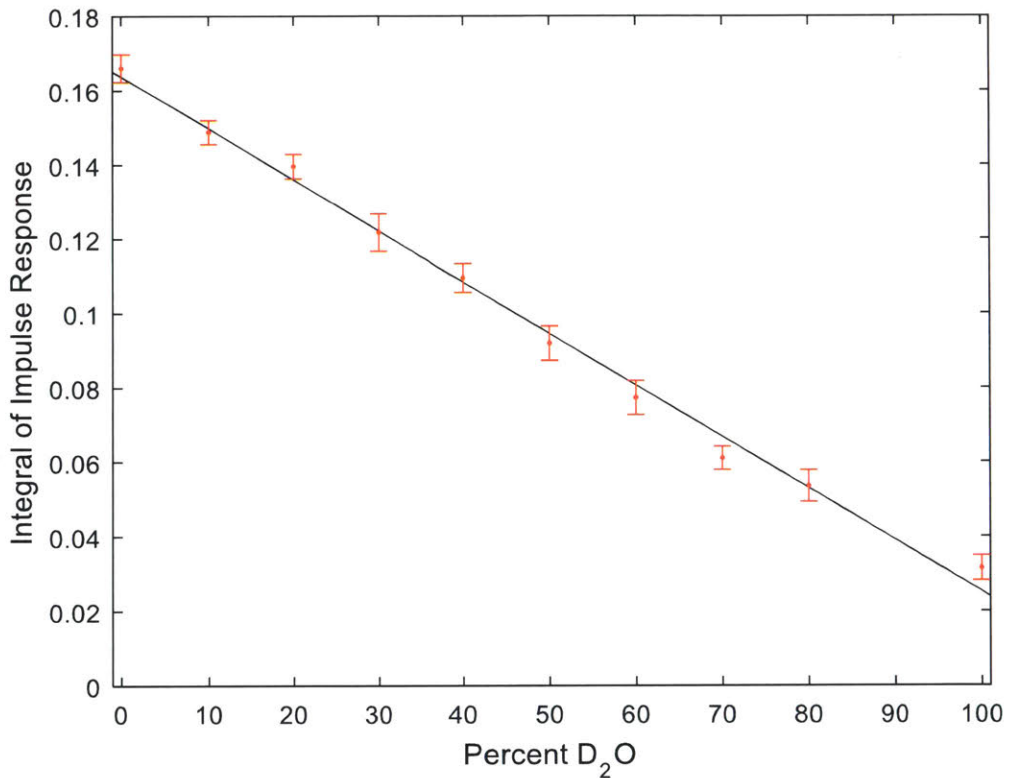


Figure 4-9: The integral of the impulse response also correlated linearly with the ratio of heavy water when sampling at 100 kHz.

Because the resonant frequency varied significantly with temperature, it was necessary at the start of each session to find resonance. Resonance was found by viewing the output of the low-frequency amplifiers on an oscilloscope, running a stochastic experiment at 50 kHz, and sending 4 V_{pp} excitation pulses. These relatively large pulses caused saturation over the entire experiment, but for the first few pulses provoked a large response visible on the scope. This response was apparent with the fast

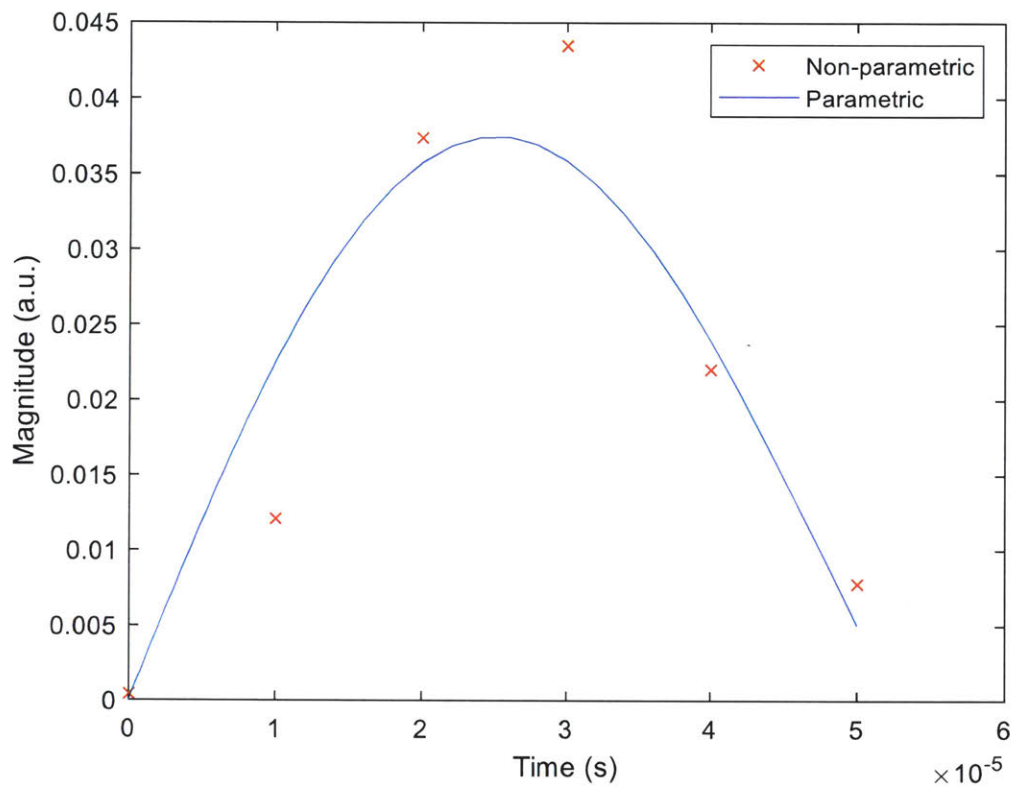


Figure 4-10: A second order model was fit to the beginning of the impulse response in order to estimate what the response would look like with no noise and faster sampling.

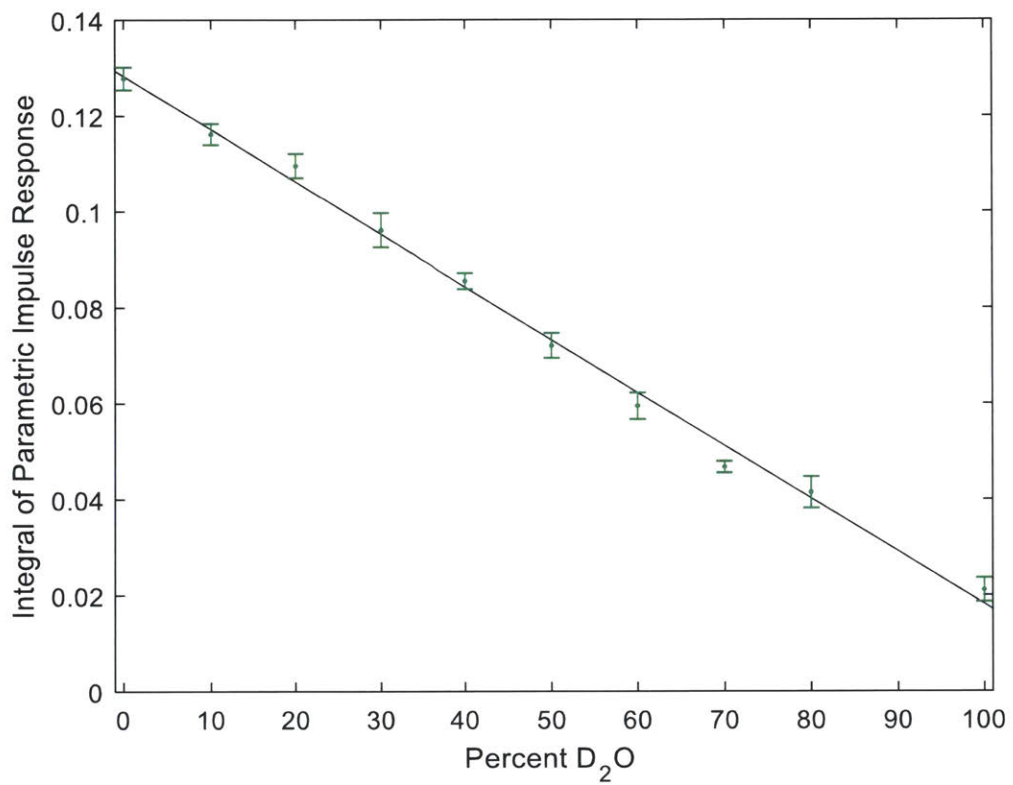
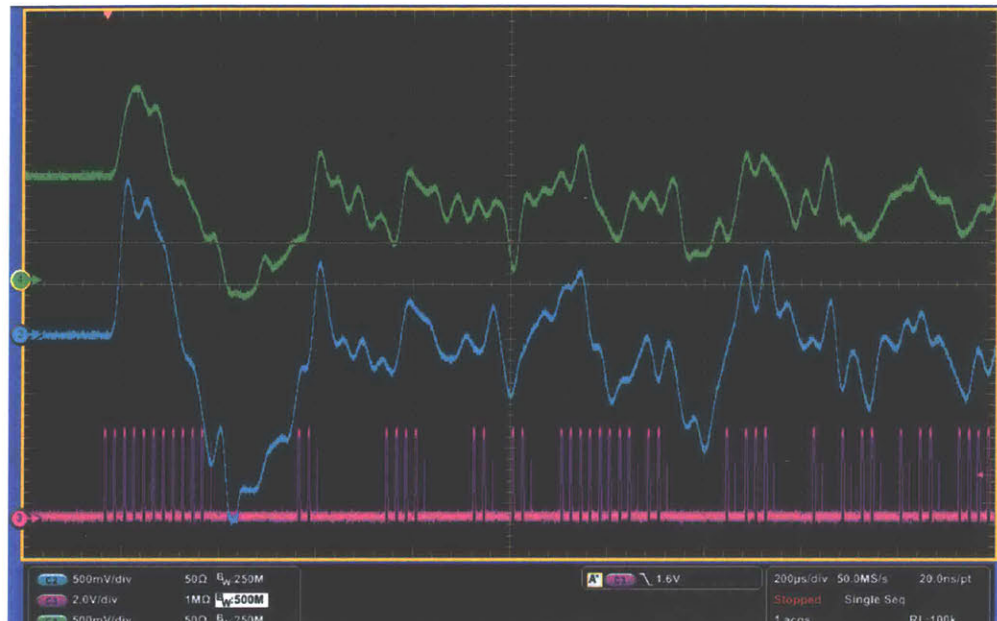


Figure 4-11: The integral of the model in Fig. 4-11 correlated linearly to the ratio of protium and deuterium.

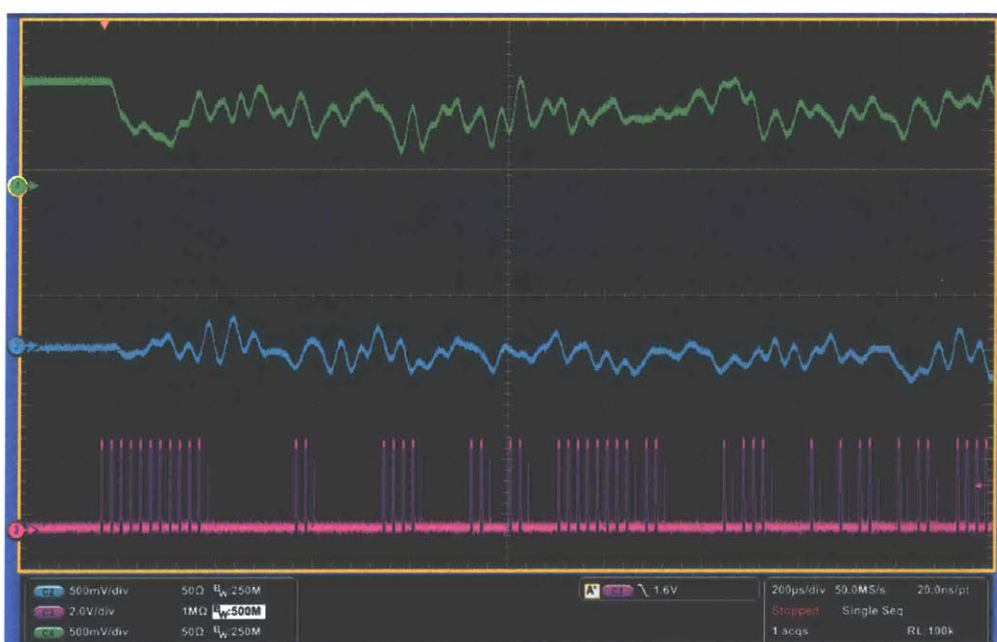
50 MHz sampling on an oscilloscope, and less visually obvious with 50 kHz sampling through the ADCs. The excitation frequency was adjusted to maximize the response seen on the scope, shown in Fig. 4-12.

In the future this process could be automated by setting up a routine that varies the excitation frequency to maximize the peak magnitude of a calibration sample FID.

The results of this section show that measuring spin density with stochastic excitation is a remarkably robust measurement. The benefits of low power excitation were evident, with no amplifier needed after the excitation pulses and a very short dead time. Although there exist uses for spin density measurements, it is worth noting that no experimental changes are needed to measure NMR spectra. The only requirement would be a sufficiently homogeneous magnetic field. Thus, these types of measurement show promise both for the present capabilities and the possibilities for future development.



(a)



(b)

Figure 4-12: The first few pulses of the m-sequence provoked a characteristic resonance response in water (a), not present for a heavy water (b). The magenta trace shows the gating signal to send pulses, and the green and blue traces the real and imaginary channels.

Chapter 5

Conclusion

Promising strategies to address significant challenges to portable NMR have been demonstrated. An ultra-low cost magnet assembly was optimized, constructed, and used to measure NMR signal. Feasibility was demonstrated for a labor-saving active shim system. Spin density was measured using low power stochastic excitation, which significantly eased the requirements on the spectrometer electronics.

Considering only the capabilities experimentally demonstrated, all the groundwork has been laid for a portable, ultra-low cost NMR device. Materials to prototype the shim-a-ring magnet were only about \$100, and would cost significantly less in volume. Manufacturing costs would be minimal. Because a standard pipe size was used as a shim, the only machining was to cut the stock to length and hone the bore. The self-assembling rings are palm-sized and have a mass of under 500 g. With no further modifications, NMR signal was recorded in the half Tesla field of the bore. The magnet and spectrometer could be handheld and portable if combined with existing technologies for miniaturized NMR electronics [5].

Using the stochastic spin density techniques, the small device is capable of incredibly robust, automated measurements. Low power excitation allows uncontaminated recording of the NMR signal with short dead time, and a short script extracts the FID from noise. Excellent correlation to spin density is obtained through a metric as naive as the peak value of the FID.

The utter simplicity of the proposed solution makes it a valuable contribution, even

while acknowledging its limited capabilities. With the active shim design, full spectroscopic measurements become possible while maintaining moderate cost. Unlike passive designs, the electromagnetic shims require no hyper-fine mechanical calibration. Instead, the current is varied in each shim to find maximum field homogeneity, a process that could be at least partially automated.

Analysis showed that an active shim system built using flexible circuits would require a current density of up to 10^8 A/m²—larger than recommended for steady state operation, but manageable for short experiments. The dissipated heat using 14 correcting shims is estimated to be less than 5 W, which would cause negligible temperature rise across the device for short experiments. A known issue is the challenge of fitting all the shims in the limited space of the magnet bore. The shims considered in this design would reduce the bore diameter to 4.4 mm, too small for a standard 5 mm diameter sample. Full-sized samples could be accommodated by scaling up the magnet design somewhat. The ideal solution would of course be to improve the manufacturing of the magnet to eliminate the need for higher order shims.

The experiment and data analysis used to measure spin density are identical to the process for measuring 1D spectra. The only additional step is to take the Fourier transform of the impulse response, assuming the data was collected in a homogeneous field.

Stochastic excitation holds great promise in the context of miniature NMR, worthy of further exploration. In particular, three dimensional experiments provide full information about the system, and maintain the short experiment time needed for the low-cost active shims. There are many challenges to be explored and overcome, such as the systematic noise in higher order measurements. This thesis charts an initial foray on a path ripe with possibility.

Appendix A

Code

A.1 LabVIEW Code

Reproduced here (Fig. A-1) is the LabVIEW code used to program the FPGA. The code generates a 2047-element-long maximum length binary sequence (MLBS), and flips the T/R switch according to this sequence using a digital output (DIO). A separate DIO controls switches gating the LO output and the preamp output. This switch could be programmed to flip delayed relative to the T/R switch in order to let noise die down before feeding signals to the sensitive mixer. The DIO ports updated with every cycle of the 40 MHz clock.

The analog sampling loop reads in the values from the external ADCs.

Using a control panel (not shown) it was possible to specify the number of repetitions of the MLBS, the sampling rate, the duty cycle, and the delay of the LO/Preamp switch relative to the T/R switch.

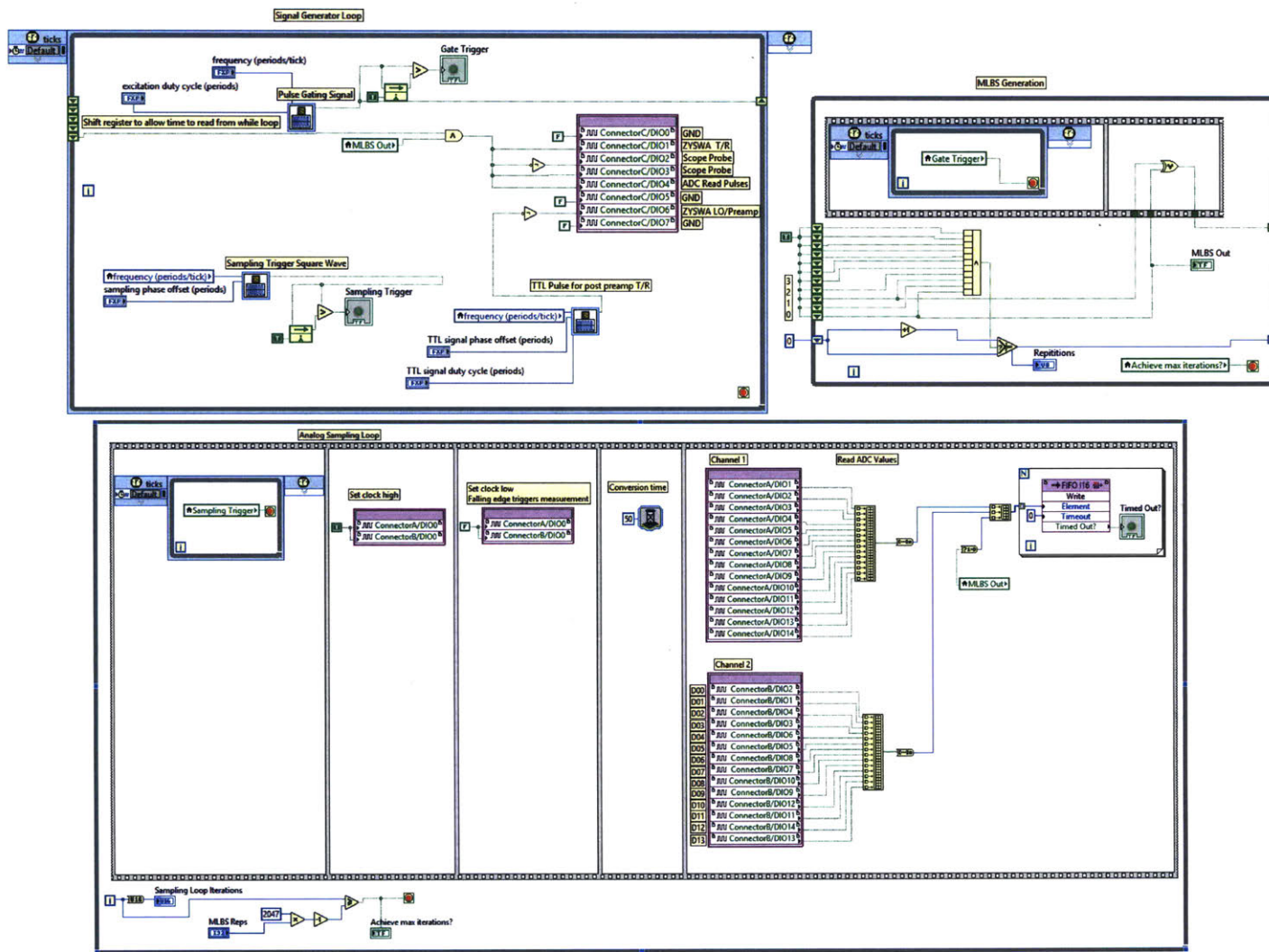


Figure A-1: The top right loop generated the MLBS, the top left loop controlled the switches, and the bottom loop read values from the ADCs.

A.2 MATLAB Code

Listing A.1: Shim design to minimize power consumption

```
1 %CoilOptimizationMinPower_AxesChange.m
2 %optimizing the stream function for shim coil design
3 %set z direction perpendicular to bore, aligned with
4 %magnetic field. Set x
5 %along bore
6 clear all
7 close all
8
9
10 %% User defined parameters
11
12 %choose harmonic to calculate
13 harmonic='T_{1,1}';
14 %options:
15 % 'T1,-1' is the Y harmonic, varies as y
16 % 'T1,0' is the Z harmonic, varies as z
17 % 'T1,1' is the X harmonic, varies as x
18 % 'T2,-2' is the XY harmonic, varies as 6*x*y
19 % 'T2,-1' is the ZY harmonic, varies as 3*z*y
20 % 'T2,0' is the Z2 harmonic, varies as z^2-(1/2)*R^2
21 % 'T2,1' is the ZX harmonic, varies as 3*z*x
22 % 'T2,2' is the X2Y2 harmonic, varies as 3*(x^2-y^2)
23 % 'T_{3,-2}' is the Z(2XY) harmonic, varies as 15*z*(2*xy)
24 % 'T_{3,-1}' is the Z2Y harmonic, varies as 3/2*y*[4*z2-
25 % (x2+y2)]
26 % 'T_{3,0}' is the Z3 harmonic, varies as z3-3/2*rho2*z
27 % 'T_{3,1}' is the Z2X harmonic, varies as 3/2*x*[4*z2-(x2-
28 % +y2)]
29 % 'T_{3,2}' is the Z(X2-Y2) harmonic, varies as 15*z*(x2-
30 % y2)
```

```

26 % 'T_{4,0}' is the Z4 harmonic, varies as z4-3*z2*rho2
27 +3/8*rho4
28
29 %Define bore geometry
30 D=10; %diameter [mm]
31 L=50; %length [mm]
32
33 %manufacturing geometry
34 d_min=0.4; %min trace width, [mm]
35 w_gap=0.1; %min gap between traces [mm]
36 t_cu=0.07; %thickness of copper trace [mm]
37
38 %Electrical and magnetic parameters
39 B0=0.5; %magnetic field [T]
40 Jmax=10; %max allowed current density, [A/mm^2]
41
42 %Physical constants
43 rho_cu=1.68e-5; %copper resistivity, [ohm*mm]
44 mu_0=1.256637e-3; %[T*mm/A]
45
46 %Define discretization parameters
47 Q_nominal=4500; %number of discrete points calculated for
48     coil surface
49
50 %Define the diameter of spherical volume (DSV)
51 %Region over which desire to generate field
52 DSV=4; %diameter of DSV in [mm]
53 N=100; %number of points to match in volume
54 epsilon=0.05; %deviation allowed from ideal field

```

```

54
55
56
57 %% Calculate discretization geometry
58
59 nominal_area=pi*D*L; %[mm^2]
60 q_area=nominal_area/Q_nominal; %nominal area per square:
    total area divided by desired # squares
61 a_nominal=sqrt(q_area); %length of tentative square
62 Qc=floor(pi*D/a_nominal); %want to divide diameter into
    integer # squares
63 a=pi*D/Qc; %final length of square, integer # to go around
    diameter
64 Qr=floor(L/a); % # of squares in vertical direction,
    rounding down again
65 Q=Qc*Qr; %number of elements created when evenly dividing
    squares
66 Lf=Qr*a; %final length after evenly dividing into squares
67
68 %need to assign an xyz location to center of each square
69 q_xyz=zeros(Q,3);
70 %need to calculate normal for each square
71 nq=zeros(Q,3);
72 %assign x and y first, and calculate normal vector
73 subtended_angle=2*pi/Qc; %subtended angle of each square
74 q_angle=subtended_angle/2; %angle of first square, to
    initialize loop
75 for q=1:Qc
    q_xyz(q,3)=D/2*cos(q_angle); %assign z coordinate to
        point q

```

```

77 q_xyz(q,2)=-D/2*sin(q_angle); %assign y coordinate to
    point q
78 nq(q,:)=[0 -sin(q_angle) cos(q_angle)]; %normal vector
79 q_angle=q_angle+subtended_angle; %augment angle for
    next iteration of loop
80 end
81 %now consider spacing of x-coordinates, along axis
82 x_range=a*(Qr-1); %from center of top square to center of
    bottom square
83 x_max=x_range/2;
84 q_x=-x_max; %initial x value in loop
85 q_count=1; %initialize q value in loop
86 for i=1:Qr
87     q_xyz((q_count:q_count+Qc-1),2:3)=q_xyz(1:Qc,2:3);%
        copy y and z values for q
88     nq((q_count:q_count+Qc-1),:)=nq(1:Qc,:); %copy normal
        vector
89     q_xyz((q_count:q_count+Qc-1),1)=q_x;%assign x value
90     q_x=q_x+a; %augment x value
91     q_count=q_count+Qc; %augment q count
92 end
93
94
95 %% randomly and evenly distribute test points in DSV
96
97 DSV_xyz = randsphere(N,3,DSV/2);
98 % This function returns an m by n array, X, in which
99 % each of the m rows has the n Cartesian coordinates
100 % of a random point uniformly-distributed over the
101 % interior of an n-dimensional hypersphere with

```

```

102 % radius r and center at the origin. The function
103 % 'randn' is initially used to generate m sets of n
104 % random variables with independent multivariate
105 % normal distribution, with mean 0 and variance 1.
106 % Then the incomplete gamma function, 'gammairc',
107 % is used to map these points radially to fit in the
108 % hypersphere of finite radius r with a uniform % spatial
109 % distribution.
110 % Roger Stafford - 12/23/05
111
112 %% target field for the coil
113
114 if strcmp(harmonic,'T_{1,-1}')
115     Btarget=DSV_xyz(:,2); %varies as y
116 elseif strcmp(harmonic,'T_{1,0}')
117     Btarget=DSV_xyz(:,3); %varies as z
118 elseif strcmp(harmonic,'T_{1,1}')
119     Btarget=DSV_xyz(:,1); %varies as x
120 elseif strcmp(harmonic,'T_{2,-2}')
121     Btarget=6*DSV_xyz(:,1).*DSV_xyz(:,2); %varies as 6*x*y
122 elseif strcmp(harmonic,'T_{2,-1}')
123     Btarget=3*DSV_xyz(:,3).*DSV_xyz(:,2); %varies as 3*z*y
124 elseif strcmp(harmonic,'T_{2,0}')
125     Btarget=DSV_xyz(:,3).^2-0.5*(DSV_xyz(:,1).^2+DSV_xyz
126         (:,2).^2); %varies as z^2-(1/2)*R^2
127 elseif strcmp(harmonic,'T_{2,1}')
128     Btarget=DSV_xyz(:,3).*DSV_xyz(:,1); %varies as 3*z*x

```

```

129 elseif strcmp(harmonic,'T_{3,-2}')
130     Btarget=15*DSV_xyz(:,3).*(2*DSV_xyz(:,1).*DSV_xyz(:,2)
131         ); %varies as 15*z*(2*xy)
132 elseif strcmp(harmonic,'T_{3,-1}')
133     Btarget=3/2*DSV_xyz(:,2).*(4*DSV_xyz(:,3).^2-(DSV_xyz
134         (:,1).^2+DSV_xyz(:,2).^2)); %varies as 3/2*y*[4*z2
135         -(x2+y2)]
136 elseif strcmp(harmonic,'T_{3,0}')
137     Btarget=DSV_xyz(:,3).^3-3/2*(DSV_xyz(:,1).^2+DSV_xyz
138         (:,2).^2).*DSV_xyz(:,3); %varies as z3-3/2*rho2*z
139 elseif strcmp(harmonic,'T_{3,1}')
140     Btarget=3/2*DSV_xyz(:,1).*(4*DSV_xyz(:,3).^2-(DSV_xyz
141         (:,1).^2+DSV_xyz(:,2).^2)); %varies as 3/2*x*[4*z2
142         -(x2+y2)]
143 elseif strcmp(harmonic,'T_{3,2}')
144     Btarget=15*DSV_xyz(:,3).*(DSV_xyz(:,1).^2-DSV_xyz(:,2)
145         .^2);
146 elseif strcmp(harmonic,'T_{4,0}')
147     Btarget=DSV_xyz(:,3).^4-3*DSV_xyz(:,3).^2.* (DSV_xyz
148         (:,1).^2+DSV_xyz(:,2).^2)+3/8*(DSV_xyz(:,1).^2+
149         DSV_xyz(:,2).^2).^2; %varies as z4-3*z2*rho2+3/8*
150         rho4
151 end
152
153 %% Define constraints for optimization
154
155 %need to constrain all edge elements to be zero
156 %Aeq*x=beq
157 q=1:Q;
158 edge=q<Qc | q>Q-Qc;% | mod(q,Qc)==0 | mod(q,Qc)==1;%find

```

```

    all the edge elements
149 Aeq=double(diag(edge));%create a matrix with 1's on the
      diagonal where there are edge elements, all others 0
150 beq=zeros(Q,1);
151
152 %need to constrain field at target points N to be close to
      desired field
153 %A*x<=b
154 %define matrix that will allow calculation of generated B
      field from S
155
156 c_xq_unscaled=zeros(N,Q); %initialize
157 %UNSCALED: won't give true value for magnetic field
158 %missing scaling factor of mu_0/(4*pi)*a^2
159 %***c_xq*S will compute the x component of the magnetic
      field***
160 %reproduced from Liu et al, 2012
161 for i=1:N
162   for j=1:Q
163     c_xq_unscaled(i,j)=((DSV_xyz(i,1)-q_xyz(j,1))^2+...
164       (DSV_xyz(i,2)-q_xyz(j,2))^2+(DSV_xyz(i,3)-
      q_xyz(j,3))^2)^(-5/2)...
165     *(2*nq(j,3)*(DSV_xyz(i,3)-q_xyz(j,3))^2 ...
166     -nq(j,3)*(DSV_xyz(i,2)-q_xyz(j,2))^2 ...
      -nq(j,3)*(DSV_xyz(i,1)-q_xyz(j,1))^2 ...
168     +3*nq(j,2)*(DSV_xyz(i,3)-q_xyz(j,3))*(DSV_xyz(
      i,2)-q_xyz(j,2)) ...
169     +3*nq(j,1)*(DSV_xyz(i,3)-q_xyz(j,3))*(DSV_xyz(
      i,1)-q_xyz(j,1)));
170 end

```

```

171 end
172 %in above: x=DSV_xyz(i,1), y=DSV_xyz(i,2), z=DSV_xyz(i,3)
173 %x_q '=q_xyz(j,1), y_q '=q_xyz(j,2), z_q '=q_xyz(j,3)
174 %nx=nq(j,1), ny=nq(j,2), nz=nq(j,3)
175
176 %for later: scaled version of C_xq
177 c_xq=mu_0/(4*pi)*a^2*c_xq_unscaled;
178
179 %A*x<=b
180 %Require: c_xy*S<=Btarget_x*(1+epsilon)
181 %-c_xy*S<=-Btarget_x(1-epsilon)
182 A=[c_xq_unscaled;-c_xq_unscaled];
183 b=[Btarget+abs(Btarget)*epsilon;-Btarget+abs(Btarget)*
    epsilon];
184
185 %%
186 %Define objective function
187 %minimize power consumption
188
189 % Minimize -1/2 * (x' * H * x) - f' * x
190 %no linear terms in power equation
191 f=zeros(Q,1);
192
193 %Hessian defined by square power matrix Wnm (eq'n 13)
194 %generate main diag terms
195 K0=2*ones(Q,1);
196 K0(1,1)=2*2;
197 K0(2:Qc,1)=2*3;
198 K0(Qc+1:Q-Qc,1)=2*4;
199 K0(Q-Qc+1,1)=2*2;

```

```

200 %K0(Q-Qc+2:Q,1)=2*1; %already preset to ones
201
202 %generate first diagonal terms
203 K1=-2*ones(Q-1,1);
204 K1(Q-Qc+1:Q-1,1)=0;
205
206 %generate the Qc diagonal terms
207 K_Qc=-2*ones(Q-Qc,1);
208
209 %Form Hessian matrix
210 H=sparse(diag(K0) + diag(K1,1) + diag(K1,-1) + diag(K_Qc,
    Qc) + diag(K_Qc,-Qc));
211
212 %% Minimize the function
213 % Choose the Algorithm to be interior-point-convex
214 qpopts = optimset('Algorithm','interior-point-convex',...
    'Display','iter');
215
216 % Perform the optimization
217 LB=[];
218 UB=[];
219
220 tic
221 [S,fval] = quadprog(H,f',A,b,Aeq,beq,LB,UB,[],qpopts);
222 toc
223
224 %%
225 %Plot the isolines of S
226
227 %Divide S into rows and columns

```

```

228 S_grid=zeros(Qr,Qc);
229 %populate
230 for i=1:Qr
231     S_grid(i,:)=S((i-1)*Qc+1:i*Qc,1);
232 end
233
234 %choose distance between levels using max gradient of S
235 Sq=S;
236 Sq1=diag(ones(Q-1,1),1)*S;%S_(q+1)
237 SqQc=diag(ones(Q-Qc,1),Qc)*S;%S_(q+Qc)
238 %calculate gradient magnitude at each point q
239 MagGradSq=1/a*sqrt((Sq1-Sq).^2+(SqQc-Sq).^2);
240 MaxGrad=max(MagGradSq);%max S gradient magnitude
241 DeltaS=MaxGrad*d_min; %step size b/w isolines of S so that
242     smallest has dist of d_min
243 Nlevels=floor((max(S)-min(S))/DeltaS);
244 Remainder=max(S)-min(S)-Nlevels*DeltaS;
245 levels=min(S)+Remainder/2:DeltaS:max(S);%distribute levels
246     centered within range
247
248 %label spacing; points separated by distance a
249 X=subtended_angle*(1:Qc);
250 Y=a*((1:Qr)-Qr/2);
251
252 figure
253 [C,h]=contour(X,Y,S_grid,levels);
254 %v=[levels(5),levels(7)];
255 %clabel(C,h,v)
256 ylabel('Axial position (mm)', 'FontSize', 16)
257 xlabel('Angle (rad)', 'FontSize', 16)

```

```

256 title(harmonic,'FontSize',18)
257
258
259 %% Calculate power dissipated and field corrected
260
261 Imax=t_cu*(d_min-w_gap)*Jmax; %max current allowed, [A]
262 Js_unit=1/(d_min-w_gap); %surface current density [A/mm]
263 %for 1 A current
264 %-->current density for 1 A is Js_unit/t_cu
265 %Max value of Js implied by the calculated S is MaxGrad
266 %--->use to scale to
267 %1 A of current
268 UnitScale=Js_unit/MaxGrad;
269
270 S_normalized=S*UnitScale; %S values corresponding to 1 A
271 %of current
272
273 %calculate the harmonic coefficient for 1A of current
274 harm_coeff_1A=mu_0/(4*pi)*a^2*UnitScale %
275
276 %calculate power dissipated for 1 A current
277 Pdiss_local=rho_cu/t_cu*(UnitScale*1)^2*((Sq1-Sq).^2+(SqQc
278 -Sq).^2);
279 Pdiss_total=sum(Pdiss_local) %power dissipation at 1 A
280 %current [W]
281
282 %check that S is scaled correctly: expect 1 A
283 %I_check=(d_min-w_gap)/a*UnitScale*max(sqrt((Sq1-Sq).^2+(SqQc-Sq).^2));

```

```
280
281 %now calculate the actual magnetic field produced per 1 A
282     current
283 B_1A=c_xq*S_normalized;
284 Bcmps=max(B_1A) %this is the max field generated at any of
285     the target points for 1 A current
286
287 %ppm corrected for 1 A
288 ppm_corrected=Bcmps/B0*10^6
```

Listing A.2: Simulation of stochastic experiments using exact Bloch solutions

```
1 %mlbs_bloch_exact.m
2 %look at response to mlbs using exact bloch solution (Bain
3 %amplitude modulated
4 close all
5 %%
6 %system parameters
7 T1=0.001; %s
8 T2=0.001; %s
9 Omega=2*pi*1000; %rad/s, offset freq
10 FlipAngle=1; %desired flip angle in degrees
11 phi=0; %phase of rf field wrt x-axis
12
13 M0=[0;0;1;1]; %unit magnetization pointing in z dir'n to
14 %start
15 %timing parameters
16 dt=20e-6; %sampling interval in s
17 duty_cycle=25; %duty cycle in percent
18 t_on=duty_cycle*dt/100; %time spent on for each step
19 t_off=dt-t_on; %time spent off for each step
20
21 %calculate strength of rf field
22 FlipAngle=pi/180*FlipAngle; %convert to radians
23 b1=FlipAngle/t_on; %equal to gamma*B1. Recall FlipAngle=
24 %gamma*B1*time
25 %generate excitation sequence
26 L=8; %sequence length is 2^L-1
```

```

27 b=mlbs_am(L); %generate the sequence using amplitude
   modulation
28 reps=10; %number of times to repeat the sequence
29 b_long=repmat(b,1,reps);
30 N=length(b_long);
31 n=length(b); %length of mlbs
32
33 %Bloch solution
34 %calculate L matrixes with rf field on
35 [lambda_on,L1_on,L2_on,L3_on,L4_on] = bloch_L(T1,T2,Omega,
   b1,phi);
36 %calculate L matrixes with rf field off
37 [lambda_off,L1_off,L2_off,L3_off,L4_off] = bloch_L(T1,T2,
   Omega,0,phi);
38
39 %perform calculations
40 M=zeros(4,N); %initialize magnetization vector
41 t=dt:dt:N*dt; %create time vector
42 M_t=M0; %magnetization will change with each step
43
44 for i=1:N
45     %effect of pulse first
46     if b_long(i)==1
47         [M_t] = bloch_expAt(t_on,M_t,L1_on,L2_on,L3_on,
           L4_on,lambda_on);
48     elseif b_long(i)==0
49         [M_t] = bloch_expAt(t_on,M_t,L1_off,L2_off,L3_off,
           L4_off,lambda_off);
50     end
51     %effect of waiting time

```

```

52 [M_t] = bloch_expAt(t_off,M_t,L1_off,L2_off,L3_off,
53 L4_off,lambda_off);
54 %record magnetization after waiting time
55 M(:,i)=M_t;
56 end
57
58 figure
59 plot(t,real(M))
60 xlabel('Time (s)')
61 ylabel('Normalized Magnetization')
62 legend('Mx','My','Mz')
63
64 %%
65 %pick out the Mx vector; discard the 1st time through the
66 %MLBS
67 Mxy=M(1,:)+1i*M(2,:);
68
69 Mxy_cut=Mxy(n+1:end); %throw out 1st rep
70 Mxy_cut=Mxy_cut-mean(Mxy_cut); %set to 0 mean
71
72 %wrap into a matrix
73 Mxy_mat=zeros(reps-1,n);
74 for i=1:reps-1
75 Mxy_mat(i,:)=Mxy_cut((i-1)*n+1:i*n);
76 end
77 %average the reps
78 Mxy_avg=mean(Mxy_mat);
79

```

```

80 FID = mxy2fid(b,Mxy_avg);
81 t_FID=dt*(0:n-1);
82 magFID=abs(FID);
83
84 figure
85 plot(t_FID,real(FID),t_FID,imag(FID),t_FID,magFID)
86 xlabel('Time (s)')
87 title('Calculated FID / Impulse Response')
88 legend('Real Part','Imaginary Part','Absolute Value')
89 %%
90 %Fourier Transform
91 Spectrum_raw=fft(FID)/(n);
92 Spectrum=fftshift(Spectrum_raw);
93
94 %frequencies computed
95 Fs=1/dt;%sampling frequency
96 L=n;%was n+1
97 f=Fs*linspace(-0.5,0.5,L);
98
99 %implement phase shift to pass signal between absorption
100 %and dispersion
101 phi=pi/2-0.1; %radians
102 Spectrum=Spectrum*exp(1i*phi);
103
104 %split into real and imaginary
105 Absorption=real(Spectrum);
106 Dispersion=imag(Spectrum);
107 Abs_spectrum=abs(Spectrum);
108

```

```
109 figure
110 plot(f,Absorption)
111 xlabel('Frequency (Hz)')
112 ylabel('Absorption Spectrum')
113 figure
114 plot(f,Dispersion)
115 xlabel('Frequency (Hz)')
116 ylabel('Dispersion Spectrum')
```

Listing A.3: Generation of amplitude-modulated maximum length binary sequence

```
1 function [b] = mlbs_am(L)
2 %MLBS_AM Generate a MLBS with amplitude modulation
3 %generate MLBS
4 %L is length of shift register used to generate sequence
5 a=zeros(1,L);
6
7 b=zeros(1,2^(L)-1);
8 N=length(b);
9 b(1:L)=1;
10
11 if L==3
12     a=[1 1 0];
13 elseif L==8
14     a(4+1)=1;
15     a(3+1)=1;
16     a(2+1)=1;
17     a(1)=1;
18 elseif L==9
19     a(4+1)=1;
20     a(1)=1;
21 elseif L==10
22     a(3+1)=1;
23     a(1)=1;
24 elseif L==11
25     a(2+1)=1;
26     a(1)=1;
27 end
28
29 for i=L:N-1
```

```
30      b(i+1)=mod(sum(a.*b((i-L+1):(i))),2);  
31 end  
32  
33 end
```

Listing A.4: Implementation of exact solution of Bloch equations

```
1 function [lambda,L1,L2,L3,L4] = bloch_L(T1,T2,Omega,b1,phi
2 )
3 %BLOCH_L Calculate the eigenvalues and L1-L4 for exact
4 % solution of Bloch
5 %eq'n, from Bain's 2010 paper
6 % Input relaxation times in sec, offset freq in rad/s,
7 % b1=gamma*B1 and is
8 % in rad/s, phi is the phase of the rf field wrt x-axis
9 %Output lambda contains the four eigenvalues
10
11
12 %relaxation times
13 R1=1/T1;
14 R2=1/T2;
15
16
17 %Generate matrix A
18 A=[-R2 -Omega b1*sin(phi) 0;...
19 Omega -R2 -b1*cos(phi) 0;...
20 -b1*sin(phi) b1*cos(phi) -R1 R1;...
21 0 0 0 0];
22
23
24 %calculate eigenvalues
25 E3=12*(b1^2+Omega^2)^3+24*(R1-R2)^2*(Omega^2-(5+3*sqrt(3))
26 *b1^2/4)*...
27 (Omega^2-(5-3*sqrt(3))*b1^2/4)+12*(R1-R2)^4*Omega^2;
28
29 E2=1/3*(Omega^2+b1^2)-1/9*(R1-R2)^2;
30
31 E1=(-8*(R1-R2)*(9*Omega^2+(R1-R2)^2)+36*(R1-R2)*b1^2+12*
32 sqrt(E3))^(1/3);
```

```

25
26 u2=-E1/12+3*E2/E1-R1/3-2*R2/3;
27
28 u3=sqrt(3)/2*(E1/6+6*E2/E1);
29
30 l1=E1/6-6*E2/E1-1/3*R1-2/3*R2;
31 l2=u2+1i*u3;
32 l3=u2-1i*u3;
33 lambda=[l1;l2;l3;0];
34
35 %calculate the Lagrange interpolation coefficients
36 I=eye(4);
37
38 L1=A*(A-12*I)*(A-13*I)/(l1*(l1-l2)*(l1-l3));
39 L2=A*(A-11*I)*(A-13*I)/(l2*(l2-l1)*(l2-l3));
40 L3=A*(A-11*I)*(A-12*I)/(l3*(l3-l1)*(l3-l2));
41 L4=(A-l1*I)*(A-l2*I)*(A-l3*I)/(-l1*l2*l3);
42
43 end

```

Listing A.5: Time evolution of magnetization using Bloch solutions

```
1 function [M] = bloch_expAt(t,M0,L1,L2,L3,L4,lambda)
2 %BLOCH_EXPAT Gives the magnetization at a time t, given
3 %the initial
4 %magnetization, Lagrange interpolation coefficients, and
5 %eigenvalues
6 % For use after L matrixes and lambda calcuated in
7 % bloch_L.m
8 %uses exact solution to Bloch equations given in Bain 2010
9
10
11
12
13 %label each eigenvalue
14 l1=lambda(1);
15 l2=lambda(2);
16 l3=lambda(3);
17
18
19 %calculate exp(A*t)
20 e_At=exp(l1*t)*L1+exp(l2*t)*L2+exp(l3*t)*L3+L4;
21
22 %calculate magnetization at time t
23 M=e_At*M0;
24
25
26 end
```

Listing A.6: Processing of experimental data from stochastic experiment

```
1 %process_mlbs_measured_2chan.m
2 % Processing data from LabVIEW acquisition for 2 channels
3 %based on the script process_mlbs_measured_2chan
4 close all
5
6 %INPUTS
7 %Mx_meas and My_meas should be pre-loaded into workspace
8 Mxy_meas=Mx_meas+1i*My_meas;
9
10 acquisition_rate=100e3; %sampling rate in Hz
11 signal=12; %approximate number of data points that contain
               signal for given conditions
12 L=11; %number of registers in the mlbs
13 reps=10; %number of times the mlbs is played
14
15 %CALCULATE PARAMETERS
16 dt=1/acquisition_rate; %time step
17 b=mlbs(L); %reproduce the mlbs used in excitation
18
19 %PROCESS DATA
20 % %throw out 1st rep, and average the others
21 n=length(b);
22 Mxy_cut=Mxy_meas(n+1:end); %throw out 1st rep
23 Mxy_cut=Mxy_cut-mean(Mxy_cut); %set to 0 mean
24 t_FID=dt*(0:n-1);
25
26 %wrap into a matrix
27 Mxy_mat=zeros(reps-1,n);
28 for i=1:reps-1
```

```

29      Mxy_mat(i,:)=Mxy_cut((i-1)*n+1:i*n);
30  end
31 %average the reps
32 Mxy_avg=mean(Mxy_mat);
33
34 %Compute the FID of the averaged response
35 FID = mxy2fid(b,Mxy_avg);
36 magFID=abs(FID);
37
38 %plot the FID
39 figure
40 plot(t_FID,real(FID),t_FID,imag(FID),t_FID,magFID,'o-')
41 xlabel('Time (s)', 'FontSize', 18)
42 ylabel('Impulse Response (a.u.)', 'FontSize', 18)
43 %title('Calculated FID / Impulse Response', 'FontSize'
44 %       , 18)
44 lgd1=legend('Real','Imaginary','Absolute Value');
45 lgd1.FontSize=18;
46 xlim([0 0.001]) %view only beginning, where signal
47 present
48
49 %Extract the max amplitude of the FID
50 maxmagFID=max(magFID)
51 %Calculate area under curve
52 integral=trapz(magFID(1:signal))

```


Bibliography

- [1] B. Blümich, S. Haber-Pohlmeier, and W. Zia, *Compact NMR*. Berlin/Boston: Walter de Gruyter GmbH, 2014.
- [2] M. Levitt, *Spin Dynamics*. second ed., 2008.
- [3] W. Jakes, A. Gerdova, M. Defernez, A. D. Watson, C. McCallum, E. Limer, I. J. Colquhoun, D. C. Williamson, and E. K. Kemsley, “Authentication of beef versus horse meat using 60 MHz ^1H NMR spectroscopy,” *Food Chemistry*, vol. 175, pp. 1–9, 2015.
- [4] M. A. Voda and J. van Duynhoven, “Bench-top NMR–Food: Solid Fat Content Determination and Emulsion Droplet Sizing,” in *Mobile NMR and MRI: Developments and Applications* (M. L. Johns, E. O. Fridjonsson, S. J. Vogt, and A. Haber, eds.), The Royal Society of Chemistry, 2016.
- [5] N. Sun, T. J. Yoon, H. Lee, W. Andress, R. Weissleider, and D. Ham, “Palm NMR and 1-chip NMR,” *IEEE Journal of Solid-State Circuits*, vol. 46, no. 1, pp. 342–352, 2011.
- [6] G. Eidmann, R. Savelsberg, P. Blümler, and B. Blümich, “The NMR MOUSE, a Mobile Universal Surface Explorer,” *Journal of Magnetic Resonance, Series A*, vol. 122, no. 1, pp. 104–109, 1996.
- [7] F. J. Rühli, T. Böni, J. Perlo, F. Casanova, M. Baias, E. Egarter, and B. Blümich, “Non-invasive spatial tissue discrimination in ancient mummies and bones in situ by portable nuclear magnetic resonance,” *Journal of Cultural Heritage*, vol. 8, no. 3, pp. 257–263, 2007.
- [8] E. Danieli, J. Perlo, B. Blümich, and F. Casanova, “Small magnets for portable NMR spectrometers,” *Angewandte Chemie - International Edition*, vol. 49, no. 24, pp. 4133–4135, 2010.
- [9] B. Rosen and L. L. Wald, “Magnetic Resonance HST.584J / 22.561,” 2006.
- [10] Yamavu, Veranschaulichung der Präzession eines Atomspins um ein externes Magnetfeld, 2009. [Online] Available: https://en.wikipedia.org/wiki/Larmor_precession.

- [11] G. Moresi and R. Magin, "Miniature permanent magnet for table-top NMR," *Concepts in Magnetic Resonance Part B: Magnetic Resonance Engineering*, vol. 19, no. 1, pp. 35–43, 2003.
- [12] F. Bloch, "Nuclear Induction," *Physical Review*, vol. 70, no. 7-8, pp. 460–474, 1946.
- [13] B. Blumich, *NMR Imaging of Materials*. Oxford University Press, 2000.
- [14] LabVIEW. National Instruments Corporation, Austin, TX. <http://www.ni.com/>.
- [15] V. Demas, A. Bernhardt, V. Malba, K. L. Adams, L. Evans, C. Harvey, R. S. Maxwell, and J. L. Herberg, "Electronic characterization of lithographically patterned microcoils for high sensitivity NMR detection.,," *Journal of magnetic resonance (San Diego, Calif. : 1997)*, vol. 200, pp. 56–63, Sept. 2009.
- [16] E. Fukushima and S. Roeder, *Experimental Pulse NMR: A Nuts and Bolts Approach*. 1981.
- [17] R. Subramanian, M. M. Lam, and G. Webb, "RF microcoil design for practical NMR of mass-limited samples.,," *Journal of magnetic resonance*, vol. 133, no. 1, pp. 227–231, 1998.
- [18] MATLAB. MathWorks, Natick, MA. <http://www.mathworks.com/>.
- [19] Instructional Tabletop MRI Scanner Wiki. Martinos Center for Biomedical Imaging, Massachusetts General Hospital. [Online] Available: https://tabletop.martinos.org/index.php/Main_Page.
- [20] H. Y. Chen, Y. Kim, P. Nath, and C. Hilty, "An ultra-low cost NMR device with arbitrary pulse programming," *Journal of Magnetic Resonance*, vol. 255, pp. 100–105, 2015.
- [21] N. Tavassolian, M. Li, C. C. Vassiliou, and M. J. Cima, "A novel magnetic relaxation-based platform for hydration monitoring," *IEEE Sensors Journal*, vol. 14, no. 8, pp. 2851–2855, 2014.
- [22] N. Sun, Y. Liu, H. Lee, R. Weissleder, and D. Ham, "Silicon RF NMR biomolecular sensor - Review," *Proceedings of 2010 International Symposium on VLSI Design, Automation and Test, VLSI-DAT 2010*, pp. 121–124, 2010.
- [23] S. B. Kim, H. Kitamura, D. Ishizuka, and D. Miyazawa, "The study to improve the field homogeneity of the HTS bulk magnets for NMR Relaxometry device by passive compensation methods," *Physics Procedia*, vol. 58, no. 3, pp. 298–301, 2014.
- [24] Pulsar, Oxford Instruments, Abingdon, United Kingdom, <https://www.oxford-instruments.com/products/spectrometers/nuclear-magnetic-resonance-nmr/pulsar>.

- [25] Spinsolve Benchtop NMR, Magritek, Wellington, New Zealand, <http://www.magritek.com/products/spinsolve/>.
- [26] picoSpin™ 45 Series II NMR Spectrometer, Thermo Fisher Scientific, Waltham, MA, <https://www.thermofisher.com/>.
- [27] NMReady-60PRO, Nanalysis, Calgary, AB, Canada, <http://www.nanalysis.com/nmready-60pro>.
- [28] E. Danieli, J. Mauler, J. Perlo, B. Blümich, and F. Casanova, "Mobile sensor for high resolution NMR spectroscopy and imaging," *Journal of Magnetic Resonance*, vol. 198, no. 1, pp. 80–87, 2009.
- [29] B. Manz, M. Benecke, and F. Volke, "A simple, small and low cost permanent magnet design to produce homogeneous magnetic fields," *Journal of Magnetic Resonance*, vol. 192, pp. 131–138, may 2008.
- [30] C. Hugon, F. D'Amico, G. Aubert, and D. Sakellariou, "Design of arbitrarily homogeneous permanent magnet systems for NMR and MRI: theory and experimental developments of a simple portable magnet.," *Journal of magnetic resonance*, vol. 205, pp. 75–85, jul 2010.
- [31] V. Demas, J. L. Herberg, V. Malba, A. Bernhardt, L. Evans, C. Harvey, S. C. Chinn, R. S. Maxwell, and J. Reimer, "Portable, low-cost NMR with laser-lathe lithography produced microcoils," *Journal of Magnetic Resonance*, vol. 189, pp. 121–129, nov 2007.
- [32] A. McDowell and E. Fukushima, "Ultracompact NMR: ^1H spectroscopy in a subkilogram magnet," *Applied Magnetic Resonance*, vol. 35, no. 1, pp. 185–195, 2008.
- [33] C. L. Zimmerman, "Low-field Classroom Nuclear Magnetic Resonance System," Master's thesis, MIT, 2010.
- [34] H. D. Phuc, P. Pouliche, T. T. Cong, A. Fakri, C. Delabie, and L. Fakri-bouchet, "Design and construction of light weight portable NMR Halbach magnet," *International Journal on Smart Sensing and Intelligent Systems*, vol. 7, no. 4, pp. 1555–1578, 2014.
- [35] P. Nath, C. K. Chandrana, D. Dunkerley, J. A. Neal, and D. Platts, "The "shim-a-ring" magnet: Configurable static magnetic fields using a ring magnet with a concentric ferromagnetic shim," *Applied Physics Letters*, vol. 102, no. 20, 2013.
- [36] R. Magin, a.G. Webb, and T. Peck, "Miniature magnetic resonance machines," *IEEE Spectrum*, vol. 34, no. 10, pp. 51–61, 1997.
- [37] PM1055 Permanent Magnets, Metrolab, Geneva, Switzerland, <https://www.metrolab.com/products/pm1055/>.

- [38] H. Raich and P. Blümller, “Design and construction of a dipolar Halbach array with a homogeneous field from identical bar magnets: NMR mandhalas,” *Concepts in Magnetic Resonance Part B: Magnetic Resonance Engineering*, vol. 23, no. 1, pp. 16–25, 2004.
- [39] C. K. Chandrana, J. A. Neal, D. Platts, B. Morgan, and P. Nath, “Automatic alignment of multiple magnets into Halbach cylinders,” *Journal of Magnetism and Magnetic Materials*, vol. 381, pp. 396–400, 2015.
- [40] C. Hugon, P. M. Aguiar, G. Aubert, and D. Sakellariou, “Design, fabrication and evaluation of a low-cost homogeneous portable permanent magnet for NMR and MRI,” *Comptes Rendus Chimie*, vol. 13, pp. 388–393, Apr. 2010.
- [41] COMSOL Multiphysics. COMSOL Inc., Stockholm, Sweden. <http://www.comsol.com/>.
- [42] R. A. De Graaf and C. Juchem, “B0 Shimming Technology,” in *New Developments in NMR*, vol. 7, pp. 166–207, 2016.
- [43] E. Danieli, J. Perlo, F. Casanova, and B. Blumich, “High-Performance Shimming with Permanent Magnets,” in *Magnetic Resonance Microscopy: Spatially Resolved NMR Techniques and Applications*, ch. 30, pp. 487–499, 2009.
- [44] R. R. Ernst, “Measurement and control of magnetic field homogeneity,” *Review of Scientific Instruments*, vol. 39, no. 7, pp. 998–1012, 1968.
- [45] W. Liu, F. Casanova, B. Blümich, and D. Zu, “An Efficacious Target-Field Approach to Design Shim Coils for Halbach Magnet of Mobile NMR Sensors,” *Applied Magnetic Resonance*, vol. 42, no. 1, pp. 101–112, 2012.
- [46] J. M. Mendoza. The Modeling and Characterization of a Lorentz-Force Actuator for Needle-Free Injection. Undergraduate thesis, MIT, 2011.
- [47] I. S. Mackenzie, E. M. Robinson, A. N. Wells, and B. Wood, “A simple field map for shimming,” *Magnetic Resonance in Medicine*, vol. 5, no. 3, pp. 262–268, 1987.
- [48] F. Romeo and D. I. Hoult, “Magnet Field Profiling: Analysis and Correcting Coil Design,” *Magnetic Resonance in Medicine*, vol. 1, pp. 44–65, 1984.
- [49] R. Turner, “A target field approach to optimal coil design,” *Journal of Physics D: Applied Physics*, vol. 19, no. 8, pp. 6–11, 1986.
- [50] C. Hugon, X. Li, G. Aubert, and D. Sakellariou, “Generalized shim and gradient generation: Application to the magic angle field spinning case,” *Microporous and Mesoporous Materials*, vol. 178, pp. 31–33, 2013.
- [51] Y. Xu, Q. Chen, G. Zhang, Z. Pei, and X. Yang, “Shim Coils Design for Halbach Magnet Based on Target Field Method,” *Applied Magnetic Resonance*, vol. 46, no. 7, pp. 823–836, 2015.

- [52] G. Peeren, “Stream function approach for determining optimal surface currents,” *Journal of Computational Physics*, vol. 191, no. 1, pp. 305–321, 2003.
- [53] G. Peeren, *Stream Function Approach for Determining Optimal Surface Currents*. PhD thesis, Eindhoven University of Technology, 2003.
- [54] Flexible Circuit Technologies, Plymouth, MN, *Flexible Circuit & Heater Design Guide*, 2008.
- [55] C. Hugon, J. Polesel, V. Martinez, and D. Sakellariou, “Simple procedure for the fabrication of flexible NMR shim coils,” *Comptes Rendus Chimie*, vol. 16, pp. 967–971, 2013.
- [56] M. Finstad, *Reliable Flexible Circuit Design and Manufacturing*. Flexible Circuit Technologies, Plymouth, MN.
- [57] Flexible PCB Capabilities & Tolerances. PCB Universe. [Online]. Available: <http://www.pcouniverse.com/pcb-universe/flexible-pcb.php>.
- [58] IPC-2221 Generic Standard of Printed Board Design. IPC, Northbrook, IL, 1998.
- [59] Trace Width Calculator. Advanced Circuits. [Online] Available: <http://www.4pcb.com/trace-width-calculator.html>.
- [60] C. Z. Cooley, *Portable Low-Cost Magnetic Resonance Imaging*. PhD thesis, MIT, 2014.
- [61] B. Blümich and D. Ziessow, “Nonlinear noise analysis in nuclear magnetic resonance spectroscopy. 1D, 2D, and 3D spectra,” *Journal of Chemical Physics*, vol. 78, no. 3, pp. 1059–76, 1983.
- [62] B. Blümich, “Stochastic Excitation,” in *eMagRes*, 2007.
- [63] J. Paff, R. Freeman, and B. Blumich, “Reduction of Systematic Noise in Stochastic-Excitation NMR by Oversampling,” 1993.
- [64] R. R. Ernst, “Nuclear magnetic resonance Fourier transform spectroscopy,” *Bio-science Reports*, vol. 12, no. 3, pp. 143–187, 1992.
- [65] P. Z. Marmarelis and V. Z. Marmarelis, *Analysis of Physiological Systems: The White Noise Approach*. Computers in Biology and Medicine, New York: Plenum Press, 1978.
- [66] R. Kaiser, “Application of the Hadamard transform to NMR spectrometry with pseudonoise excitation,” *Journal of Magnetic Resonance (1969)*, vol. 15, no. 1, pp. 44–63, 1974.
- [67] B. Blümich and D. Ziessow, “Saturation in hadamard NMR spectroscopy and its description by a correlation expansion,” *Journal of Magnetic Resonance*, vol. 46, no. 3, pp. 385–405, 1982.

- [68] D. Ziessow and B. Blümich, "Hadamard-NMR Spektroskopie," *Berichte der Bunsengesellschaft für physikalische Chemie*, vol. 78, no. 11, pp. 1168–1179, 1974.
- [69] B. Blümich and R. Kaiser, "Stochastic NMR on a commercial spectrometer," *Journal of Magnetic Resonance*, vol. 58, no. 1, pp. 149–151, 1984.
- [70] B. Blümich and D. Ziessow, "2D NMR Spectra from Stochastic NMR. Coupling and Exchange Information from Third Order Frequency Kernel," *Berichte der Bunsengesellschaft für physikalische Chemie*, vol. 84, no. 11, pp. 1090–1102, 1980.
- [71] B. Blümich, "Stochastic NMR spectroscopy," *Bulletin of Magnetic Resonance*, vol. 7, no. 1, pp. 5–23, 1985.
- [72] H. Todt, G. Guthausen, W. Burk, D. Schmalbein, and A. Kamrowski, "Water-/moisture and fat analysis by time-domain NMR," *Food Chemistry*, vol. 96, no. 3, pp. 436–440, 2006.
- [73] Oxford Instruments, Abingdon, United Kingdom, *Application Note 8: Measurement of Oil Content in Jatropha curcas seeds*, 2018.
- [74] Oxford Instruments, Abingdon, United Kingdom, *Application Note 25: Determination of grease content for water quality monitoring using the MQC+23*, 2018.
- [75] Oxford Instruments, Abingdon, United Kingdom, *Application Note 14: Standard Method for Hydrogen Content in Fuels (ASTM D7171-16)*, 2017.
- [76] Oxford Instruments, Abingdon, United Kingdom, *Application Note 5: Measurement of Fluoride Content in Toothpaste*, 2014.
- [77] Oxford Instruments, Abingdon, United Kingdom, *Application Note 20: Measurement of Calcium Fluoride Content in Fluorospar*, 2018.
- [78] Oxford Instruments, Abingdon, United Kingdom, *Application Note 21: Measurement of Fluorine Content in Alumina*, 2018.
- [79] A. D. Bain, C. K. Anand, and Z. Nie, "Exact solution to the Bloch equations and application to the Hahn echo," *Journal of Magnetic Resonance*, vol. 206, no. 2, pp. 227–240, 2010.